

Master's thesis

2019

Master's thesis

Mike Alexander Lund

NTNU
Norwegian University of
Science and Technology
Faculty of Natural Sciences
Department of Physics

Mike Alexander Lund

Spin Pumping from Uniform, Non-collinear Antiferromagnets

June 2019



Norwegian University of
Science and Technology



Norwegian University of
Science and Technology

Spin Pumping from Uniform, Non- collinear Antiferromagnets

Mike Alexander Lund

Master of Science in Physics and Mathematics

Submission date: June 2019

Supervisor: Arne Brataas, IFY

Co-supervisor: Akashdeep Kamra, IFY

Norwegian University of Science and Technology
Department of Physics

Abstract

Motivated by recent theoretical work on spin pumping in two-sublattice magnets we investigate the effect of cross-sublattice spin pumping on the total dc spin pumping current pumped from an antiferromagnet and whether it can be detected experimentally. We use an antiferromagnetic/normal metal bilayer model with three different antiferromagnetic systems, driven into harmonic oscillations by a time-varying applied field, to numerically calculate the dc spin current pumped from the magnetic systems. Two systems in a collinear ground state and one system in a non-collinear ground state are considered. To calculate the spin current the solution to the Landau-Lifshitz-Gilbert-equations of motion is calculated for the three systems, and an analytic expression for the dc spin current for the two types of ground states.

The solution to the LLG-equations for the easy axis antiferromagnet (AFM) in a collinear ground state presented in this thesis, is in excellent agreement with the literature. Due to the breaking of rotational symmetry, by applying a magnetic field along the easy axis, two distinct rotational modes (plus and minus modes) emerge for the antiferromagnetic magnetizations. This results in only one peak for the spin current at resonance of the excited mode. The spin current expression displays polarization in only the z-direction, making it impossible to isolate the cross-sublattice contributions experimentally. The effect of cross-sublattice spin pumping is found to decrease the total spin current pumped from the magnet.

For the biaxial antiferromagnet in a collinear ground state, the solution to the LLG-equations are found to be reasonable, since the easy axis solution is obtained for $K_x = 0$. Adding a hard axis coupled the plus and minus modes, such that two peaks are observed for the spin pumping current for plus and minus polarized ac-field. Similar to the easy axis case, the spin current is reduced by the cross-sublattice contributions.

The solution to the LLG-equation presented for the easy-axis antiferromagnet, in the spin flop state (non-collinear ground state), is found to be reasonable. Due to the non-collinearity of the sublattice magnetization vectors, the only the plus mode of the antiferromagnet can be excited, consistent with the literature. The spin current therefore only displays one peak. The analytic expression for the spin current shows polarization components in the x-,y- and z-directions, however the numerical calculations shows only a non-zero spin current polarized in the z-direction for the parameters employed. Thus, the cross-sublattice contributions cannot be isolated experimentally. The same effect of the cross-sublattice contributions as in the collinear cases is observed.

Sammendrag

Motivert av nylig teoretisk arbeid med spin pumping i to-subgitter magneter vil vi undersøke effekten av kryss-subgitter spin pumping på den totale dc spin pumpestrømmen pumpet fra en antiferromagnet, og om dette kan bli målt eksperimentelt. Vi benytter en antiferromagnet/normal metal-dobbeltlag modell med tre forskjellige antiferromagnetiske systemer, drevet inn i harmonisk oscillasjon av et tidsvarierende magnetisk felt, for å numerisk beregne spin pumpestrømmen fra det magnetiske systemet. To antiferromagnetiske systemer i kolineær grunnstilstand og et i ikke-kolineær grunnstilstand vil bli brukt. For å beregne spinstrømmen vil løsningen på Landau-Lifshitz-Gilbert-bevegelsesligningene (LLG-ligningene) bli beregnet for de tre systemene, samt et analytisk uttrykk for dc spin pumpestrømmen for de to typene grunnstilstander som er undersøkt.

Løsningen på LLG-ligningene for ”easy-axis” antiferromagneten, i kolineær grunnstilstand, viser seg å stemme utmerket godt med litteraturen. Å påføre magneten et magnetisk felt i samme retning som den ”myke”-aksen, blir rotasjonssymmetrien til magneten brutt, som fører til to distinkte rotasjonsmoder (plus og minus modene) for sub-gittermagnetiseringsvektorene. Dette resulterer i kun én topp for spinstrømmen for resonansfrekvensen til de to rotasjonsmodene. Spinstrømmuttrykket viser kun en spinstrøm polarisert i z-retning, slik at kryss-subgitter bidragene til spinstrømmen ikke kan isoleres eksperimentelt. Bidraget fra kryss-subgitter spin pumping reduserte den totale dc spinstrømmen fra magneten.

Løsningen på LLG-ligningene for biaxial antiferromagneten ble funnet å være fornuftig, ettersom løsningen for reduseres til løsningen for antiferromagneten i grensen $K_x = 0$. Å legge til en hard akse fører til en kobling av plus og minus modene, slik at to toppe ble observert for spin pumpestrømmen for både påført plus og minus polarisert ac-felt. Samme effekt av kryss-subgitter spin pumping som for easy-axis magneten er observert.

Løsningen på LLG-ligningene for easy-axis antiferromagneten i ikke-kolineær grunnstilstand (spin flop tilstand), viser seg å være fornuftig. Den ikke-kolineære konfigurasjonen av magnetiseringsvektorene fører til kun én rotasjonsmode, konsistent med litteraturen. Det analytiske uttrykket for spin pumpestrømmen viser at spinstrømmen er polarisert i x-, y- og z-retning. De numeriske beregningene viser at kun z-komponenten ikke er null for de brukte parameterene, slik at kryss-subgitter bidragene til spin pumpe strømmen ikke kan isoleres og måles eksperimentelt. Igjen ble den totale dc spin strømmen redusert av kryss-subgitter bidragene.

Preface

Before you lies the master thesis "Spin pumping from uniform, non-collinear antiferromagnets", the basis of which is a theoretical investigation of and predictions for the effect cross-sublattice contributions to the spin pumping current from antiferromagnets. It has been written to fulfill the requirements of graduating from the master's degree program in Applied Physics and Mathematics at the Norwegian University of Science and Technology. The thesis was written during the last semester of the fifth-year of the master's degree study.

The research has been challenging, especially since my supervisor had a very busy schedule and was away for some time during the work period, limiting the opportunity to have quality meetings. This resulted in great time pressure when the thesis was written, reflected in the thesis. This has also greatly improved my ability to work independently and to check that the results makes sense in the absence of literature to compare with.

I first of all would like to thank my supervisor researcher Akashdeep Kamra for taking time out of his very busy schedule to be my supervisor, specially in the last week of writing when I needed it the most. I would also like to thank Postdoc. Roberto Troncoso for contributing to the discussions in some of the meetings. Last, but not least I give my sincere gratitude to my parents who have provided both mental and financial support during my time at university.

Mike Alexander Lund
Trondheim, Norway
June, 2019

Table of Contents

Abstract	i
Sammendrag	iii
Preface	v
Table of Contents	viii
List of Figures	xii
Nomenclature	xiii
1 Introduction	1
1.1 Motivation	1
1.2 Outline	3
2 Theoretical background	5
2.1 Magnetostatics	5
2.1.1 The exchange interaction	7
2.1.2 Anisotropy	10
2.1.3 Zeeman energy	12
2.2 Antiferromagnetic ground state	13
2.3 Magnetization dynamics	16
2.3.1 The Landau-Lifshitz equation of motion	16
2.3.2 Spin wave theory for antiferromagnets	19
2.4 Spin dynamics in antiferromagnet/normal metal bilayers	22

2.4.1	Spin pumping	23
2.4.2	Spin accumulation induced by spin pumping current	25
2.4.3	Electrical detection of spin currents: The Inverse Spin Hall effect	27
3	Results and discussion	31
3.1	Easy axis antiferromagnet in collinear ground state	32
3.1.1	Magnetization dynamics	32
3.1.2	Dc spin pumping current density and ISHE-voltage	36
3.2	Biaxial antiferromagnet in collinear ground state	42
3.2.1	Magnetization dynamics	42
3.2.2	Dc spin pumping current density and ISHE-voltage	45
3.3	Easy axis antiferromagnet in spin flop state, static applied field	49
3.3.1	Magnetization dynamics	49
3.3.2	Dc spin pumping current and ISHE-voltage	55
4	Conclusion	67
4.1	Summery and concluding remarks	67
4.1.1	Outlook	68
	Bibliography	69
	Appendix	77
4.2	Equation of motion of the magnetization from Lagrangian formalism . . .	77
4.3	Coordinate transformations	79
4.4	Numerics	80
4.4.1	Codes	81

List of Figures

1.1	Voltage detection in ferromagnetic/normal metal bilayer	3
2.1	Schematic depiction of the magnetic structure at microscopic level, and the net moment for ferro-, ferri- and antiferromagnets. The illustration is adapted from (Kamra, 2015).	6
2.2	Schematic depiction of a 1D lattice of spins exhibiting ferromagnetic (top) and antiferromagnetic (bottom) ordering of spins. The spin at lattice site i interacts with the spin at lattice site j	9
2.3	Definitions of the directional cosines.	11
2.4	Schematic depiction of the torque, τ , acting on the magnetization, \mathbf{M} , of a ferromagnet by a magnetic field, \mathbf{H} , applied with an angle θ with respect to the magnetization direction. The torque bends the magnetization in the direction of the applied field.	12
2.5	Schematic depiction of the ground state configurations of an antiferromagnet with easy axis anisotropy in a static applied field. (a) For a sufficiently low magnetic field applied along the easy axis, the collinear ground state remains unchanged. (b) With growing field, the transition to the spin flop state occurs. (c) Increasing the field further decreases the angle between magnetization vectors, and at a critical field, $\mathbf{H}_0 = \mathbf{H}_{\parallel}$, the spin flip transition occurs. (d) Applying a magnetic field along a hard axis (perpendicular to the easy axis) decreases the angle between \mathbf{M}_A and \mathbf{M}_B for increasing field, \mathbf{H}_0 . (e) At a critical value, $\mathbf{H}_0 = \mathbf{H}_{\perp}$, the spin flip transition occurs.	15

2.6	Schematic depiction of the precession of the magnetization \mathbf{M} (blue vector) due to an externally applied field \mathbf{H}_{ext} (black vector). The Gilbert damping term causes the magnetization vector to spiral down to the equilibrium magnetization direction, indicated by the dashed blue line.	17
2.7	Illustration of a spin wave. The relative motion of the electron magnetic moments (black arrows) creates a wave (a magnon) illustrated by the red curve.	20
2.8	Schematic depiction of spin pumping in a antiferromagnet/normal metal bilayer (AFM/NM-layer) from one of the sublattice magnetizations driven into uniform oscillations by an applied ac-field. Note that both sublattice magnetizations contributes to the injected current. The oscillating sublattice magnetization, \mathbf{M}_A , pumps a spin current into the normal metal, creating a spin accumulation density, μ_N at the interface. The spin density diffuses into the metal, driving the spin pumping current \mathbf{j}_s^{pump} , and back into the magnet, causing spin back-flow, \mathbf{j}_s^{back} . The polarization, $\hat{\mathbf{s}}$, of the spin current is illustrated by the yellow arrows. The field, \mathbf{H}_0 , is the static part of the applied field.	23
2.9	Schematic depiction of a pure charge current (a), with no net spin current, a spin polarized charge current (b), where electrons with opposite spins move in the same direction, and a pure spin current (c), where electrons with opposite spins propagate in the opposite direction, creating a net spin current and no charge current. The figure is adapted from (Muller, 2017) .	25
2.10	Schematic depiction of the Inverse Spin Hall effect. The pure spin current, J_s , with polarization, σ , pumped into the normal metal is scattered by electrons and impurities in the metal. Due to antisymmetric scattering of electrons with opposite spin polarization, the spin current electrons are bent towards one edge of the sample, inducing an electrical field E_{ISHE} . The electric potential due to the accumulation of charges is shown by the + and - signs at the edges. The figure is adapted from (Ando et al., 2011) and is slightly altered.	28
3.1	Schematic depiction of the two eigenmodes of the antiferromagnetic magnetizations. The chiralities and cone angle ratios are opposite for the two modes. The plus mode constitutes counter clockwise rotation, while the minus mode demonstrates clock wise rotation. The angles of the two sublattice magnetizations have been exaggerated for clarity.	35

3.2	The dc spin pumping current, for the plus polarized mode of the easy axis antiferromagnet in collinear ground state, as a function of frequency, ω , of the ac-field. The current is plotted for four different values of the magnitude of the steady part of the applied field.	39
3.3	The dc spin pumping current, for the minus polarized mode of the easy axis antiferromagnet in collinear ground state, as a function of frequency, ω , of the applied field. The current is plotted for four different values of the magnitude of the steady part of the applied field.	40
3.4	The dc spin pumping current, for the easy axis AFM excited by a linear polarized applied field, as a function of frequency, ω . The current is plotted for four different values of the magnitude of the steady part of the applied field.	41
3.5	The dc spin pumping current, for the easy axis AFM excited by a linear polarized applied field, as a function of frequency, ω . The current is plotted for four different values of the cross-sublattice spin mixing conductance.	42
3.6	The dc spin pumping current, for the biaxial AFM, as a function of frequency, ω , for four different values of H_0 . A right circularly polarized magnetic field has been applied.	46
3.7	Schematic depiction of the hybridized mode of the biaxial antiferromagnet in collinear ground state. The mode is linearly polarized with equal angles between the sublattice magnetizations.	47
3.8	The dc spin pumping current, for the biaxial AFM, as a function of frequency, ω for four different values of H_0 . A left circularly polarized magnetic field has been applied.	47
3.9	The dc spin pumping current, for the biaxial AFM, as a function of frequency, ω , for four different values of H_0 . A linearly polarized field is applied.	48
3.10	The dc spin pumping current, for the biaxial AFM, as a function of frequency, ω , for four different values of g_{AB} . A linearly polarized field is applied.	49
3.11	Schematic depiction of the ground state configuration of the antiferromagnet for static external applied field along the easy (z-) axis	50
3.12	Schematic depiction of the three coordinate systems employed in describing the dynamics of the system. In the ground state $\vec{M}_A = M_{A0}\hat{z}'$ and $\vec{M}_B = -M_{B0}\hat{z}''$. The x-coordinate for the three coordinate systems coincide	52

3.13	The dc spin pumping current polarized in the x-direction, as a function of frequency, ω , for four different values of H_0 . A linearly polarized field is applied.	60
3.14	The dc spin current polarized in the y-direction, for the non-collinear AFM system, for different values of the static applied field, H_0 and different modes of the ac-field. In a) (plus mode) and b) (minus mode) only one mode is used. In c) a linearly polarized field is employed.	63
3.15	The dc spin current polarized in the z-direction, for the non-collinear AFM system, for different values of the static applied field, H_0 . A right circularly polarized applied field has been employed.	64
3.16	The dc spin current polarized in the z-direction, for the non-collinear AFM system, for different values of the static applied field, H_0 . A left circularly polarized applied field has been employed	64
3.17	The dc spin current polarized in the z-direction, for the non-collinear AFM system, for different values of the static applied field, H_0 . A linearly polarized applied field has been employed	65
3.18	The dc spin current polarized in the y-direction, for the non-collinear AFM system, for different values of the cross-sublattice spin mixing conductance, g_{AB} . A linearly polarized applied field has been employed	65
3.19	The dc spin current polarized in the z-direction, for the non-collinear AFM system, for different values of the cross-sublattice spin mixing conductance, g_{AB} . A linearly polarized applied field has been employed	66
4.1	An xy -Cartesian coordinate system rotated through an angle θ to an $x'y'$ -Cartesian coordinate system	79

Nomenclature

Symbols

F	=	Free energy
μ_0	=	Magnetic permeability
γ	=	Gyromagnetic ratio
J	=	Exchange integral
K_z	=	Easy axis anisotropy constant
K_x	=	Hard axis anisotropy constant
M_0	=	Saturation magnetization
$\alpha_{AA,BB}$	=	Intra-sublattice damping parameter on sublattice A,B
$\alpha_{AB,BA}$	=	Cross-sublattice damping parameter on sublattice A,B
\mathbf{M}	=	Magnetization
$\hat{\mathbf{m}}$	=	Unit vector magnetization
$j_s^{0,dc}$	=	Dc spin pumping current
$\hat{\mathbf{s}}$	=	Unit vector polarization of the electrons in the spin current
$g_{AA,BB}$	=	Intra-sublattice spin mixing conductance for sublattice A,B
$g_{AB,BA}$	=	Cross-sublattice spin mixing conductance for sublattice A,B
$V_{x,y,z}$	=	Inverse Spin Hall effect voltage

Conventions

Boldsymbol = Vector

Introduction

1.1 Motivation

Today's conventional electronic and data storing devices mainly utilize charge currents as information carrier. The constant demand for larger storage capabilities and higher processing power has pushed the boundaries of semiconductor electronics technology, resulting in miniaturization of the electric components. However, as the electronic components become smaller and smaller, the quantum effects of single electrons come more and more into play, resulting in excessive heat that is difficult to get rid of (Tveten, 2016), and the rapid technological development is seemingly headed for an inevitable halt. A new concept is therefore needed to continue the rapid technological advancement.

An alternative is to employ the spin-degree of freedom of the electron as information carrier in conjunction with, or instead of, the electron charge (Shen, 2008). This is the main objective in the field of spintronics, which seeks to exploit and manipulate the electron spin in electrical circuits. Using spin instead of electric charge, i.e using a spin polarized current instead of a charge current, more energy-effective electronic technology can be made (Joshi, 2016) as spin currents offer lower power dissipation (Mosendz et al., 2010). This has made spintronics an exciting field in considerable expansion. The discovery of the giant magnetoresistance (GMR) effect in multilayer ferromagnetic thin films, by A. Fert (Baibich et al., 1988) and P. Grünberg (Binasch et al., 1989) in 1988, marks the birth of the field of spintronics. Later, this discovery generated widespread industrial importance as a fundamental part of hard drive read-head sensors and magnetic random access memory (MRAM) cells (Dieny et al., 2016).

Currently, most spin based devices use ferromagnets, in which the constituent spins

tend to align parallel resulting in a spontaneous net magnetic moment, as the active component. The spontaneous net magnetic moment makes ferromagnets easy to manipulate magnetically, however it also creates fundamental limiting factors related to robustness against spurious magnetic fields and power-efficiency. Since the magnetic moment is so easy to manipulated, it is also sensitive to magnetic reading and field perturbations from other components. In addition these devices require high current densities to store information. To overcome some of the drawbacks of ferromagnets, researchers have turned their interest towards antiferromagnets (AFMs) as a potential candidate to replace ferromagnets as the active component in spin-based devices. Antiferromagnets are more common in nature than their ferromagnetic counter part and they operate at a much higher frequency in the terahertz (THz) ranges (Kimel et al., 2005; Satoh et al., 2010; Wienholdt et al., 2012), which makes it possible to perform ultrafast information processing and communication. As they do not create any stray fields, they are more robust against magnetic perturbations, which allows for a denser storage of components without undesired cross-talk between the active elements. In addition they have the possibility of generating large magnetotransport effects (Cheng et al., 2014). Already, theoretical and experimental work on antiferromagnetic spintronics have provided promising results for antiferromagnet-driven spin based devices. However, more information on spin transport for antiferromagnets is required before ferromagnet-free devices can be realized.

Recently, the theoretical work in antiferromagnetic spintronics has revolved around phenomena such as anisotropic magnetoresistance (AMR) (Martí et al., 2012; Wang et al., 2012) and spin transfer torques (STT) in AFMs (Haney and MacDonald, 2008; Xu et al., 2008; Swaving and Duine, 2011). The reciprocal effect to STT, called spin pumping, on the other hand has received far less attention (Cheng et al., 2014; Johansen and Brataas, 2017; Gulbrandsen and Brataas, 2017), possibly due to the naive conception that the vanishing magnetization of antiferromagnets spoils any spin pumping. Spin pumping (Brataas et al., 2002) is a mechanism where a pure spin current is injected into a normal metal by the magnetization of a magnet (at resonance) in contact with the metal (see Sec. 2.4).

Up until recent years, the contribution from cross-sublattice terms to the spin current pumped from a two-sublattice magnet has been disregarded. However, recent studies on such magnetic metals (Kamra and Belzig, 2017; Liu et al., 2017) suggest an important role for these terms. Since a spin current can be indirectly measured/detected through a voltage (Costache et al., 2006) induced by the inverse spin Hall effect (ISHE) (Saitoh and Miyajima, 2006), one obtains a way of investigating the effect of these cross-terms experimentally (see Sec. 2.4). Fig. 1.1 illustrates how such a voltage can be detected. This is the motivation behind this thesis, where the effect of cross-sublattice terms on the

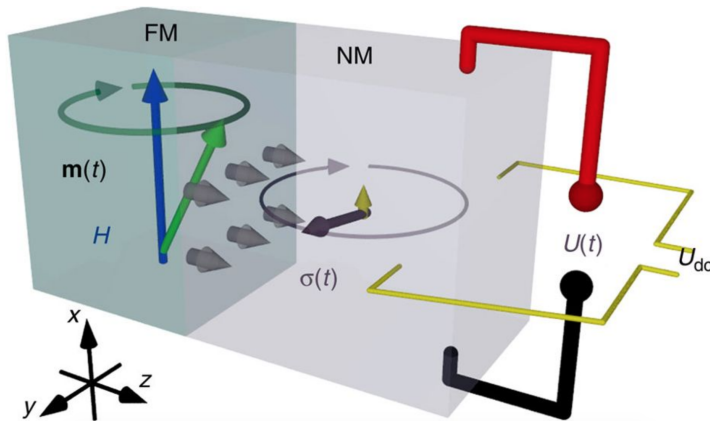


Figure 1.1: A schematic depiction of the detection of the induced inverse spin Hall effect voltage in a ferromagnetic/normal metal bilayer. Attaching probes to the edges of the normal metal (NM), one can measure both the ac and dc voltages induced by the ac- and dc-component of the spin current. The green, blue and grey arrows are the magnetization vector, the externally applied magnetic field and the spin pumping current, respectively. The spin current is polarized (black arrow) almost entirely in the yz -plane, with a small dc polarization component in the x -direction (yellow arrow). This figure is taken from (Wei et al., 2014).

spin pumping current from an antiferromagnet will be studied. The key goal is to identify, and make predictions for, experimentally available systems in which the effect of cross-sublattice terms can be unequivocally isolated from the intra-sublattice contributions.

1.2 Outline

In order for us to investigate spin transport by spin pumping, an understanding of the magnetostatics and magnetization dynamics of the system, and the basic mechanism of the spin pumping phenomenon is required. The thesis therefore has the following outline.

In chapter 2 a theoretical foundation of magnetization and spin dynamics is built. First (Sec. 2.1), magnetostatics is considered, providing a conceptual understanding of the mechanisms that contributes to the free energy of the system, which affects the magnetization dynamics. This is followed by a brief consideration of the configuration of the antiferromagnetic ground state for different applied fields. Then, the magnetization dynamics (Sec. 2.3 using the LLG-equation is discussed. Finally (Sec. 2.4), the mechanisms of spin pumping and ISHE are elucidated.

Chapter 3 is devoted to present and discuss the analytic and numerical results of the magnetization dynamics and spin pumping of the antiferromagnetic systems considered. The chapter is divided into three sections, one for each of the antiferromagnetic systems,

where results of the system are presented and discussed.

Finally a conclusion based on the findings in Sec. 3 and a very brief outlook are given in Sec. 4.

Theoretical background

This chapter provides a theoretical background describing the concepts of magnetization dynamics and spin pumping, important for understanding the results and discussion that follow in chapter 3. Section 2.1 is devoted to give a conceptual understanding of magnetic ordering in metals and the mechanisms that contribute to the free energy describing the antiferromagnetic systems considered in this thesis. The continuum approach is used to describe the magnetic properties of magnets and the effect of a static externally applied field. Then, a brief consideration of the antiferromagnetic ground state for different applied fields is considered in Sec. 2.2. In section 2.3, the dynamics of antiferromagnets are considered. A derivation of the Landau-Lifshitz-Gilbert (LLG) equation of motion for the magnetization, using a semi-classical approach, is given. We will see that the motion of the magnetization is determined by the various contributions to the free energy of the system. Spin waves are also considered briefly. The last section (2.4) explains the spin pumping mechanism in an antiferromagnetic/normal metal-bilayer. By employing an oscillating magnetic field a spin current can be injected into the normal metal by the magnet. This current can be detected by an electrical signal induced by the Inverse Spin Hall effect.

2.1 Magnetostatics

All materials can be classified into one of the following subgroups (Coey, 2009) - paramagnets, diamagnets, ferromagnets, antiferromagnets and ferrimagnets. Paramagnetic and diamagnetic materials are considered non-magnetic, as they do not contain magnetic ordering in the absence of an externally applied magnetic field. When such a field is applied, the constituent elementary magnetic moments can be oriented along the same (paramag-

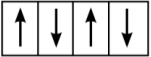
Type	Arrangement	Lattice	Resultant
Ferromagnetic	Alignment within lattice		
Antiferromagnetic	Sublattice, A & B, aligned but antiparallel equal		(none)
Ferrimagnetic	Sublattice, A & B, aligned but antiparallel unequal		

Figure 2.1: Schematic depiction of the magnetic structure at microscopic level, and the net moment for ferro-, ferri- and antiferromagnets. The illustration is adapted from (Kamra, 2015).

netism) or opposite (diamagnetism) direction of the applied field, and the material exhibits an induced net magnetic moment in this direction. Most materials fall under one of these two categories. The latter three subgroups however, do possess some sort of magnetic ordering. Ferromagnets can in the simplest case be considered to be composed of tiny magnetic moments on a lattice all pointing in the same direction, resulting in a large net magnetic moment in this direction (see Fig. 2.1). In antiferromagnets on the other hand, the magnetic moments can be seen to form two equivalent but oppositely oriented ferromagnetic sublattices. The magnetic moments will in this case cancel, thus leading to no net magnetic moment in spite of the ordered configuration at the microscopic level. Like antiferromagnets, ferrimagnets also consist of two interpenetrating ferromagnetic lattices oriented in the opposite direction. However, in this case the sublattices are inequivalent, giving rise to a net magnetic moment. In this thesis only antiferromagnets will be considered, but the ferromagnet is used to explain some of the phenomena. The spontaneous magnetization due to alignment of the atomic magnetic moments depends on temperature and falls precipitously to zero at the critical Curie temperature, T_C , for ferromagnets and the Néel temperature, T_N , for ferri- and antiferromagnets (Coey, 2009). At this critical temperature thermal agitation, inducing fluctuations of the moments, completely destroys the magnetic ordering and the material becomes paramagnetic.

The first modern theory explaining the spontaneous magnetic ordering of spins in ferromagnets was proposed by Pierre Weiss, in 1907 (Weiss, 1907). He supposed that a high internal molecular field, proportional to the magnetization of the ferromagnet, acts on the magnetic moments, but he could not explain the origin of this field. A few decades later the nature of magnetic ordering was explained by Heisenberg (Heisenberg, 1926) and Dirac (Dirac and Howard, 1926), in 1926. They attributed the ordering of spins to a quantum mechanical mechanism called the exchange interaction.

2.1.1 The exchange interaction

Quantum mechanical formulation

The exchange interaction, responsible for the ordering of the spin magnetic moments, is a consequence of the antisymmetry requirements on the fermionic many-particle wave function $\Psi(\mathbf{r}_1, \mathbf{r}_2, \dots, \mathbf{r}_N, s_1, s_2, \dots, s_N)$ of the electrons (at position \mathbf{r}_i with spin s_i). To elucidate how such a symmetry requirement can be responsible for the magnetic ordering, let's consider a system consisting of only two electrons in the presence of two interacting atom cores, as in the hydrogen molecule, H_2 .

Neglecting interaction between the electrons, the system can be modeled by the following Hamiltonian:

$$\hat{\mathcal{H}} = \hat{\mathcal{H}}_1 + \hat{\mathcal{H}}_2 + \hat{\mathcal{H}}_C, \quad (2.1)$$

where the two first terms are the single particle Hamiltonians of the electrons and the last term is the Coulomb potential from the ion cores. If electron 1 and 2 are located at the positions \mathbf{r}_1 and \mathbf{r}_2 respectively, the total spatial wave function of the system can be either symmetric, ϕ_s , or antisymmetric, ϕ_a , with respect to interchange of the electron positions ($\mathbf{r}_1 \leftrightarrow \mathbf{r}_2$). These are the two possible electron orbitals. The symmetric orbital has electrons piled up between the ion cores, while the antisymmetric orbital has the electrons piled up at the ion cores. Neglecting the effect of the Coulomb interaction term on the individual spatial wave functions ψ_1 and ψ_2 , the orbitals can be defined as (Blundel, 2001):

$$\phi_s = \frac{1}{\sqrt{2}}[\psi_1(\mathbf{r}_1)\psi_2(\mathbf{r}_2) + \psi_1(\mathbf{r}_2)\psi_2(\mathbf{r}_1)] \quad (2.2a)$$

$$\phi_a = \frac{1}{\sqrt{2}}[\psi_1(\mathbf{r}_1)\psi_2(\mathbf{r}_2) - \psi_1(\mathbf{r}_2)\psi_2(\mathbf{r}_1)]. \quad (2.2b)$$

Correspondingly, the spin states can be either symmetric or antisymmetric:

$$\chi_a = \frac{1}{\sqrt{2}}[\chi_{\uparrow\downarrow} - \chi_{\downarrow\uparrow}], \quad \chi_s = \begin{cases} \chi_{\uparrow\uparrow} \\ \frac{1}{\sqrt{2}}[\chi_{\uparrow\downarrow} + \chi_{\downarrow\uparrow}] \\ \chi_{\downarrow\downarrow} \end{cases}, \quad (2.3)$$

Here, $\chi_{\uparrow\downarrow}$ denotes the total spin state with electron 1 having up spin (\uparrow) and electron 2 having down spin (\downarrow), etc. The antisymmetric and symmetric states are called the singlet and triplet state, having total spin number $s = s_1 + s_2 = 0$ and $s = 1$, respectively. An-

tiparallel alignment of spins (*antiferromagnetism*) is therefore associated with the singlet state and parallel alignment (*ferromagnetism*) with the triplet state.

According to the Pauli exclusion principle, no two fermions can be in the same quantum state. Thus, the total wave function $\Psi = \phi(\mathbf{r}_1, \mathbf{r}_2)\chi$ has to be antisymmetric with respect to the permutation of two electrons (Bruus and Flensberg, 2002). This leaves only two possible combinations of the spatial wave function and the spin state, $\Psi_T = \phi_a\chi_s$ with energy ϵ_T and $\Psi_S = \phi_s\chi_a$ with energy ϵ_S (the subscripts T and S denote the triplet and singlet state respectively). If the spin states are properly normalized, the energy can be evaluated using Eq. (2.1):

$$\epsilon_{T,S} = \int \phi_{a,s}^*(\mathbf{r}_1, \mathbf{r}_2) \hat{\mathcal{H}}(\mathbf{r}_1, \mathbf{r}_2) \phi_{a,s}^*(\mathbf{r}_1, \mathbf{r}_2), \quad (2.4)$$

with an energy difference (Blundel, 2001)

$$\epsilon_T - \epsilon_S = 2 \int \psi_1^*(\mathbf{r}_1) \psi_2^*(\mathbf{r}_2) \hat{\mathcal{H}} \psi_2(\mathbf{r}_1) \psi_1(\mathbf{r}_2). \quad (2.5)$$

The total spin of the two-electron system can be represented by the operator $\hat{S} = \hat{S}_1 + \hat{S}_2$, such that $\hat{S}^2 = \hat{S}_1^2 + \hat{S}_2^2 + 2\hat{S}_1 \cdot \hat{S}_2$ (Hemmer, 2005). Acting with this operator on the two possible states gives:

$$\hat{S}^2 \Psi_S = 0 \quad (2.6)$$

$$\hat{S}^2 \Psi_T = 2\hbar^2 s(s+1) \Psi_T = 2\hbar^2 \Psi_T. \quad (2.7)$$

Using this, the Hamiltonian in Eq. (2.1) can be re-written as:

$$\hat{\mathcal{H}} = \epsilon_T + \frac{\epsilon_T - \epsilon_S}{2\hbar^2} \hat{S}^2 \quad (2.8)$$

$$\begin{aligned} &= \epsilon_T + \frac{\epsilon_T - \epsilon_S}{2\hbar^2} (\hat{S}_1^2 + \hat{S}_2^2 + 2\hat{S}_1 \cdot \hat{S}_2) \\ &= \frac{1}{4}(\epsilon_S + 3\epsilon_T) + \frac{(\epsilon_T - \epsilon_S)}{\hbar^2} \hat{S}_1 \cdot \hat{S}_2, \end{aligned} \quad (2.9)$$

where $s_1 = s_2 = 1/2$ for electrons has been used. From Eq. (2.9) we see, apart from a constant energy term, that the physics of the direct exchange interaction originates from spin-spin interaction. The Hamiltonian, called the exchange Hamiltonian, is usually written as:

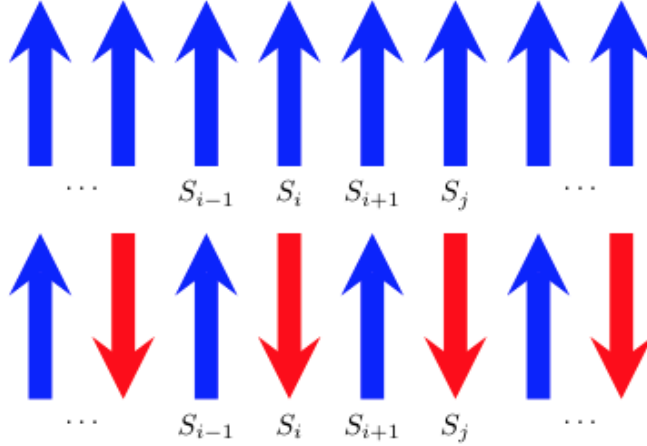


Figure 2.2: Schematic depiction of a 1D lattice of spins exhibiting ferromagnetic (top) and antiferromagnetic (bottom) ordering of spins. The spin at lattice site i interacts with the spin at lattice site j .

$$\hat{\mathcal{H}} = -2J\hat{\mathbf{S}}_1 \cdot \hat{\mathbf{S}}_2, \quad (2.10)$$

where $J = (\epsilon_S - \epsilon_T)/\hbar^2$ is the exchange integral. If $\epsilon_T > \epsilon_S$, J is negative, and the singlet state is favored resulting in antiferromagnetic ordering of spins. If $\epsilon_T < \epsilon_S$, J is positive, and the triplet state is favored giving ferromagnetic ordering. Generalizing this to a many-body system is highly non-trivial and beyond the scope of this thesis. Nevertheless, a good insight into the effect of the exchange interaction in a bulk material can be captured by the the following Hamiltonian:

$$\hat{\mathcal{H}} = - \sum_{i,j} J_{ij} \hat{\mathbf{S}}_i \cdot \hat{\mathbf{S}}_j \quad (2.11)$$

and was first introduced by Heisenberg in 1926. Here, J_{ij} is the exchange integral between the i^{th} and j^{th} lattice site (see Fig. 2.2), and the summation is taken doubly over all possible electron pairs. From Eq. (2.5) we can see that the exchange integral J is dependent on the overlap of the electron wave functions. The exchange interaction is therefore short ranged. Thus, in many cases it is sufficient to execute the summation over nearest neighbour spins.

Continuum formulation

In the Landau-Lifshitz phenomenology, the dynamics of the magnet are described by using a continuum model. We then leave the microscopic picture of the elementary magnetic moments, $\boldsymbol{\mu}$, and enter the macroscopic picture, described by the magnetization $\boldsymbol{M} = \sum_{\Delta V} \boldsymbol{\mu} / \Delta V$ ($\sum_{\Delta V} \boldsymbol{\mu}$ is the magnetic moment of a small but macroscopic volume). Assuming constant exchange integral, the contribution from the exchange interaction to the free energy of the magnet, in the macroscopic limit, can be expressed as:

$$E^{ex} = -J \boldsymbol{M}_i \cdot \boldsymbol{M}_j, \quad (2.12)$$

where i and j now denote the sublattice magnetizations. The continuum approach allows for the use of classical theory, hence the magnetization is considered a classical vector. For a ferromagnet there is only one sublattice and the exchange energy is then proportional to M^2 .

2.1.2 Anisotropy

So far we have seen that the exchange interaction leads to ferromagnetic or antiferromagnetic alignment of spins. However, it does not explain why the spins tend to align in fixed directions in a magnetic sample in the absence of externally applied fields. This phenomenon is called magnetic anisotropy and is largely due to sample shape, crystal structure and atomic or micro-scale textures (Coey, 2009). We will only consider one type of anisotropy related to the crystal structure of the magnet, called magnetocrystalline anisotropy.

Magnetocrystalline anisotropy is an intrinsic property of a magnetic crystal, rendering the magnetic properties of the solid dependent on the direction of the magnetization relative to one or more of the crystallographic axes. This form of anisotropy originates from crystal-field interaction and spin-orbit interaction (single-ion anisotropy), or else the dipole-dipole interaction between atoms on the crystal lattice (two-ion anisotropy). In the case of single-ion anisotropy, the electrostatic interaction with the ions tend to stabilize a particular orbital of the electrons. The ordering of the orbital, and therefore also the angular magnetic moment of the ion, becomes dependent on the ordering of the crystal lattice. Since spin and orbital magnetic moment interact with each other (spin-orbit coupling), the net moment is aligned in a particular crystallographic direction. The energy of the net moment of the ion then depends on its orientation with respect to the major axes of the crystal. This orientation-dependent contribution to the total free energy of the system is called the magneto-crystalline anisotropy energy. If the energy is only dependent on the

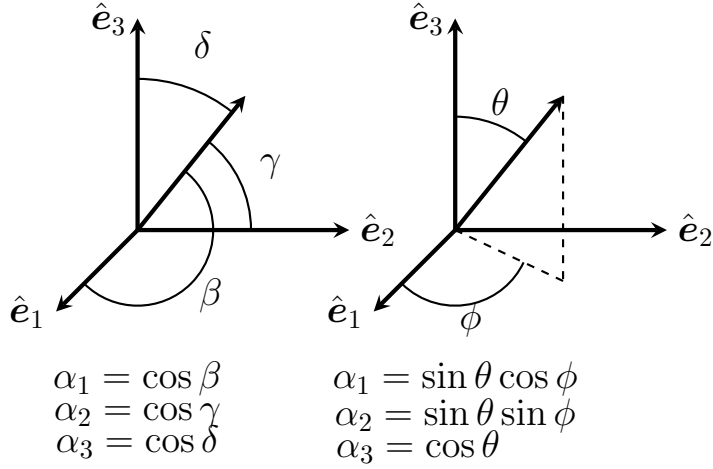


Figure 2.3: Definitions of the directional cosines.

orientation relative to one axis, the crystal has uniaxial anisotropy. This axis can either correspond to a maximum (hard axis) or minimum in energy (easy axis).

Assuming that the crystal has a symmetry in energy along an easy axis, the energy density of the magnetocrystalline anisotropy for a ferromagnet can be expressed as an even power series in $\sin \theta$ (Stancil and Prabhakar, 2009):

$$E_{ua} = K_{u1} \sin^2 \theta + K_{u2} \sin^4 \theta + \dots, \quad (2.13)$$

where θ is the angle between the magnetization and the easy axis, and $K_{u1} > 0$ is a constant. From Eq. (2.13) it is easy to see that the energy is minimized for $\theta = 0$. Thus, for uniaxial anisotropy it is energetically favorable for the magnetization to align along the direction of the easy axis. For convenience this can be expressed in terms of directional cosines $\alpha_i = M_i/M_0$, where M_i is the component of the magnetization along the i^{th} axis and M_0 is the saturation magnetization. Let the e^3 -axis be the axis of symmetry (see Fig. 2.3). To lowest order, the energy density can be written as:

$$E_{ua} = K_{u1} \left(1 - \frac{M_3^2}{M_0^2} \right). \quad (2.14)$$

..

Since an antiferromagnet can be considered as two interpenetrating ferromagnetic lattices, the magnetocrystalline energy density of a uniaxial antiferromagnet can be written as:

$$E_{ua} = K_A \left(1 - \frac{M_{A3}^2}{M_{A0}^2} \right) + K_B \left(1 - \frac{M_{B3}^2}{M_{B0}^2} \right), \quad (2.15)$$

where the subscripts A and B denote the two sublattices.

2.1.3 Zeeman energy

As mentioned earlier, applying a magnetic field can change the direction of the magnetic moments of a material from their original orientations. Let's first consider the magnetization of a ferromagnet in the continuum limit, \mathbf{M} , in the presence of a static magnetic field, \mathbf{H} , applied in some arbitrary direction (see Fig. 2.4). Let's also neglect any magnetic anisotropies for simplicity, which ultimately play an important role in the orientation of the magnetization. The magnetization experiences a torque, $\boldsymbol{\tau}$, from the field,

$$\boldsymbol{\tau} = \mathbf{M} \times \mu_0 \mathbf{H}, \quad (2.16)$$

rotating the magnetization in the direction of the applied field. The torque does work

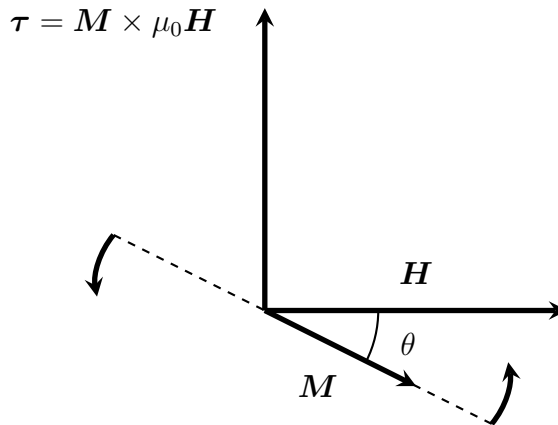


Figure 2.4: Schematic depiction of the torque, $\boldsymbol{\tau}$, acting on the magnetization, \mathbf{M} , of a ferromagnet by a magnetic field, \mathbf{H} , applied with an angle θ with respect to the magnetization direction. The torque bends the magnetization in the direction of the applied field.

on the magnetization which we know from classical mechanics can be calculated as the integral of Eq. (2.16). Choosing $\theta = 0$ as the reference state, where θ is the angle between \mathbf{M} and \mathbf{H} , the potential energy of the magnetization is:

$$\begin{aligned}
E_m &= \int_0^\theta \mathbf{M} \times \mu_0 \mathbf{H} d\theta' \\
&= -\mu_0 \mathbf{M} \cdot \mathbf{H},
\end{aligned}
\tag{2.17}$$

where a constant term has been neglected. This is called the Zeeman energy of the ferromagnet. Here we have assumed that the torque has no other effect on the magnetization other than rotating it and that the sources of \mathbf{H} are unchanged. From Eq. (2.17) it is easy to see that it is energetically favorable for the magnetization to align in the direction of the applied field.

Applying a magnetic field to an antiferromagnet at temperatures below the Néel point, is far more complicated than for a ferromagnet, at temperatures below the Curie point, because the direction in which the field is applied is crucial. For the two-sublattice antiferromagnet, the torque acts on both sublattice magnetizations. The Zeeman energy is in this case:

$$E_m = -\mathbf{H} \cdot (\mathbf{M}_A + \mathbf{M}_B).$$
(2.18)

For applied fields along the easy axis there is no energetically favorable configuration. Since the sublattice magnetizations point in the opposite direction, the decrease in the potential energy of one sublattice is canceled by the increase in energy of the other. Hence, there is no energetic advantage to align with the applied field. The torque on the magnetization vectors is in this case zero, such that the sublattice magnetizations keep their antiparallel alignment. However, if the field is applied with some angle to the antiferromagnetic configuration, the magnetization can reduce its energy by tilting towards the applied field such that it subtends an angle from its original position (see Fig. 2.5e). In this thesis, the magnetic field is applied in the direction of the easy axis for all systems considered. For sufficiently low fields the antiparallel alignment remains unchanged.

2.2 Antiferromagnetic ground state

Before introducing magnetization dynamics, we consider briefly the configuration of the sublattice magnetizations of the antiferromagnet in the ground state. Their orientation is determined by the subtle interplay of the different energy contributions to the free energy. In addition to the mechanisms cover in the previous section, the possible contributions to the free energy (Chikazumi, 1997) are from magnetostatic energy and magneto-elastic

coupling energy. However, in this thesis we will only consider contributions from the Zeeman, exchange and anisotropy energies.

In the absence of externally applied fields, the orientation of spins, below the critical Néel temperature, is determined by an exchange dominated energy minima, giving antiparallel alignment of spins. The direction of orientation relative to the crystal axis is governed by a minima in the anisotropy energy, as we have seen in the previous section. The ground state of the antiferromagnet, corresponding to a minimum in the total free energy of the system, is then described by antiparallel alignment of the sublattice magnetizations, $M_A = -M_B$ with magnitude M_0 (saturation magnetization), along the easy axis.

Applying a magnetic field changes the energy of the system such that a new ground state configuration is obtained. The configuration of the sublattice magnetizations for low fields is covered in the discussion of the Zeeman energy above. If the applied field is sufficiently large however, it will eventually dominate any internal fields forcing all the magnetic moments to align parallel with the applied field. The transition to this state, called the spin flip state, as the magnetic field is increased, is strongly dependent on the direction of the field relative to the initial directions of the sublattice magnetizations. Consider an antiferromagnet at $T = 0$, such that thermal fluctuations can be ignored. If we apply a field perpendicular to the easy axis, the magnetic moments will only bend more and more in the direction of the magnetic field as the field is increased (see Fig. 2.5e), until it reaches the spin flip state at a critical field value, H_{\perp} . If the field is applied parallel to the the easy axis instead, interesting things happen. At low fields, the direction of the moments are unchanged. However, when the field reaches a critical value, it will overtake the exchange interaction and the system snaps into a different configuration (see Fig. 2.5b). This is called the spin flop transition. Increasing the field further decreases the angle between the sublattice magnetizations and the magnetic field direction. For ferromagnets there is no spin flop state, since all spins are aligned in the same direction.

The equilibrium configuration (ground state) of the antiferromagnetic system, in the spin flip and spin flop states, can readily be calculated by minimizing the free energy with respect to the angle subtended by the sublattice magnetizations. This amounts to solving the equations:

$$\frac{\partial F}{\partial \theta} = 0 \tag{2.19}$$

$$\frac{\partial F}{\partial \phi} = 0, \tag{2.20}$$

where F is the free energy, and θ and ϕ are the angles subtended by M_A and M_B , respectively. The critical field, at which spin flop occurs, can be found by taking the derivative of Eqs. (2.19) and (2.20) and solve for the applied field, since the transition occurs when the total energy reaches an unstable equilibrium (Chikazumi, 1997).

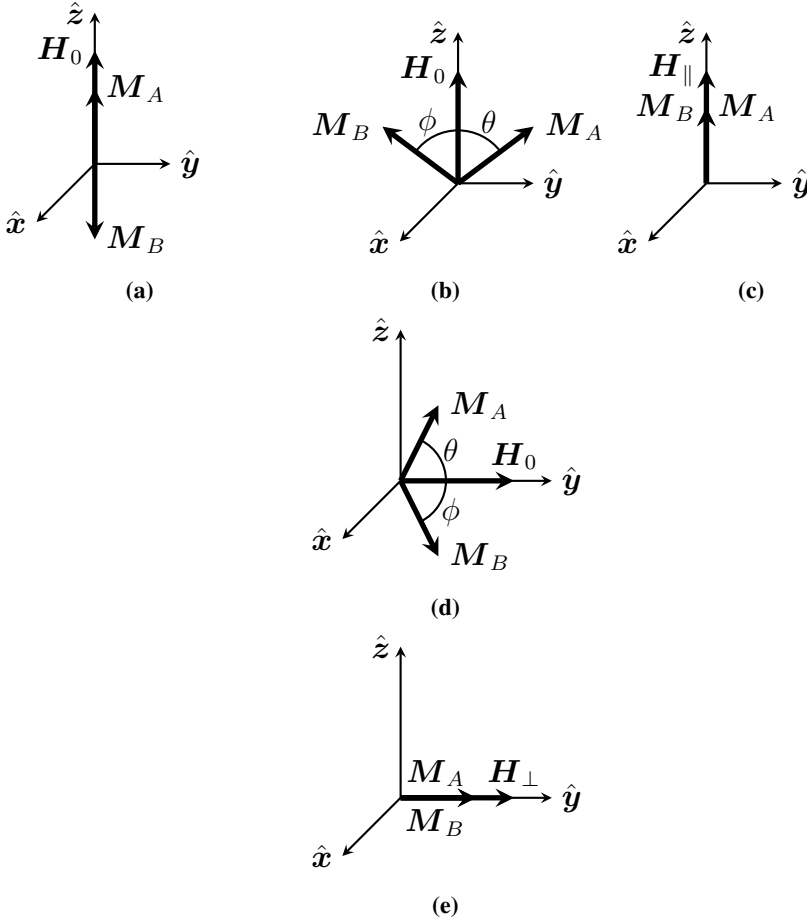


Figure 2.5: Schematic depiction of the ground state configurations of an antiferromagnet with easy axis anisotropy in a static applied field. (a) For a sufficiently low magnetic field applied along the easy axis, the collinear ground state remains unchanged. (b) With growing field, the transition to the spin flop state occurs. (c) Increasing the field further decreases the angle between magnetization vectors, and at a critical field, $H_0 = H_{\parallel}$, the spin flip transition occurs. (d) Applying a magnetic field along a hard axis (perpendicular to the easy axis) decreases the angle between M_A and M_B for increasing field, H_0 . (e) At a critical value, $H_0 = H_{\perp}$, the spin flip transition occurs.

2.3 Magnetization dynamics

The magnetic moment of the electron is a purely quantum mechanical property. Thus, the dynamical motion of the magnetic moments can only rigorously be described by quantum mechanics. However, for the relevant dynamic processes in many spin dynamic phenomena, the continuum approach can be used. At the macroscopic level, ferro-, ferri- and antiferromagnets are well described by the Landau-Lifshitz equation of motion for the magnetization (Gurevich and Melkov, 1996). In the Landau-Lifshitz phenomenology, the free energy of the system is expressed in terms of the magnetization guided by the microscopic origin of the energy contributions and the general symmetry requirements. Thus, the magnetization dynamics of the system may be fully described in terms of the free energy of the magnet.

We first derive the LLG-equation for a ferromagnet in 2.3.1 and extend the formalism to antiferromagnets in 2.3.2.

2.3.1 The Landau-Lifshitz equation of motion

Consider first an electron with magnetic moment $\boldsymbol{\mu}$ in an external magnetic field \mathbf{H}_{ext} . From classical mechanics, it is known that the torque experienced by the magnetic moment:

$$\boldsymbol{\tau} = \boldsymbol{\mu} \times \mu_0 \mathbf{H}_{ext}, \quad (2.21)$$

where μ_0 is the magnetic permeability, is equal to the rate of change of its angular momentum:

$$\frac{d\mathbf{J}}{dt} = \boldsymbol{\mu} \times \mu_0 \mathbf{H}_{ext}. \quad (2.22)$$

Employing the relation between the magnetic moment and the magnetization, $\mathbf{J} = -\gamma\boldsymbol{\mu}$, well known from quantum mechanics (Coey, 2009), we obtain the Landau-Lifshitz equation of motion for the macroscopic magnetization:

$$\frac{d\mathbf{M}}{dt} = -\gamma \mathbf{M} \times \mu_0 \mathbf{H}_{ext}. \quad (2.23)$$

Here, γ is a constant known as the gyromagnetic ratio given by $\gamma = g\mu_B/\hbar$, where g is the electron g-factor, μ_B is the Bohr magneton and \hbar is Plank's constant. Multiplying this equation by \mathbf{H}_{ext} and \mathbf{M} on both sides respectively, we find $\partial_t(\mathbf{M} \cdot \mathbf{H}_{ext}) = 0$ and $\partial_t(\mathbf{M}^2) = 0$, implying that the magnetization precess around the vector field \mathbf{H}_{ext} with constant cone angle and that the length of \mathbf{M} is conserved. Other sources of angular

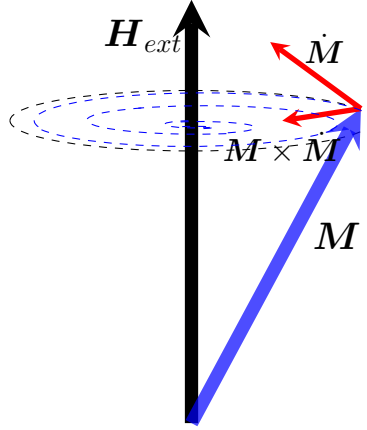


Figure 2.6: Schematic depiction of the precession of the magnetization \mathbf{M} (blue vector) due to an externally applied field \mathbf{H}_{ext} (black vector). The Gilbert damping term causes the magnetization vector to spiral down to the equilibrium magnetization direction, indicated by the dashed blue line.

momentum to the system, from i.e. spin transfer, may be included in the equation by adding the experienced torque by the magnetization on the right hand side of Eq. (2.23).

Damped motion

Constant cone angle means that the equation conserves energy, but this is not consistent with experience, since after sufficient time the magnetization will return to its equilibrium position (parallel to \mathbf{H}_{ext}) (see Fig. 2.6). The interaction of the system with its 'surroundings' and the subsequent energy loss can be described by including a phenomenological damping term parameterized by the Gilbert damping constant α . This yields the Landau-Lifshitz-Gilbert (LLG) equation of motion,

$$\frac{d\mathbf{M}}{dt} = -\gamma \mathbf{M} \times \mu_0 \mathbf{H}_{ext} + \frac{\alpha}{M_0} \left(\mathbf{M} \times \frac{d\mathbf{M}}{dt} \right). \quad (2.24)$$

On the right hand side of Eq. (2.24), the first term describes the precession of the magnetization, while the second term describes the relaxation of this motion. The Gilbert damping term can be interpreted as a torque reducing the angular momentum and energy of the system. As time passes, the magnetization will therefore spiral down until it aligns with the applied field. From energy and angular momentum conservation, the energy and angular momentum difference must be transferred to some other reservoir, which ultimately will be the lattice in the absence of any other dissipation channels. This is called spin-lattice relaxation (Manenkov and Orbach, 1966). The magnetization dynamics can therefore be

understood as energy and angular momentum flow between the various sub-systems, with a dissipation channel leaking energy and angular momentum to the 'surroundings'.

The Lagrangian formalism: Free energy

If the magnetization in a relatively large system is spatially varying, angular momentum can flow between different parts of the same magnetic sub-system that are separated in space. The most convenient way of deriving the equation of motion is then by using the Lagrangian formalism for classical fields (Gilbert, 2004; Yan et al., 2013), since the magnetization now is dependent on its position in the spin system. Solving the Euler-Lagrange's equations:

$$\frac{d}{dt} \frac{\partial \mathcal{L}[M, \dot{M}]}{\partial \dot{M}} - \frac{\partial \mathcal{L}[M, \dot{M}]}{\partial M} = 0 \quad (2.25)$$

for the Lagrangian:

$$\mathcal{L} = T(M, \dot{M}) - F(M, \dot{M}), \quad (2.26)$$

where T and F are the kinetic and free energies of the magnetization respectively, one obtains:

$$\dot{M} = -\gamma M \times \mu_0 H_{eff}, \quad (2.27)$$

for the magnetization $M = M(\mathbf{r})$. The effective field, H_{eff} , is related to the free energy by the functional derivative:

$$\mu_0 H_{eff} = -\frac{\delta F}{\delta M} = -\sum_{n=x,y,z} \frac{\delta F}{\delta M_n}. \quad (2.28)$$

A derivation of the LLG-equation from the Lagrangian formalism is given in A. 4.2. Since Eq. (2.31) is a continuous system analogue to Eq. (2.23), it can be interpreted in a similar fashion, where the magnetization experience a torque, $M \times \delta F/\delta M$, exerted by all the contributors to the free energy.

Damping can be introduced through the Rayleigh dissipation functional:

$$\mathcal{R} = \frac{\alpha}{2\gamma M_0} \int_V \frac{dM}{dt} \cdot \frac{dM}{dt} d^3r. \quad (2.29)$$

Adjusting the Euler-Lagrange's equations for the functional:

$$\frac{d}{dt} \frac{\delta \mathcal{L}[\mathbf{M}, \dot{\mathbf{M}}]}{\delta(d\mathbf{M}/dt)} - \frac{\delta \mathcal{L}[\mathbf{M}, \dot{\mathbf{M}}]}{\delta \mathbf{M}} + \frac{\delta \mathcal{R}[\mathbf{M}, \dot{\mathbf{M}}]}{\delta(d\mathbf{M}/dt)} = 0, \quad (2.30)$$

one obtains the Landau-Lifshitz-Gilbert equation:

$$\dot{\mathbf{M}} = -\gamma \mathbf{M} \times \mu_0 \mathbf{H}_{eff} + \frac{\alpha}{M_S} \left(\mathbf{M} \times \dot{\mathbf{M}} \right), \quad (2.31)$$

Similarly, the damping term can be interpreted as a torque draining angular momentum from the spin system.

2.3.2 Spin wave theory for antiferromagnets

The Landau-Lifshitz-Gilbert equations of motion for antiferromagnets

Let's now turn to antiferromagnetic systems described by some free energy F . Since an antiferromagnet can be considered as two interpenetrating ferromagnetic sublattices, with sublattice magnetization \mathbf{M}_A and \mathbf{M}_B , the LL-equations for antiferromagnets read:

$$\dot{\mathbf{M}}_A = -\gamma_A \mathbf{M}_A \times \mathbf{B}_A \quad (2.32)$$

$$\dot{\mathbf{M}}_B = -\gamma_B \mathbf{M}_B \times \mathbf{B}_B, \quad (2.33)$$

where $\mathbf{B}_A = -\delta F / \delta \mathbf{M}_A$ and γ_A , and $\mathbf{B}_B = -\delta F / \delta \mathbf{M}_B$ and γ_B are the effective fields and gyromagnetic ratios of sublattice A and B. Up until recently, it has been the consensus that the damping of the motion of the sublattice magnetizations only has contributions from intra-sublattice terms:

$$\frac{\alpha_A}{M_{A0}} \left(\mathbf{M}_A \times \dot{\mathbf{M}}_A \right) \quad \text{and} \quad \frac{\alpha_B}{M_{B0}} \left(\mathbf{M}_B \times \dot{\mathbf{M}}_B \right), \quad (2.34)$$

where M_{A0} and M_{B0} are the saturation magnetizations. However, recent theoretical results on spin pumping in two-sublattice magnets (Kamra and Belzig, 2017) and damping in AFMs (Liu et al., 2017) suggest an important role for the previously disregarded cross-sublattice terms in Gilbert damping. Including cross-sublattice damping, the LLG-equations for an antiferromagnet become (Kamra et al., 2018):

$$\dot{\mathbf{M}}_A = -\gamma_A \mathbf{M}_A \times \mathbf{B}_A + \frac{\alpha_{AA}}{M_{A0}} \left(\mathbf{M}_A \times \dot{\mathbf{M}}_A \right) + \frac{\alpha_{AB}}{M_{A0}} \left(\mathbf{M}_A \times \dot{\mathbf{M}}_B \right) \quad (2.35)$$

$$\dot{\mathbf{M}}_B = -\gamma_B \mathbf{M}_B \times \mathbf{B}_B + \frac{\alpha_{BB}}{M_{B0}} \left(\mathbf{M}_B \times \dot{\mathbf{M}}_B \right) + \frac{\alpha_{BA}}{M_{B0}} \left(\mathbf{M}_B \times \dot{\mathbf{M}}_A \right), \quad (2.36)$$

where α_{ij} are the Gilbert damping parameters. In accordance with the interpretation in the ferromagnetic case, the new damping terms can be considered as torques exerted by the sublattice magnetizations on each other. Eqs. (2.35) and (2.36) can be conveniently expressed in unit vector form, noting that $\mathbf{M}_{A,B} = M_{A0,B0} \hat{\mathbf{m}}_{A,B} = M_0 \hat{\mathbf{m}}_{A,B}$ and $\gamma_A = \gamma_B = \gamma$ for symmetric antiferromagnets:

$$\dot{\hat{\mathbf{m}}}_A = -\gamma \hat{\mathbf{m}}_A \times \mu_0 \mathbf{B}_A + \alpha_{AA} \left(\hat{\mathbf{m}}_A \times \dot{\hat{\mathbf{m}}}_A \right) + \alpha_{AB} \left(\hat{\mathbf{m}}_A \times \dot{\hat{\mathbf{m}}}_B \right) \quad (2.37a)$$

$$\dot{\hat{\mathbf{m}}}_B = -\gamma \hat{\mathbf{m}}_B \times \mu_0 \mathbf{B}_B + \alpha_{BB} \left(\hat{\mathbf{m}}_B \times \dot{\hat{\mathbf{m}}}_B \right) + \alpha_{BA} \left(\hat{\mathbf{m}}_B \times \dot{\hat{\mathbf{m}}}_A \right). \quad (2.37b)$$

Spin wave excitation

For a static applied field, the magnetization will start to precess and spiral down to the equilibrium configuration after some time by transfer of angular momentum. Some of the angular momentum will be transferred between neighboring spins creating short lived spin waves in the magnet. Since the spin waves are short lived, static fields alone are of little interest in spin dynamics. If we instead apply an oscillating magnetic field, spin waves propagating through the entire bulk material can be excited (Coey, 2009). These spin waves can be thought of as periodic oscillations in the relative orientation of the lattice spins (see Fig. 2.7). Recall that the magnetization is the net magnetic moment per volume. The motion of the spin waves is therefore described by the LLG-equations for sufficiently small oscillations of the applied field in the continuum limit. The spin wave depicted in the figure has a nonzero wave vector, \mathbf{k} . We will only consider uniform modes with $\mathbf{k} = 0$, where there is no phase difference between the rotation of the magnetic moments.



Figure 2.7: Illustration of a spin wave. The relative motion of the electron magnetic moments (black arrows) creates a wave (a magnon) illustrated by the red curve.

Consider an antiferromagnet exposed to an oscillating magnetic field. Assuming small

time-variations, the fields can be considered as a sum of a static part and a small perturbation, which can be expressed as:

$$\mathbf{H} = \mathbf{H}_0 + \mathbf{h}(t), \quad H_0 \gg |\mathbf{h}(t)|. \quad (2.38)$$

$$\mathbf{M}_{A,B} = \mathbf{M}_0 + \mathbf{m}_{A,B}(t), \quad M_0 \gg |\mathbf{m}_{A,B}(t)|. \quad (2.39)$$

The modulus of the magnetization vector is then approximately constant to first order in the small perturbation and the LLG-equations can be employed. Given the free energy of the system, Eqs. (2.37a) and (2.37b) can be solved for the time-varying magnetization components. Assuming harmonic oscillations of the fields, i.e. $\mathbf{h} = \hat{\mathbf{h}}e^{i\omega t}$ and $\mathbf{m}_{A,B} = m_{A,B}e^{i\omega t}$ where $\hat{\mathbf{h}}$ and $m_{A,B}$ are complex amplitudes, Eqs. (2.37a) and (2.37b) become:

$$i\omega \hat{\mathbf{m}}_A = -\gamma \hat{\mathbf{m}}_A \times \mathbf{B}_A + i\omega \alpha_{AA} \left(\hat{\mathbf{m}}_A \times \dot{\hat{\mathbf{m}}}_A \right) + i\omega \alpha_{AB} \left(\hat{\mathbf{m}}_A \times \dot{\hat{\mathbf{m}}}_B \right) \quad (2.40a)$$

$$i\omega \hat{\mathbf{m}}_B = -\gamma \hat{\mathbf{m}}_B \times \mathbf{B}_B + i\omega \alpha_{BB} \left(\hat{\mathbf{m}}_B \times \dot{\hat{\mathbf{m}}}_B \right) + i\omega \alpha_{BA} \left(\hat{\mathbf{m}}_B \times \dot{\hat{\mathbf{m}}}_A \right). \quad (2.40b)$$

Without assuming the form of the free energy, solving the system of coupled equations gives a general solution on the form:

$$\begin{bmatrix} \hat{\mathbf{m}}_A \\ \hat{\mathbf{m}}_B \end{bmatrix} = \hat{\chi}(\omega) \begin{bmatrix} \hat{\mathbf{h}} \\ \hat{\mathbf{h}} \end{bmatrix}, \quad (2.41)$$

where m_B , m_A and $\hat{\mathbf{h}}$ are column vectors of the components of the time-varying fields. In the general solution, $\hat{\chi}(\omega)$, is a 4x4 tensor called the dynamical susceptibility tensor and contains the information of the dynamics of the magnetization and thereby the spin waves. The tensor consists of both real and imaginary components. The imaginary part is of particular interest in damping experiments (Mizukami and Miyazaki, 2001; Gilbert, 2004; Oogane et al., 2006), as information about the damping behaviour of the magnetization is contained in this component (Vacus and Vukadinovic, 2005). For the simplest systems it is possible to obtain decoupled equations by expressing the magnetization components in a particular basis. The solution can then be written as two matrix equations, one for each component in the chosen basis $\{i, j\}$:

$$\begin{bmatrix} m_{A_{i,j}} \\ m_{B_{i,j}} \end{bmatrix} = \hat{\chi}_{i,j}(\omega) \begin{bmatrix} \hat{h}_{i,j} \\ \hat{h}_{i,j} \end{bmatrix}. \quad (2.42)$$

The susceptibility tensor $\hat{\chi}_{i,j}(\omega)$ is then 2x2 matrices.

If the antiferromagnet is in contact with another metal, the spins at the interface can interact with the electrons in the normal metal. This will be the focus of the next section.

2.4 Spin dynamics in antiferromagnet/normal metal bilayers

When a dynamic antiferromagnet (a magnet with oscillating magnetization) is put in contact with a normal metal (paramagnetic material), angular momentum can be transferred between the two materials creating a spin current in the adjacent metal. A rigorous theory of this interfacial effect for ferromagnet/normal metal layers, called spin pumping, was developed by Tserkovnyak et. al (Tserkovnyak et al., 2002a; Tserkovnyak and Halperin, 2005), enabling a new method to develop energy efficient technology. Later, an equivalent theory for antiferromagnet/normal metal layers was proposed by Cheng et. al (Cheng et al., 2014). The injected spin current induces an electrical current, due to the Inverse Spin Hall effect, which can be measured experimentally. This provides a way of reading quantum information stored in a magnet, rendering spin pumping a possible tool to be employed in quantum computing.

To elucidate the mechanisms of the two mentioned phenomena, a bilayer consisting of an antiferromagnetic insulator in contact with a normal metal is considered (see Fig. 2.8). When the two layers are connected, the electrons at the normal metal-interface are exchange coupled to the itinerant electron spins in the antiferromagnet. The interface electrons will then adiabatically adapt to the instantaneous configuration of the antiferromagnetic magnetic moments (Cheng et al., 2014). The normal to the interface is in the x-direction, while the z-direction is parallel to the interface, as shown in the figure. The length, L , of the metal is assumed much larger than the thickness, t_N , where the thickness is measured in the x-direction and the length in the y-direction. The antiferromagnetic layer is assumed to be a compensated magnet, meaning that it consists of two interpenetrating ferromagnetic sublattices described by the macroscopic magnetizations \mathbf{M}_A and \mathbf{M}_B , where $|\mathbf{M}_A| = |\mathbf{M}_B|$. The free energy is considered arbitrary, except for that the easy axis of the magnet is assumed to be in the z-direction.

Now, consider applying an oscillating external magnetic field with a large static part (dc-part) directed along the easy axis of the AFM, and a small ac-part exhibiting harmonic oscillations in the xy-plane. The sublattice magnetization will then start to precess, producing uniform spin waves in the magnet. These spin waves pumps a spin current into the nonmagnetic material.

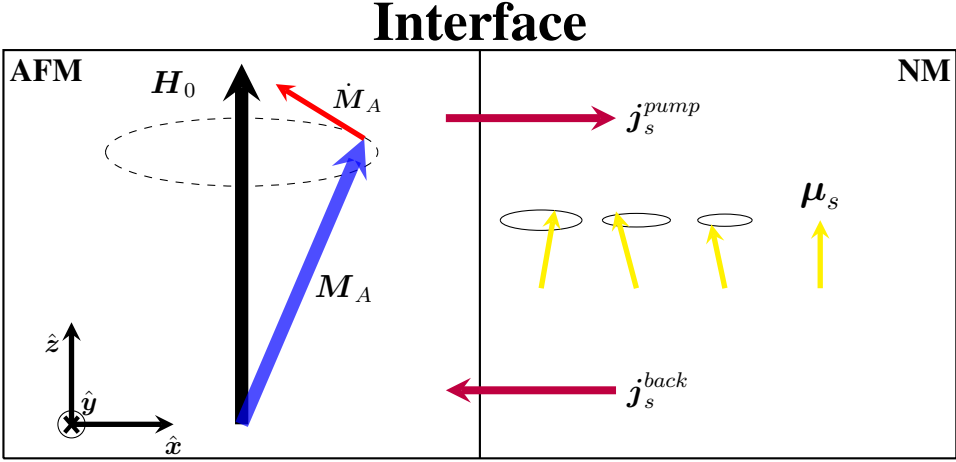


Figure 2.8: Schematic depiction of spin pumping in a antiferromagnet/normal metal bilayer (AFM/NM-layer) from one of the sublattice magnetizations driven into uniform oscillations by an applied ac-field. Note that both sublattice magnetizations contributes to the injected current. The oscillating sublattice magnetization, M_A , pumps a spin current into the normal metal, creating a spin accumulation density, μ_N at the interface. The spin density diffuses into the metal, driving the spin pumping current j_s^{pump} , and back into the magnet, causing spin back-flow, j_s^{back} . The polarization, \hat{s} , of the spin current is illustrated by the yellow arrows. The field, H_0 , is the static part of the applied field.

2.4.1 Spin pumping

The fundamental mechanism of spin pumping can be explained by a dynamic magnetization that transfers angular momentum to the electrons in the normal metal by exerting a torque on the spins. This changes the spin polarization of the electrons, which originally was arbitrary, to point in the same direction. Conservation of angular momentum ensures that the spins are polarized perpendicular to the magnetization, \mathbf{m} , and its rate of change, $\dot{\mathbf{m}}$. Previously, it was naively thought that the spin pumped from an antiferromagnet vanishes due to cancellation of the contributions from the antiparallel sublattice magnetizations. However, as described by Cheng et al. (Cheng et al., 2014) using a scattering matrix approach, the contributions to the spin current from the sublattices add constructively. They find, in accordance with (Jia et al., 2011), that the spin transfer in AFM|NM is as efficient as in FM|NM.

The spin pumping current can be expressed as:

$$j_s^0 \hat{s} = \frac{\hbar}{4\pi} \text{Re}(g^{\uparrow\downarrow}) \left(\hat{m}_A \times \dot{\hat{m}}_A + \hat{m}_B \times \dot{\hat{m}}_B \right), \quad (2.43)$$

where $\hat{\mathbf{m}}_{A,B}$ are the unit vector magnetizations, $\hat{\mathbf{s}}$ is the unit vector of the spin current polarization and $Re(g^{\uparrow\downarrow})$ is the real part of the spin-mixing conductance. The mixing conductance is a material parameter that describes the spin transport in the nonmagnet. The full expression also contains the imaginary part of the spin-mixing conductance, however the real part typically dominates the imaginary part and it can therefore be neglected (Cheng et al., 2014). Note that the vectors $(\hat{\mathbf{m}}_{A,B} \times \dot{\hat{\mathbf{m}}}_{A,B})$ are time-dependent due to the precessing nature of the magnetization, indicating time-dependent spin polarization. However, the z-component of the vector product, which is in the direction of the equilibrium magnetization, is time-independent. Thus, the spin pumping current has both a static dc-component and a time-dependent ac component. The ac-component vanishes due to dephasing of spins in a very short distance from the interface, while the dc-component propagates a longer distance (spin diffusion length). Only the dc-component will be considered in this thesis, which can be found by taking the time average of Eq. (2.43) over one period of oscillation:

$$j_s^{0,dc} \langle \hat{\mathbf{s}} \rangle = \frac{\hbar}{4\pi} Re(g^{\uparrow\downarrow}) \left(\langle \hat{\mathbf{m}}_A \times \dot{\hat{\mathbf{m}}}_A + \hat{\mathbf{m}}_B \times \dot{\hat{\mathbf{m}}}_B \rangle \right), \quad (2.44)$$

where $\langle \hat{\mathbf{s}} \rangle$ points in the z-direction.

Recent theoretical work on spin pumping in a ferrimagnet/normal metal-bilayer by Kamra and Belzig (Kamra and Belzig, 2017) suggests that the Eq. (2.44) is not the full expression for the spin pumping current injected into the NM-layer. In (Cheng et al., 2014), they assumed the sublattice magnetizations to be two independent variables. However, $\hat{\mathbf{m}}_A$ and $\hat{\mathbf{m}}_B$ are coupled by the exchange interaction and therefore cannot be treated as independent when considering the magnetization dynamics. Using a quantum mechanical approach, they find that the z-component of the spin current is on the form:

$$j_s^0 \langle \hat{\mathbf{s}} \rangle = \frac{\hbar}{4\pi} \left(\langle g_{AA} \hat{\mathbf{m}}_A \times \dot{\hat{\mathbf{m}}}_A + g_{BB} \hat{\mathbf{m}}_B \times \dot{\hat{\mathbf{m}}}_B + g_{AB} \hat{\mathbf{m}}_A \times \dot{\hat{\mathbf{m}}}_B + g_{BA} \hat{\mathbf{m}}_B \times \dot{\hat{\mathbf{m}}}_A \rangle \right), \quad (2.45)$$

where g_{ij} are the spin mixing conductances. All the conductances are real and the $\uparrow\downarrow$ notation has been omitted. A key finding in this paper is the significant contribution from cross-sublattice terms $(g_{AB} \hat{\mathbf{m}}_A \times \dot{\hat{\mathbf{m}}}_B + g_{BA} \hat{\mathbf{m}}_B \times \dot{\hat{\mathbf{m}}}_A)$, which previously has been assumed to be negligible. In the case of a compensated antiferromagnet they find that $g_{AA} = g_{BB}$ and $g_{AB} = g_{BA}$. Extending Eq. (2.45) to the full expression one obtains:

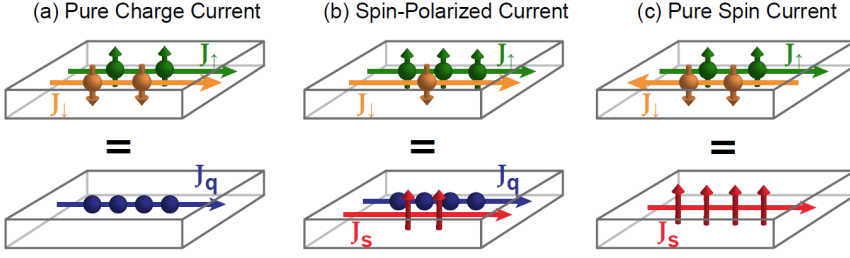


Figure 2.9: Schematic depiction of a pure charge current (a), with no net spin current, a spin polarized charge current (b), where electrons with opposite spins move in the same direction, and a pure spin current (c), where electrons with opposite spins propagate in the opposite direction, creating a net spin current and no charge current. The figure is adapted from (Muller, 2017)

$$j_s^0 \hat{s} = \frac{\hbar}{4\pi} \left(g_{AA} \hat{m}_A \times \dot{\hat{m}}_A + g_{BB} \hat{m}_B \times \dot{\hat{m}}_B + g_{AB} \hat{m}_A \times \dot{\hat{m}}_B + g_{BA} \hat{m}_B \times \dot{\hat{m}}_A \right), \quad (2.46)$$

The spin current propagates into the normal metal perpendicular to the interface due to spin diffusion, creating a pure spin current. A pure spin current can be explained by considering two channels of electrons traveling in the opposite direction. If the polarization of the electrons in the two channels are opposite, then there will be no net charge current, only a net current of spins (see Fig. 2.9).

2.4.2 Spin accumulation induced by spin pumping current

The spin current at the interface relaxes due to interaction with the nearby electrons. When the relaxation time of the spins in the normal metal is longer than the spin injection rate, a spin density, μ_N , is accumulated at the interface (Tserkovnyak et al., 2002a). The produced accumulation has to diffuse. Some of the spin density diffuses back into the magnet, called spin back-flow (Costache et al., 2008), reducing the total spin current. In Eq. (2.43), this can be taken into account by changing $g^{\uparrow\downarrow}$ to $g_{eff}^{\uparrow\downarrow}$ (Tserkovnyak et al., 2002b). In addition, the angular momentum of the magnetization is reduced by the spins exerting a spin-transfer-torque (STT) (Sankey et al., 2008) on the magnetization, which is the reciprocal effect of spin pumping. This is the mechanism behind the enhanced Gilbert damping observed in FM/NM-multilayer experiments (Tserkovnyak et al., 2002a; Urban et al., 2001). The other possible direction of diffusion is into the normal metal, driving the spin current in the NM-layer. In this direction, the spin diffusion is limited by momentum

scattering (leading to electrical resistance) and spin-flip scattering, by spin-orbit coupling or magnetic impurities, (leading to loss of spin angular momentum) causing the spin density to decay as it moves away from the interface. This creates a spin accumulation profile in the NM-layer.

An expression for the spin accumulation can be obtained by solving the spin diffusion equation describing its dissipative propagation in the NM-layer (Mosendz et al., 2010):

$$\frac{d\boldsymbol{\mu}_N}{dt} = D \frac{\partial^2 \boldsymbol{\mu}_N}{\partial x^2} - \frac{1}{\tau_{sf}} \boldsymbol{\mu}_N, \quad (2.47)$$

where τ_{sf} is the spin-flip time, x is the coordinate normal to the interface, and $D = \frac{v_F^2 \tau_{el}}{3}$ is the electron diffusion constant, with v_{el} as the electron momentum relaxation time Tserkovnyak et al. (2002b). The relaxation time can be understood as the time between successive interactions with electrons or impurities in the material. Assuming $\boldsymbol{\mu}_N \propto e^{mx+i\omega t}$, where ω is the angular frequency, Eq. (2.47) becomes:

$$i\omega \boldsymbol{\mu}_N = D \frac{\partial^2 \boldsymbol{\mu}_N}{\partial x^2} - \frac{1}{\tau_{sf}} \boldsymbol{\mu}_N. \quad (2.48)$$

For the bilayer structure, the boundary conditions are provided by the injected spin pumping current from the magnet. Assuming that the thickness of the nonmagnetic material is larger than the spin diffusion length, there is no spin current at the end of the metal and the spin current at the interface is the spin pumping current, j_s^0 , introduced above. Thus, the boundary conditions read (Mosendz et al., 2010):

$$j_s^0 \hat{s}(x=0) = -D \left. \frac{\partial \boldsymbol{\mu}_N}{\partial x} \right|_{x=0} \quad (2.49)$$

$$0 = \left. \frac{\partial \boldsymbol{\mu}_N}{\partial x} \right|_{x=t_N}, \quad (2.50)$$

where t_N is the thickness of the NM layer. Solving the equation provides the following expression:

$$\boldsymbol{\mu}_N(x) = j_s^0 \hat{s} \frac{\lambda_{sd}}{D} \frac{\cosh([x - t_N]/\lambda_{sd})}{\sinh t_N/\lambda_{sd}} \hat{x}, \quad (2.51)$$

where $\lambda_{sd} \approx \sqrt{D\tau_{sf}}$ (since $\omega \ll 1/\tau_{sf}$ as noted in the beginning of this subsection) is the spin-diffusion length. Eq. (2.51) displays the spin density profile as a function of distance, x , from the magnet/normal metal interface. It is easy to see that the equation describes a decay of spin density for increasing x .

The spin current density resulting from the spin diffusion can be expressed using Eq. (2.51). Analogous to an electrical current, the spin current is proportional to the rate of change of the spin accumulation density with respect to the distance from the interface:

$$\begin{aligned} \mathbf{j}_s(x) &= D \frac{\partial \mu_N}{\partial x} \\ &= j_s^0 \hat{\mathbf{s}} \frac{\sinh([x - t_N]/\lambda_{sd})}{\sinh(t_N/\lambda_{sd})} \hat{\mathbf{x}}. \end{aligned} \quad (2.52)$$

Since the spin pumping current is proportional to the spin pumping current, it contains both an ac- and a dc-component. The relevant component to the spin current for this thesis is the time-averaged spin current density $\langle \mathbf{j}_s \rangle$, polarized in the direction of the saturation magnetization:

$$\mathbf{j}_s^{dc}(x) = \langle j_s^{0,dc} \hat{\mathbf{s}} \rangle \frac{\sinh([x - t_N]/\lambda_{sd})}{\sinh(t_N/\lambda_{sd})} \hat{\mathbf{x}}. \quad (2.53)$$

As the spin density decays, naturally the spin pumping current decays as well. The scattering processes responsible for the decay also generates a measurable charge current. This is called the Inverse Spin Hall Effect (ISHE) (Saitoh and Miyajima, 2006), and gives the means to measure the spin current.

2.4.3 Electrical detection of spin currents: The Inverse Spin Hall effect

Analogous to the Hall effect from electrodynamics, the Inverse Spin Hall effect generates a charge current transverse to the direction of propagation of the electrons. Instead of an externally applied magnetic field acting with a force on the electrons forcing them to the boundaries of the metal, the scattering of the spin current electrons induces the electrical current. Due to spin-orbit coupling, electrons with equal spin polarization are scattered in the same direction. Since spins with opposite polarization travels in the opposite direction in a pure spin current, all the electrons will be scattered towards the same edge of the paramagnetic material, inducing a transverse electrical current (see Fig. 2.10). Electrical charge will then build up at the edge, creating an electrical field. By attaching electrodes to the edges, the voltage produced by the electrical field can be measured (Mosendz et al.,

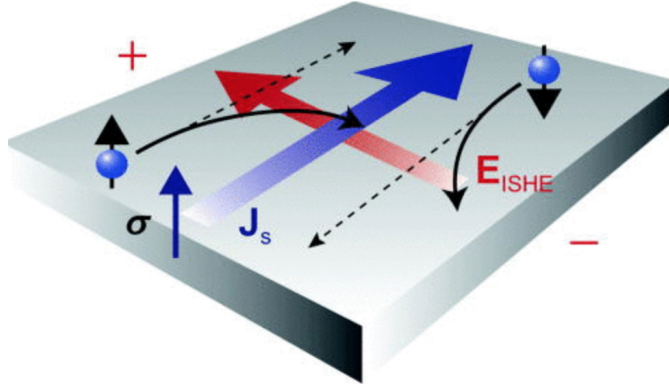


Figure 2.10: Schematic depiction of the Inverse Spin Hall effect. The pure spin current, J_s , with polarization, σ , pumped into the normal metal is scattered by electrons and impurities in the metal. Due to antisymmetric scattering of electrons with opposite spin polarization, the spin current electrons are bent towards one edge of the sample, inducing an electrical field E_{ISHE} . The electric potential due to the accumulation of charges is shown by the + and - signs at the edges. The figure is adapted from (Ando et al., 2011) and is slightly altered.

2010; Saitoh and Miyajima, 2006).

The reciprocal effect is called Spin Hall effect (SHE), where an electrical current is converted into a transverse spin current by the same scattering processes responsible for ISHE. Thus, harnessing both ISHE and SHE enables the conversion between spin currents and charge currents, which is paramount to combine spintronics with conventional electronics. Experiments on ISHE in a Pt-metal layer preformed by Saitoh et al. (Saitoh and Miyajima, 2006) demonstrated that a measurable charge current is induced at room temperature. Thus, SHE and ISHE are immediately adaptable to the metal-based spintronics used today.

The relation between the electrical current density, \mathbf{j}_c^{ISHE} , the spin current density, \mathbf{j}_s and the spin polarization, \hat{s} , is given by:

$$\mathbf{j}_c^{ISHE} = \frac{\gamma_H 2e}{\hbar} \mathbf{j}_s \times \hat{s}, \quad (2.54)$$

where γ_H is the Hall-angle (Dyakonov and Khaetskii, 2008) quantifying the efficiency of the spin-charge conversion. Since the spin polarization of the time-dependent and static component of the spin pumping current are different, an ac and dc charge current is induced. Thus, it is possible to measure the two spin currents by placing the electrodes between different edges of the nonmagnet. We will only consider the dc-component:

$$\mathbf{j}_{c,dc}^{ISHE} = \frac{\gamma_H 2e}{\hbar} \mathbf{j}_s^{dc} \times \langle \hat{\mathbf{s}} \rangle, \quad (2.55)$$

where $\langle \hat{\mathbf{s}} \rangle$ points in the equilibrium magnetization direction.

Due to the electric field, some electrons will be attracted to the opposite edge, contributing to the charge current. Using ohms law, $\mathbf{j} = \sigma \mathbf{E}$, the total charge current can be expressed as:

$$\mathbf{j}_{c,dc} = \mathbf{j}_{c,dc}^{ISHE}(x) + \sigma \mathbf{E}, \quad (2.56)$$

where σ is the electrical conductivity. The NM-layer constitutes an open circuit. From elementary electrostatics, no dc-current can flow in an open circuit. This condition can be described as:

$$\int_{-t_M}^{t_N} \mathbf{j}_{c,dc} dx = 0, \quad (2.57)$$

where t_M is the thickness of the magnetic layer. Since there is no charge current in the magnetic material, the electrical field can be readily calculated by substitution of Eq. (2.56) in Eq. (2.57):

$$\mathbf{E} = \frac{\gamma_H (2e/\hbar) \langle j_s^0 \rangle \lambda_{sd}}{\sigma_N t_N + \sigma_M t_M} \tanh \frac{t_N}{2\lambda_{sd}} [\hat{\mathbf{x}} \times \langle \hat{\mathbf{s}} \rangle]. \quad (2.58)$$

Here σ_N and σ_M constitutes the charge conductivities in the normal metal and magnet, respectively. If the length of the metal is much greater than the thickness, the electrical field is constant. From elementary electrostatics, we then have $V = LE$, and the expressions for the measurable voltages become:

$$V_{x,y,z} = \frac{\gamma_H (2e/\hbar) \langle j_s^0 \rangle \lambda_{sd} L}{\sigma_N t_N + \sigma_M t_M} \tanh \frac{t_N}{2\lambda_{sd}} [\hat{\mathbf{x}} \times \langle \hat{\mathbf{s}} \rangle]_{x,y,z}, \quad (2.59)$$

where the subscripts x, y, z denote the direction in which the voltages are measured. The voltage is only generated in the distance of the spin diffusion length since the spin current is completely relaxed beyond this distance. The proportionality of the with the length, L , makes it possible to obtain measurable voltage values even for low spin-charge conversion efficiency, γ_H , by increasing the sample length.

Results and discussion

In the previous chapter we have seen how a dynamic magnet, excited by an oscillating applied field, pumps an experimentally detectable spin current into an adjacent metal. To investigate the effect of the cross-sublattice terms on the total dc spin pumping current and if it can be measured as a voltage signal, we consider an the antiferromagnetic/normal metal bilayer introduced in Sec. 2.4, for three different antiferromagnetic systems. Two systems in a collinear ground state and one in a non-collinear ground state are treated. Each of the three bilayers are considered separately in their own section and are presented in increasing order of complexity. The sections are divided as follows. First, the solution to the LLG-equations of motion for the system is presented and discussed, followed by a general analytic expression for the dc spin pumping current and ISHE-voltage for the corresponding ground state of the antiferromagnet. The solution to the equations of motion is then used to calculate the spin current numerically as a function of the frequency of oscillations of the applied. To gain insight into both the magnetization and spin dynamics, the spin current is calculated for different values of the static part of the oscillating field and the cross-sublattice spin-mixing conductance.

For two of these systems, the solution to the LLG-equations require the inverse of a 4x4 susceptibility tensor. Due to the complexity of the tensors, the analytic solution is unattainable. We must therefore resort to numerical calculations. For this thesis, the MatLab language was used to write programs calculating and plotting the dc spin pumping current as a function of the frequency, ω , of the applied field. The numerics behind the results are elucidated in the appendix.

3.1 Easy axis antiferromagnet in collinear ground state

3.1.1 Magnetization dynamics

Starting with the simplest possible antiferromagnetic system. Consider an antiferromagnet with easy axis magnetocrystalline anisotropy along the z-direction parametrized by the parameters $K_A = K_B = K_z > 0$. The free energy of the system is then exchange dominated and the magnet is in a collinear ground state with antiparallel alignment of the sublattice magnetizations along the z-axis. Assume that the antiferromagnet is symmetric, such that we have uniform magnetization $\mathbf{M}_A = -\mathbf{M}_B$ and $\gamma_A = \gamma_B = \gamma$. We allow for antisymmetry in the Gilbert damping however, since the symmetry may be broken at the interface, by for example spin mixing conductances (Kamra et al., 2018), leading to $\alpha_{AA} \neq \alpha_{BB}$.

Consider influencing the magnet by applying an oscillating, external magnetic field along the easy axis. We assume that the time-variation of the field is small, such that the applied field and the magnetization can be considered as a sum of steady and alternating parts, as in Eqs. (2.38) and (2.39). For such small deviations from equilibrium, the \hat{z} -component of the magnetization is unchanged to first-order in small quantities so that $|\mathbf{M}_A| = |\mathbf{M}_B| \approx M_0$. Further assume that the field strength is below the spin flop field. The ground state configuration then remains unchanged and the oscillations of the magnetization is in the xy-plane. Adding the energy contributions, the free energy of the system is expressed as:

$$F[\mathbf{M}_A, \mathbf{M}_B] = \int_{dV} d^3r \left(-\mu_0 \mathbf{H} \cdot (\mathbf{M}_A + \mathbf{M}_B) - K_z M_{Az}^2 - K_z M_{Bz}^2 + J \mathbf{M}_A \cdot \mathbf{M}_B \right), \quad (3.1)$$

where $\mathbf{H} = H_0 \hat{z} + h_x \hat{x} + h_y \hat{y}$, $\mathbf{M}_A = M_0 \hat{z} + m_{A_x} \hat{x} + m_{A_y} \hat{y}$ and $\mathbf{M}_B = -M_0 \hat{z} + m_{B_x} \hat{x} + m_{B_y} \hat{y}$, with $|h_{x,y}| \ll H_0$ and $|m_{A_{x,y}, B_{x,y}}| \ll M_0$. Note, that $J > 0$ since the negative sign of the exchange intergal is already incorporated through the positive sign for the exchange energy in Eq. (3.1). By the relation Eq. (2.28), we find the effective fields exerting a torque on the sublattice magnetizations to be:

$$\mathbf{B}_A = \mu_0 \mathbf{H} + 2K_z M_0 \hat{z} - J \mathbf{M}_B \quad (3.2)$$

$$\mathbf{B}_B = \mu_0 \mathbf{H} - 2K_z M_0 \hat{z} - J \mathbf{M}_A. \quad (3.3)$$

Since the vector length of the magnetization is approximatly constant, the LLG-equations

can be employed to calculate the dynamic motion of the antiferromagnetic magnetizations. The spin pumping current expression is written in terms of the unit vector magnetizations. We therefore use the LLG-equations in unit vector form:

$$\begin{aligned}\dot{\hat{\mathbf{m}}}_A &= -\gamma\hat{\mathbf{m}}_A \times \mathbf{B}_A + \alpha_{AA} \left(\hat{\mathbf{m}}_A \times \dot{\hat{\mathbf{m}}}_A \right) + \alpha_{AB} \left(\hat{\mathbf{m}}_A \times \dot{\hat{\mathbf{m}}}_B \right) \\ \dot{\hat{\mathbf{m}}}_B &= -\gamma\hat{\mathbf{m}}_B \times \mathbf{B}_B + \alpha_{BB} \left(\hat{\mathbf{m}}_B \times \dot{\hat{\mathbf{m}}}_B \right) + \alpha_{BA} \left(\hat{\mathbf{m}}_B \times \dot{\hat{\mathbf{m}}}_A \right),\end{aligned}$$

where $\hat{\mathbf{m}}_{A,B} = (m_{A_x,B_x}/M_0)\hat{\mathbf{x}} + (m_{A_y,B_y}/M_0)\hat{\mathbf{y}} \pm \hat{\mathbf{z}}$. Due to the exchange coupling and cross-sublattice damping, the motion of the sublattice magnetizations are dependent on each other. The equations are therefore coupled in the sublattice magnetizations.

Consider harmonic time dependence of the applied field. As the LLG-equations are linear, it is reasonable to assume harmonic behaviour of the magnetization components as well. Employing the method of complex amplitudes, we introduce $\hat{\mathbf{m}}_{A,B} = \hat{\mathbf{m}}_{A,B} e^{i\omega t}$ and $\mathbf{h} = \mathbf{h} e^{i\omega t}$. The complex variables $\hat{\mathbf{m}}_{A,B}$ and \mathbf{h} are the complex amplitudes of the real time-varying fields. Projecting the amplitudes onto a Cartesian coordinate system, substituting the Eqs. (3.2) and (3.3) in the equations of motion, and switching to a circular basis via $\hat{m}_{A\pm,B\pm} = \hat{m}_{A_x,B_x} \pm i\hat{m}_{A_y,B_y}$ etc., the equations above become:

$$\pm\omega\hat{m}_{A\pm} = -\gamma\mu_0\mathbf{h}_{\pm} + (\Omega_A + i\alpha_{AA}\omega)\hat{m}_{A\pm} + (\gamma JM_0 + i\alpha_{AB}\omega)\hat{m}_{B\pm} \quad (3.4)$$

$$\mp\omega\hat{m}_{B\pm} = -\gamma\mu_0\mathbf{h}_{\pm} + (\Omega_B + i\alpha_{BB}\omega)\hat{m}_{B\pm} + (\gamma JM_0 + i\alpha_{BA}\omega)\hat{m}_{A\pm}, \quad (3.5)$$

where we have defined $\hat{m}_{A_x} = m_{A_x}/M_0$ etc. as the unit vector components of the magnetization. To get to Eqs. (3.4) and (3.5), the equations have been linearized in the small field values $\hat{\mathbf{m}}_{A,B}$ and \mathbf{h} . This is valid when $H_0 \gg |\mathbf{h}|$ and $M_0 \gg |\mathbf{m}_{A,B}|$. The first term in the equations originates from the torque on the sublattice magnetizations from the time-varying components of the applied field. The second term corresponds to the torque from the intra-sublattice damping and the static components in $\mathbf{B}_{A,B}$. The remaining term is the torque from the time-varying components of the magnetization from the opposite sublattice.

Rearranging terms, the equations can be written in matrix form as follows:

$$\begin{bmatrix} \gamma\mu_0\mathbf{h}_{\pm} \\ \gamma\mu_0\mathbf{h}_{\pm} \end{bmatrix} = \begin{bmatrix} -(\pm\omega - \Omega_A - i\alpha_{AA}\omega) & \gamma JM_0 + i\alpha_{AB}\omega \\ \gamma JM_0 + i\alpha_{BA}\omega & \pm\omega + \Omega_B + i\alpha_{BB}\omega \end{bmatrix} \begin{bmatrix} \hat{m}_{A\pm} \\ \hat{m}_{B\pm} \end{bmatrix}, \quad (3.6)$$

where $\Omega_A = \gamma(\mu_0 H_0 + 2K_z M_0 + J M_0)$ and $\Omega_B = \gamma(2K_z M_0 + J M_0 - \mu_0 H_0)$. This matrix must be inverted to obtain an expression for the magnetization amplitudes. Inverting gives:

$$\begin{bmatrix} \hat{m}_{A\pm} \\ \hat{m}_{B\pm} \end{bmatrix} = \frac{1}{D} \begin{bmatrix} \pm\omega + \Omega_B + i\alpha_{BB}\omega & -(\gamma J M_0 + i\alpha_{AB}\omega) \\ -(\gamma J M_0 + i\alpha_{AB}\omega) & -(\pm\omega - \Omega_A - i\alpha_{AA}\omega) \end{bmatrix} \begin{bmatrix} \gamma\mu_0 \hbar \pm \\ \gamma\mu_0 \hbar \pm \end{bmatrix}, \quad (3.7)$$

with

$$D = -(\pm\omega - \Omega_A - i\alpha_{AA}\omega)(\pm\omega + \Omega_B + i\alpha_{BB}\omega) - (\gamma J M_0 + i\alpha_{AB}\omega)^2, \quad (3.8)$$

which is the determinant of Eq. (3.6) and we have used that $\alpha_{AB} = \alpha_{BA}$ for all anti-ferromagnets (Kamra et al., 2018). Thus, we have obtained a solution written in terms of two decoupled rotational modes, the + and - polarized modes of the magnetization. Employing a plus (minus) polarized external field, excites the plus (minus) mode of the magnetization. Comparing Eq. (3.7) with Eq. (2.42), the 2x2 matrix times the prefactor $1/D$ is the dynamic susceptibility tensor of the magnet.

By considering the motion at resonance, we obtain valuable information about the behaviour of the magnetization for the two modes. At resonance, the time-dependent magnetization components have a peak in amplitude and will therefore create a stronger spin current than for other frequencies. Solving the equation $D = 0$ for ω for both signs gives $\omega_{\pm} = \omega_{r\pm} + i\omega_{i\pm}$, where $\omega_{r\pm}$ are the resonance frequencies and $\omega_{i\pm}$ are called the decay rates. The resonance frequencies and decay rates are calculated to:

$$\omega_{\pm} \approx \frac{\pm(\Omega_A - \Omega_B) + \sqrt{(\Omega_A + \Omega_B)^2 - 4(\gamma J M_0)^2}}{2} \quad (3.9)$$

$$= \pm\gamma\mu_0 H_0 + 2\gamma M_0 \sqrt{(J + K_z)K_z} \quad (3.10)$$

and

$$\frac{\omega_{i\pm}}{\omega_{r\pm}} = \frac{\pm\omega_{r\pm}(\alpha_{AA} - \alpha_{BB}) + \alpha_{AA}\Omega_B + \alpha_{BB}\Omega_A - 2J|\gamma_B|M_{A0}\alpha_{AB}}{\omega_{r+} + \omega_{r-}}, \quad (3.11)$$

to zeroth and first order in the Gilbert damping parameters, respectively, when the damping is small. Thus, the two modes have different resonance frequencies. Here, the positive solutions have been chosen for the equations of the resonance frequencies. The positive and negative solutions are equal in magnitude and represent the same modes physically.

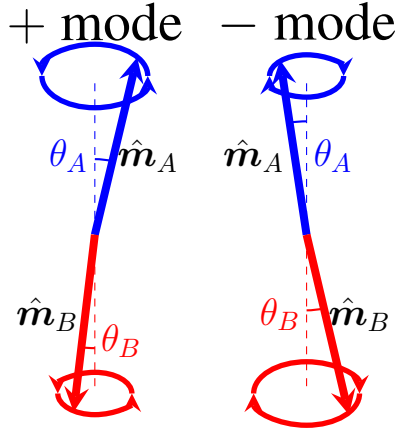


Figure 3.1: Schematic depiction of the two eigenmodes of the antiferromagnetic magnetizations. The chiralities and cone angle ratios are opposite for the two modes. The plus mode constitutes counter clockwise rotation, while the minus mode demonstrates clock wise rotation. The angles of the two sublattice magnetizations have been exaggerated for clarity.

Substituting $\omega = \omega_+ = \omega_{r_+} + i\omega_{i_+}$ in D for the lower sign, we obtain $D \neq 0$. The system therefore only has the trivial solution $m_{A_-} = m_{B_-} = 0$, which means $m_{A_x} = im_{A_y}$ and $m_{B_x} = im_{B_y}$. This corresponds to circular precession of the magnetization with right hand rotation (right hand polarized mode). Similarly, we have $m_{A_+} = m_{B_+} = 0$ for $\omega = \omega_{r_-} + i\omega_{i_-}$. In this case we have $m_{A_x} = -im_{A_y}$ and $m_{B_x} = -im_{B_y}$, resulting in circular precession with left hand rotation (left hand polarized mode). A depiction of the two modes is given in Fig. 3.1. Note, that in addition to the opposite chiralities of the two modes, the ratio of the cone angles θ_A and θ_B are opposite as well. Comparing Ω_A and Ω_B , one can see that the breaking of the degeneracy of the modes is due to the magnetic field applied along the easy axis (consistent with the findings in (Kamra et al., 2017)) and the difference in intra-sublattice damping. When applying the external field, the Zeeman energy for the magnetization is increased (decreased) in the direction antiparallel (parallel) to the field. Thus, the total energy of the system is different when looking in the direction parallel and antiparallel to the easy axis, breaking the rotational symmetry. This results in a gapped excitation spectrum and a lifting of the degeneracy of the modes. A discrepancy in the intra-sublattice damping leads to energy and angular momentum differences between the two sublattice magnetizations, increasing the disparity in the subtended cone angle.

An intuitive picture explaining the of the behaviour of the two modes is as follows: In the plus mode, \hat{m}_A is "driving" the motion, while \hat{m}_B follows the exchange field (molecular field) of \hat{m}_A . Increasing H_0 , raises the effective field B_A , resulting in a higher resonance frequency of \hat{m}_A and therefore the entire system. For the minus mode, the reverse is

true. The precession direction of both magnetisations is clockwise, with a phase difference π due to the exchange interaction forcing the magnetization vectors to be antiparallel.

These results are in excellent agreement with the results found by Kittel (Keffer and Kittel, 1952) and Gurevich (Gurevich and Melkov, 1996) on antiferromagnetic resonance for $\alpha_{AA} = \alpha_{BB} = \alpha$ and $\alpha_{AB} = 0$. Furthermore, comparing Eqs. (3.7), (3.10) and (3.11) to the results obtained in (Kamra et al., 2018) for general two-sublattice magnets, their expressions concur with what is presented in this thesis for $\gamma_A = \gamma_B = \gamma$, $K_A = K_B = K_z$ and $M_{A0} = M_{B0} = M_0$.

3.1.2 Dc spin pumping current density and ISHE-voltage

Analytic results

Now that the dynamic motion has been established, dc spin pumping current density produced by the magnet and the induced measurable voltage can be calculated. Note that the analytic spin current expressions calculated, does not assume any free energy of the magnet, and is thus general for this type of configuration. As discussed in Sec. 2.4, the dc spin current is found by taking the time-average over period of oscillation of Eq. (2.46):

$$j_s^0 \langle \hat{s} \rangle = \frac{\hbar}{4\pi} \left(\langle g_{AA} \hat{m}_A \times \dot{\hat{m}}_A + g_{BB} \hat{m}_B \times \dot{\hat{m}}_B + g_{AB} \hat{m}_A \times \dot{\hat{m}}_B + g_{BA} \hat{m}_B \times \dot{\hat{m}}_A \rangle \right). \quad (3.12)$$

The total expression is linear, so we can take the time-average of each term independently.

Let's start by considering the intra-sublattice contributions to the spin current. Both magnetizations have a static component in the \hat{z} -direction. The x- and y-components of the cross-product $\hat{m}_{A,B} \times \dot{\hat{m}}_{A,B}$ are thus to first order in the time-varying magnetization components and vanish upon time averaging. The contributions to the spin current therefore only have a component in the z-direction given by:

$$j_{s,intra}^{0,dc} = \frac{\hbar}{4\pi} \langle \hat{s} \rangle = \left(g_{AA} \langle \hat{m}_{Ax} \dot{\hat{m}}_{Ay} - \hat{m}_{Ay} \dot{\hat{m}}_{Ax} \rangle + g_{BB} \langle \hat{m}_{Bx} \dot{\hat{m}}_{By} - \hat{m}_{By} \dot{\hat{m}}_{Bx} \rangle \right) \hat{z}. \quad (3.13)$$

This is consistent with the results in (Cheng et al., 2014; Johansen and Brataas, 2017) for $g_{AA} = g_{BB}$. The solution to the LLG-equations is complex. It is therefore convenient to express the spin current in the complex amplitudes of the magnetization components. The real components can be written in terms of their complex amplitudes as follows:

$$\begin{aligned}\hat{m}_{A_x, B_x} &= \frac{1}{2} \left(\hat{m}_{A_x, B_x} e^{i\omega t} + \hat{m}_{A_x, B_x}^* e^{-i\omega t} \right) \\ \hat{m}_{A_y, B_y} &= \frac{1}{2} \left(\hat{m}_{A_y, B_y} e^{i\omega t} + \hat{m}_{A_y, B_y}^* e^{-i\omega t} \right)\end{aligned}$$

where * denotes the complex conjugate. In order for the results in Eq. (3.7) to be used, we must switch to the circular basis employed earlier. Substituting the complex representation in Eq. (3.13), taking the time-average and transforming to circular variables, we obtain:

$$j_{s, intra}^{0, dc} \langle \hat{\mathbf{s}} \rangle = \frac{\hbar\omega}{16\pi} \left[g_{AA} (|\hat{m}_{A+}|^2 - |\hat{m}_{A-}|^2) + g_{BB} (|\hat{m}_{B+}|^2 - |\hat{m}_{B-}|^2) \right] \hat{\mathbf{z}}, \quad (3.14)$$

where the relations $A^*B - AB^* = 2iIm(A^*B)$ and $A^*B + AB^* = 2Re(A^*B)$ have been applied, and $|\hat{m}_{\pm}|^2 = \hat{m}_{\pm} \hat{m}_{\pm}^*$. Although the spin current is expressed in the complex amplitudes of the magnetization vectors, the absolute square of the amplitudes make the expression real, which is required for a physically measurable quantity. From Eq. (3.14) it is easy to see that the plus and minus polarized modes give oppositely polarized spin currents. Thus, we can choose which way the charge current flows in the normal metal by influencing the magnet with a plus or minus polarized applied field.

Similarly to the intra-sublattice terms, the cross-products in the cross-sublattice terms only have a nonzero component in the $\hat{\mathbf{z}}$ -direction upon time averaging. Using that $g_{AB} = g_{BA}$ for antiferromagnets, we have:

$$j_{s, cross}^{0, dc} \langle \hat{\mathbf{s}} \rangle = \frac{\hbar g_{AB}}{4\pi} \left(\langle \hat{m}_{A_x} \dot{\hat{m}}_{B_y} - \hat{m}_{A_y} \dot{\hat{m}}_{B_x} \rangle + \langle \hat{m}_{B_x} \dot{\hat{m}}_{A_y} - \hat{m}_{B_y} \dot{\hat{m}}_{A_x} \rangle \right) \hat{\mathbf{z}}. \quad (3.15)$$

Following the same procedure as for the intra-sublattice terms and adding the obtained expression to Eq. (3.14), the total dc spin pumping current reads:

$$\begin{aligned}j_s^{0, dc} \langle \hat{\mathbf{s}} \rangle &= \frac{\hbar\omega}{16\pi} \left(g_{AA} (|\hat{m}_{A+}|^2 - |\hat{m}_{A-}|^2) + g_{BB} (|\hat{m}_{B+}|^2 - |\hat{m}_{B-}|^2) + \right. \\ &\quad \left. 2g_{AB} Re(\hat{m}_{A+}^* \hat{m}_{B+} - \hat{m}_{A-}^* \hat{m}_{B-}) \right) \hat{\mathbf{z}}.\end{aligned} \quad (3.16)$$

It is clear that the cross-sublattice contributions are real and non-zero, consistent with (Kamra and Belzig, 2017). Thus, they will ultimately have an effect on the produced signal

from the dynamic magnet. However, since the spin current only has a component polarized in a single direction, the cross-terms cannot be isolated experimentally. It is therefore not possible to measure the effect of these terms on the spin current for an antiferromagnet in a collinear ground state. Furthermore, we observe that the two modes are still uncoupled in the full expression, so the spin current for the two modes is polarized in the positive and negative \hat{z} -direction, respectively. By exciting only the plus (minus) mode, the spin current will thus have a positive (negative) peak at the resonance frequency of the mode. Substituting Eq. (3.16) in the voltage expression Eq. (2.59), we have:

$$V_y = -\frac{\gamma_H e \lambda_{sd} L \omega}{8\pi(\sigma_N t_N + \sigma_F t_F)} \tanh \frac{t_N}{2\lambda_{sd}} \left[g_{AA}(|\hat{m}_{A+}|^2 - |\hat{m}_{A-}|^2) + g_{BB}(|\hat{m}_{B+}|^2 - |\hat{m}_{B-}|^2) \right. \\ \left. 2g_{AB} \text{Re}(\hat{m}_{A+}^* \hat{m}_{B+} - \hat{m}_{A-}^* \hat{m}_{B-}) \right]. \quad (3.17)$$

Due to the polarization parallel (antiparallel) to the z -direction, the electrical signal is only produced across the edges in the y -direction in the normal metal.

Numerical results

In order to gain insight into the magnetization dynamics and the effect of the cross-sublattice spin current, the dc spin pumping current has been plotted for different values of the applied field and the spin mixing conductances. To simulate a real AF|N-layer system reasonable parameter values must be chosen. Remember from 2.4.1 that spin transfer in AF|NM is as efficient as in FM|NM. Thus, the spin mixing conductances are of the same order of magnitude in both types of layers. The intra-sublattice spin mixing conductances are chosen to be $g_{AA} = g_{BB} = 2 \cdot 10^{19} \text{ m}^{-2}$, close to the spin mixing conductance in Pt (Mosendz et al., 2010). The other parameter values are: $\gamma = 10^{11}$, $J = 10^{-4}$, $K_z = K_x = 10^{-7}$, $M_0 = 10^5$ and $\alpha_{AA} = \alpha_{BB} = 0.01$ in SI units, and have been chosen to represent the typical order of magnitude without pertaining to a specific material. For the values of the ac-field amplitudes, $\hat{h}_{\pm} = 0.005/\mu_0$ are employed. These values are used for all systems considered.

In Fig. 3.2, the dc spin current is plotted as a function of the frequency ω , of the ac-field, for different values of H_0 , for the plus mode of the magnetization. For simplicity, the cross-sublattice spin mixing conductance and damping parameters are chosen to be zero. Observing the curves, the spin current displays a positive peak for one frequency value corresponding to the resonance frequency of the plus mode of the magnetization.

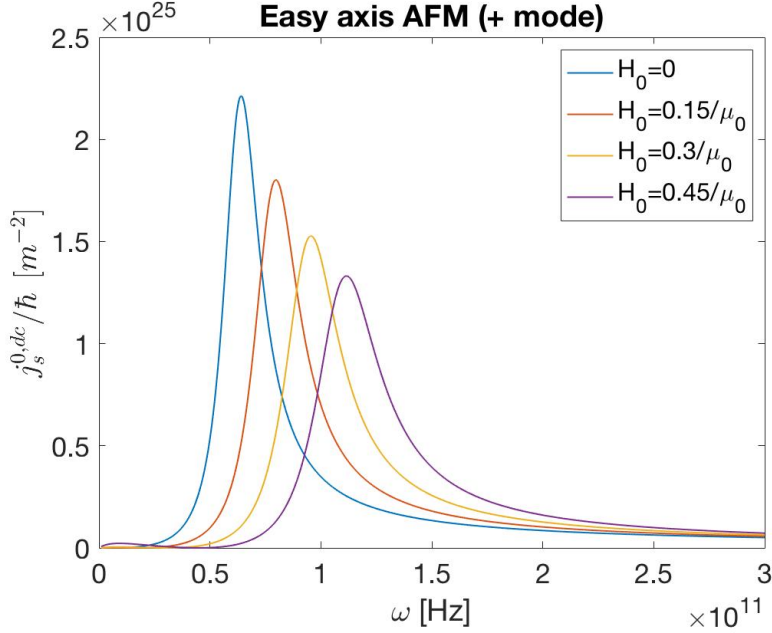


Figure 3.2: The dc spin pumping current, for the plus polarized mode of the easy axis antiferromagnet in collinear ground state, as a function of frequency, ω , of the ac-field. The current is plotted for four different values of the magnitude of the steady part of the applied field.

This is expected considering Eq. (3.16) and the analysis of the magnetization dynamics above. Comparing this behaviour to the results in (Cheng et al., 2014) and (Johansen et al., 2018) (since the voltage is proportional to $j_s^{0,dc}$) for the right circular polarized mode, one finds that they are in excellent agreement. From Eq. (3.10), we see that the frequency increases for increasing H_0 for the plus mode. This explains why the peak moves to the right for larger field strength. Two peculiar features of the results are the decrease in amplitude and the slight broadening of the peaks for stronger applied field. This can be attributed to the increase in the decay rate of the mode for increasing resonance frequency, since $\omega_{i\pm} \propto \omega_{r\pm}$ (see Eqs. (3.10) and (3.11)). The larger the decay rate, the more damped the motion of the magnetizations become, leading to smaller amplitude of the magnetization components and thus a smaller spin current. Increasing decay rate also leads to a broadening of the peak.

In Fig. 3.3 the minus mode of the magnetization is excited. We immediately observe that the spin current is negative and that the peaks occur for different frequencies, consistent with the previous discussions above and the results in (Cheng et al., 2014). However, there is a discrepancy in the frequency value of the peak in their paper and this thesis. They

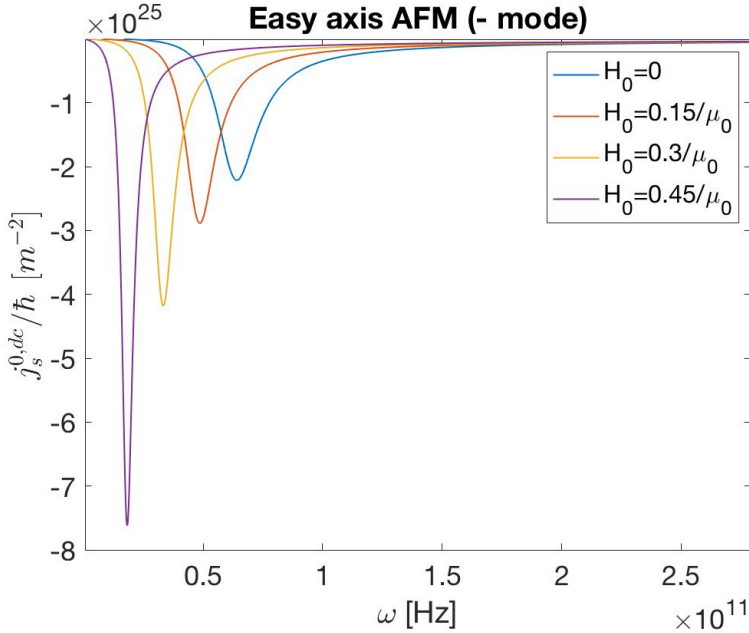


Figure 3.3: The dc spin pumping current, for the minus polarized mode of the easy axis antiferromagnet in collinear ground state, as a function of frequency, ω , of the applied field. The current is plotted for four different values of the magnitude of the steady part of the applied field.

plotted the spin current for $H_0 = 0$ and the peak occurs at the frequency $\omega_- = -\omega_+$, while the peak in Fig. 3.3 occurs at $\omega_- = \omega_+$ for the same field strength. In contrast to the results above, the amplitude increases, while width of the peak decreases for increasing H_0 . This can be explained in a similar fashion as before by considering Eqs. (3.10) and (3.11) for the minus sign. Larger fields give smaller resonance frequencies of the mode, and therefore larger spin currents. Thus, to produce the largest spin current, we should excite the minus mode of the antiferromagnet with a large, oscillating field with left circular polarization. A distinct feature compared to the oppositely polarized current, is the large increase in amplitude from $H_0 = 0.3/\mu_0$ and $H_0 = 0.45/\mu_0$. This can again be attributed to the decrease in decay rate.

The dc spin current is plotted for linearly polarized applied field, i.e equal amounts of right, h_+ , and left, h_- circular polarized field, in Fig. 3.4. This excites both the plus and minus mode of the magnetization at the same time, resulting in linearly polarized oscillation for ω far from ω_{\pm} . For ω close to ω_+ (ω_-), the plus (minus) mode dominates and the magnetization exhibits right (left) circular rotation. The spin current exhibits two peaks at two distinct frequencies, which is expected considering the modes

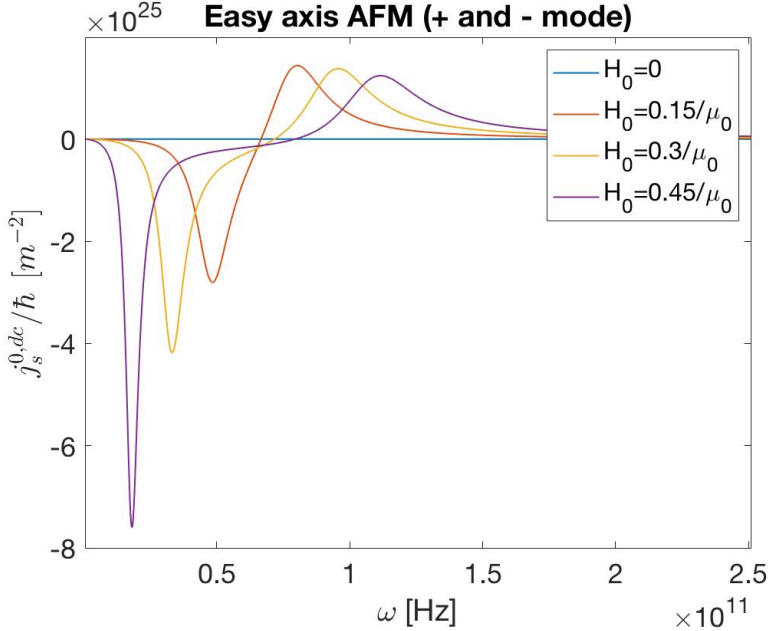


Figure 3.4: The dc spin pumping current, for the easy axis AFM excited by a linear polarized applied field, as a function of frequency, ω . The current is plotted for four different values of the magnitude of the steady part of the applied field.

being uncoupled in Eq. (3.16). Comparing the peaks, it is evident that the positive and negative peaks exhibit the same behaviour as discussed for the two modes excited separately. This is reasonable since the resonance frequencies of the modes are far enough apart, such that one dominates the other at ω_{\pm} . However, for $H_0 = 0$, the resonance frequencies of the modes are equal, resulting in no spin current since the contribution from the two modes cancels. The more H_0 increases, the greater the difference in resonance frequency of the modes, giving larger gaps between the peaks.

As shown by Kamra and Belzig (Kamra and Belzig, 2017), the spin mixing conductances are directly related to the damping parameters, thus α_{AB} cannot be zero when investigating the effect of cross-sublattice spin pumping. We therefore arbitrarily set $\alpha_{AB} = \alpha_{BA} = 0.001$. Keeping the field strength constant at $H_0 = 0.3/\mu_0$ and plotting the spin current for linear polarized applied field, we obtain the following results in Fig. 3.5. Note, that all other parameters are as before. The figure displays the spin current as a function of ω for four different values of g_{AB} . It is clear that the cross-sublattice spin current contributions have a significant effect on the total spin pumping current. As seen from the figure, the spin current is reduced by increasing the cross-sublattice spin

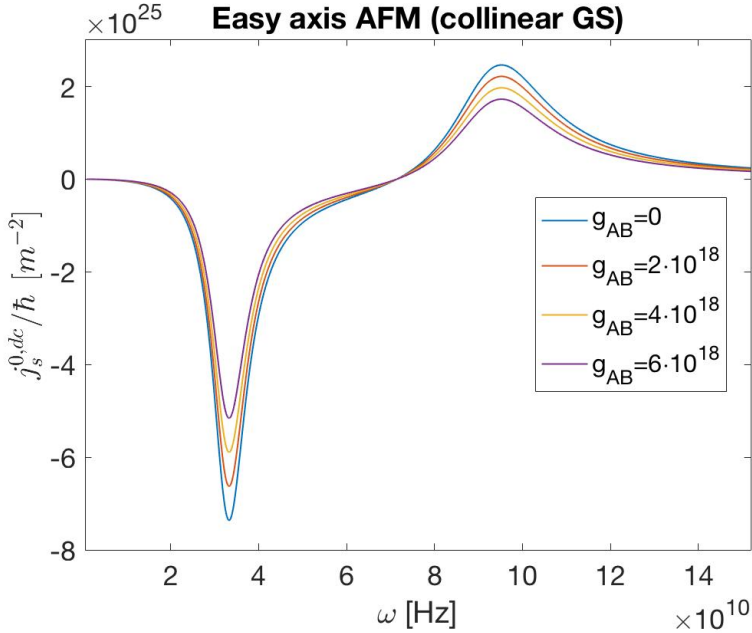


Figure 3.5: The dc spin pumping current, for the easy axis AFM excited by a linear polarized applied field, as a function of frequency, ω . The current is plotted for four different values of the cross-sublattice spin mixing conductance.

mixing conductance. This is because the sublattice magnetizations curtail the spin current pumped by the other. The effect can only be explained quantum mechanically and is therefore beyond the scope of this thesis, however the reader is referred to the following papers: (Kamra and Belzig, 2017) on spin pumping and spin shot noise in ferrimagnets, and (Liu et al., 2017) on mode-dependent damping in metallic antiferromagnets due to inter-sublattice spin pumping.

3.2 Biaxial antiferromagnet in collinear ground state

3.2.1 Magnetization dynamics

Now, consider the antiferromagnet to have a hard axis along the x-direction in addition to the easy axis. The free energy then increases due to the spin-orbit coupling. Thus, it is energetically unfavorable for the magnetization to have a component in this direction. This energy term does not affect the collinear ground state configuration of the AFM, since the x-component of the magnetization is zero in equilibrium. Applying the same oscillating

field as before, the free energy of the system reads:

$$F[\mathbf{M}_A, \mathbf{M}_B] = \int_{dV} d^3r \left(-\mu_0 \mathbf{H}(\mathbf{M}_A + \mathbf{M}_B) - K_z M_{Az}^2 - K_z M_{Bz}^2 + J \mathbf{M}_A \cdot \mathbf{M}_B + K_x M_{Ax}^2 + K_x M_{Bx}^2 \right), \quad (3.18)$$

where the hard axis anisotropy is parametrized by $K_x > 0$. The new effective fields acting with a torque on the sublattice magnetizations are:

$$\mathbf{B}_A = \mu_0 \mathbf{H} + 2K_z M_0 \hat{z} - J \mathbf{M}_B + 2K_x m_{A_x} \hat{x} \quad (3.19)$$

$$\mathbf{B}_B = \mu_0 \mathbf{H} - 2K_z M_0 \hat{z} - J \mathbf{M}_A + 2K_x m_{B_x} \hat{x}. \quad (3.20)$$

Similarly to the easy axis anisotropy parameter, the hard axis anisotropy parameter is equal for both sublattices due to the assumed symmetry of the antiferromagnet. The only difference from the previous case is the addition of a new effective field experienced by the magnetization. We therefore perform the same steps as in the previous case, yielding the following form of the unit vector LLG-equations:

$$\pm \omega \hat{m}_{A\pm} = -\gamma \mu_0 \hat{h}_{\pm} + (\Omega_A + i\alpha_{AA}\omega) \hat{m}_{A\pm} + (\gamma J M_0 + i\alpha_{AB}\omega) \hat{m}_{B\pm} + \gamma K_x M_0 (\hat{m}_{A+} + \hat{m}_{A-}) \quad (3.21)$$

$$\mp \omega \hat{m}_{B\pm} = -\gamma \mu_0 \hat{h}_{\pm} + (\Omega_B + i\alpha_{BB}\omega) \hat{m}_{B\pm} + (\gamma J M_0 + i\alpha_{BA}\omega) \hat{m}_{A\pm} + \gamma K_x M_0 (\hat{m}_{B+} + \hat{m}_{B-}). \quad (3.22)$$

Solving for the magnetization amplitudes, the solution to the equations can be written on the form:

$$\tilde{m} = (P_0 + P_H + R)^{-1} \tilde{h}, \quad (3.23)$$

with

$$\tilde{m} = \begin{bmatrix} m_{A+} \\ m_{B+} \\ m_{A-} \\ m_{B-} \end{bmatrix}, \quad \tilde{h} = \begin{bmatrix} \gamma\mu_0 h_+ \\ \gamma\mu_0 h_+ \\ \gamma\mu_0 h_- \\ \gamma\mu_0 h_- \end{bmatrix}$$

$$P_0 = \begin{bmatrix} -(\omega - \Omega_A) & \gamma JM_0 & 0 & 0 \\ \gamma JM_0 & (\omega + \Omega_B) & 0 & 0 \\ 0 & 0 & -(-\omega - \Omega_A) & \gamma JM_0 \\ 0 & 0 & \gamma JM_0 & (-\omega + \Omega_B) \end{bmatrix},$$

$$P_H = \begin{bmatrix} \gamma K_x M_0 & 0 & \gamma K_x M_0 & 0 \\ 0 & \gamma K_x M_0 & 0 & \gamma K_x M_0 \\ \gamma K_x M_0 & 0 & \gamma K_x M_0 & 0 \\ 0 & \gamma K_x M_0 & 0 & \gamma K_x M_0 \end{bmatrix},$$

$$R = \begin{bmatrix} i\alpha_{AA}\omega & i\alpha_{AB}\omega & 0 & 0 \\ i\alpha_{BA}\omega & i\alpha_{BB}\omega & 0 & 0 \\ 0 & 0 & i\alpha_{AA}\omega & i\alpha_{AB}\omega \\ 0 & 0 & i\alpha_{BA}\omega & i\alpha_{BB}\omega \end{bmatrix}.$$

P_H is the contribution from the hard axis to the magnetization components, while R is the contribution from damping. The sum $P_0 + R$ is the uncoupled matrix in Eq. (3.7). In the limit of $K_x = 0$, we should have the easy axis antiferromagnet with circular precession of the modes. Substituting this in P_H , Eq. (3.7) is retrieved, indicating that the matrix equation is on reasonable form.

In contrast to the easy axis AFM, the plus and minus modes are coupled for the biaxial AFM. Observing the matrix P_H , it is clear that the coupling stems from the hard axis contributions to the system. By applying a plus circularly polarized field excites both modes simultaneously, however close to and at the resonance frequency the plus polarized

mode dominates (Gurevich and Melkov, 1996), since this mode is closer to the motion of the right circular polarized applied field. The reverse is true for minus polarized applied field. The mixing of the two orthogonal modes is associated with breaking of rotational symmetry of the energy of the system, and contributes to the lifting of degeneracy of the modes (Liensberger et al., 2019). Analogous to the effect of demagnetization fields (Gurevich and Melkov, 1996), the hard axis restricts the motion of the magnetization in one direction, in this case the x-direction, since it is energetically unfavorable for the magnetization to have a component in this direction. This results in an elliptical precession of the sublattice magnetizations. The precession is in the xy-plane because the static part of the applied field is in the z-direction. Similarly to the easy axis case, the plus and minus modes have distinct resonance frequencies due to the symmetry breaking, consistent with (Johansen and Brataas, 2017).

3.2.2 Dc spin pumping current density and ISHE-voltage

Analytic results

The ground state of the biaxial AFM is the same as for the easy axis AFM, thus we can use the same expressions for the dc spin current (Eq. (3.16)) and the induced ISHE-voltage Eq. (3.17). However, due to the coupling of the two modes, the spin currents are dramatically different in the two cases. Since both modes are excited simultaneously, the spin current will have two peaks regardless of the polarization of the applied field. This reduces the spin current pumped from the AFM, as the two modes give oppositely polarized spin currents.

Numerical results

Due to the complex nature of the inverse susceptibility tensor, $P_0 + P_H + R$, we must resort to numerical calculations to obtain the solution to the LLG-equations. As it is the spin current that is of particular interest in this thesis, only the results for the spin current are presented.

Fig. 3.6 shows a plotted of the dc spin current as a function of frequency ω for four different values of H_0 , for the biaxial AFM in collinear ground state. Here the applied field is right circularly polarized. As discussed above, the spin current displays two peaks, one positive and one negative, due to the coupling of the modes. However, the positive (negative) peak increases (decreases) as the field strength is raised, and the negative peak has nearly vanished for $H_0 = 0.45/\mu_0$. In addition the distance between the peaks is enlarged. This indicates that the coupling between the two modes decreases and is nearly lifted for the large field value. We also see that the peak of the spin current is smaller than

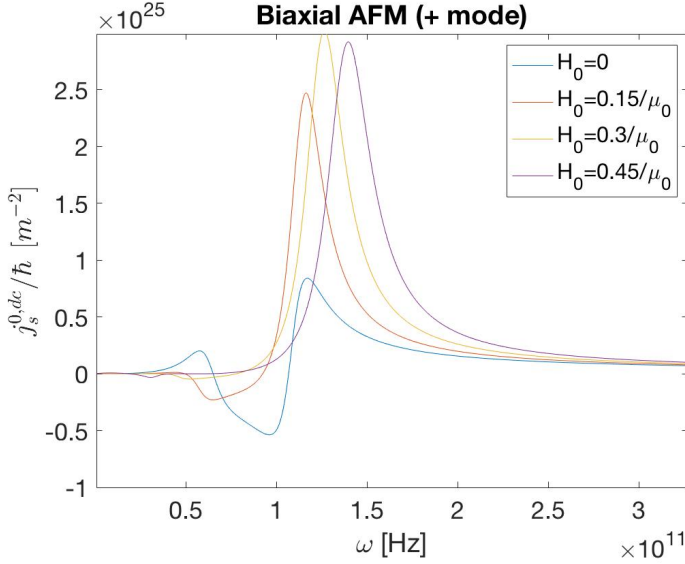


Figure 3.6: The dc spin pumping current, for the biaxial AFM, as a function of frequency, ω , for four different values of H_0 . A right circularly polarized magnetic field has been applied.

for the $H_0 = 0.3/\mu_0$. This is similar to the easy axis AFM/normal metal-bilayer, where the peak decreases as a function of H_0 . An interesting case is $H_0 = 0$. Observing the blue curve, the spin current has three peaks, which is not consistent with the analysis above. This is attributed to a phenomenon called hybridization, which occurs when the two coupled modes are close in energy (Kim et al., 2018). When two modes are hybridized, both modes are equally excited resulting in linear polarization of the magnetization precession (Liensberger et al., 2019) (see Fig. 3.7).

Fig. 3.8 displays the spin current as a function of ω for the biaxial AFM, influenced by a left circularly polarized applied field, for different values of H_0 . In this case the minus mode dominates over the plus mode, explaining the observed larger negative peaks compared to the positive peaks, which is expected from the magnetization dynamics. Similar to the analysis in the previous paragraph, the two modes are coupled and the coupling is weakened for increasing field strength. In addition, the hybridized mode of the magnetizations is apparent for $H_0 = 0$, although inverted. This suggests that the polarization of the spin current is opposite for these two cases. Another distinction is that the positive peaks in Fig. 3.8 are larger than the negative peaks in Fig. 3.6. This is due to the fact that the magnetization vectors have a different response to the plus and minus polarized ac-field, since the static applied field is in the z-direction.

Exciting the magnet using a linearly polarized field, we obtain the results in Fig. 3.9.

Hybridized mode

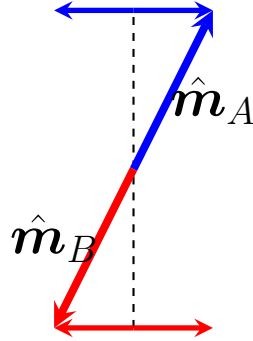


Figure 3.7: Schematic depiction of the hybridized mode of the biaxial antiferromagnet in collinear ground state. The mode is linearly polarized with equal angles between the sublattice magnetizations.

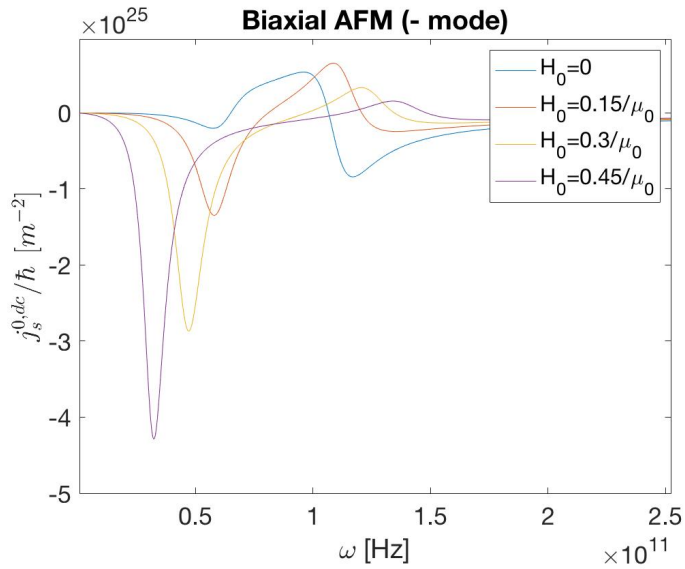


Figure 3.8: The dc spin pumping current, for the biaxial AFM, as a function of frequency, ω for four different values of H_0 . A left circularly polarized magnetic field has been applied.

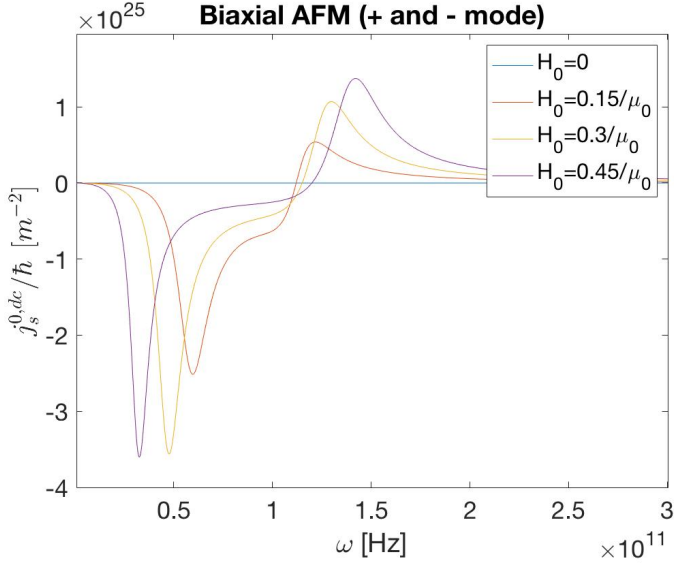


Figure 3.9: The dc spin pumping current, for the biaxial AFM, as a function of frequency, ω , for four different values of H_0 . A linearly polarized field is applied.

The positive peaks are larger than in Fig. 3.8, but smaller than in Fig. 3.6 for the same values of H_0 (except for $H_0 = 0$). This is peculiar, as one might expect the peaks to add constructively when both a linearly polarized field is applied. The peak values also increase as a function of H_0 , which is consistent with the behaviour in Fig. 3.6 for all but the purple curve. For the negative peaks on the other hand, the peak amplitudes have increased (except for the purple curve) compared to the two other cases. For $H_0 = 0$, the spin current from the two modes cancels. This is reasonable considering that both modes are excited simultaneously and the polarization of the spin pumping current is opposite for the two modes (see. Eq. (3.16)). Considering the above results, it is clear that the coupling of the modes has an important effect on the dc spin current injected into the normal metal. Exciting the biaxial AFM with a left circularly polarized field, at ω_- , produces the largest dc spin current.

In Fig. 3.10, the spin current is plotted for different values of the cross-sublattice spin mixing conductance for linearly polarized applied field. The same parameters have been employed as in the easy axis case. We observe the same effect as before when the mixing conductance is increased. There is no effect on the behaviour of the curve from the cross-sublattice spin pumping terms.

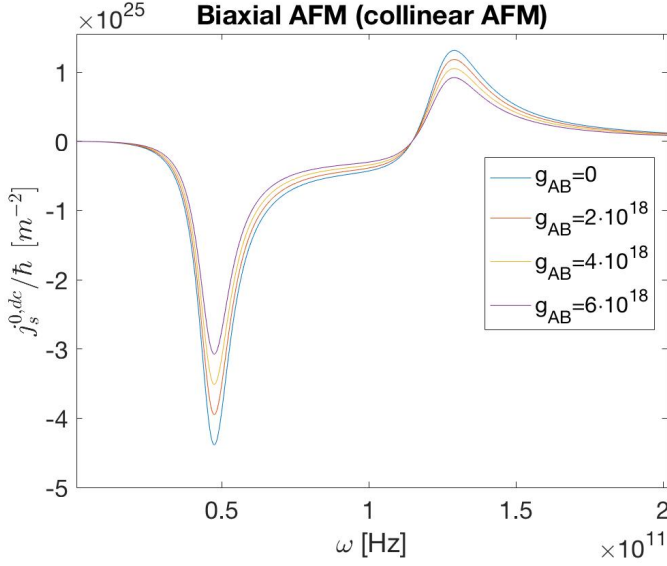


Figure 3.10: The dc spin pumping current, for the biaxial AFM, as a function of frequency, ω , for four different values of g_{AB} . A linearly polarized field is applied.

3.3 Easy axis antiferromagnet in spin flop state, static applied field

3.3.1 Magnetization dynamics

We now remove the hard axis, such that we have the symmetric easy axis antiferromagnet again. Consider applying a magnetic field along the easy axis with \mathbf{H}_0 above the spin flop field. The antiferromagnet is then in the spin flop state and the ground state of the system is non-collinear. Before considering oscillations, we first find the ground state configuration of the sublattice magnetizations. The free energy of the system reads:

$$\begin{aligned}
 F[\mathbf{M}_A, \mathbf{M}_B] &= \int_{dV} d^3r \left(-\mu_0 \mathbf{H}_0 (\mathbf{M}_A + \mathbf{M}_B) - K_z M_{Az}^2 - K_z M_{Bz}^2 + J \mathbf{M}_A \cdot \mathbf{M}_B \right) \\
 &= \int_{dV} d^3r \left(-\mu_0 H_0 (M_0 \cos \theta - M_0 \cos \phi) - K_z M_0^2 \cos^2 \theta - \right. \\
 &\quad \left. K_z M_0^2 \cos^2 \phi + J M_0^2 \cos(\theta + \phi) \right),
 \end{aligned} \tag{3.24}$$

where θ and ϕ are the angles subtended by M_A and M_B , respectively (see Fig. 3.11). Using Eqs. (2.19) and (2.20), and noting that $\phi = \theta$ due to the assumed symmetry of the antiferromagnet, we obtain the ground state configuration of the system described by:

$$\theta = \arccos \frac{\mu_0 H_0}{(2J - K_z)M_0}. \quad (3.25)$$

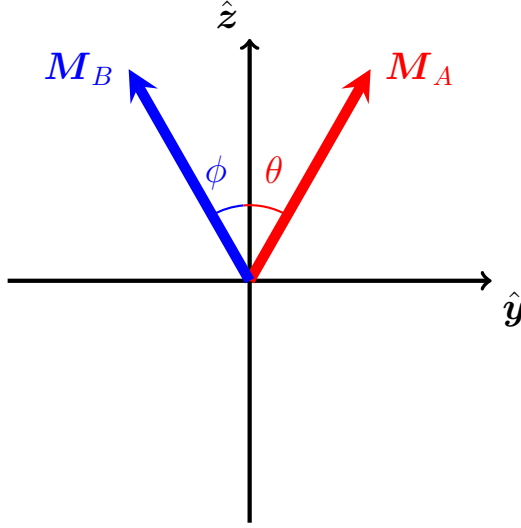


Figure 3.11: Schematic depiction of the ground state configuration of the antiferromagnet for static external applied field along the easy (z -) axis

This is only valid for fields between the spin flop and spin flip fields. Taking the derivative of the free energy twice with respect to the angle, substituting the expression for the angle and solving for H_0 , we obtain:

$$\mu_0 H_{C1} = \sqrt{K_z M_0 (K_z M_0 + 2J M_0)}, \quad (3.26)$$

where the subscript denotes the first critical field. The spin flip state corresponds to $\theta = 0$, thus the spin flip field is $\mu_0 H_{C2} = (2J - K_z)M_0$, where C2 denotes the second critical field. The condition then translates to:

$$0 < \theta \leq \arccos \frac{\mu_0 H_{C1}}{(2J - K_z)M_0}. \quad (3.27)$$

With the ground state configuration established, let's consider the dynamics. The applied field is now oscillating with small time-variations, as in Sec. 3.1.1. The free energy

is then:

$$F[\mathbf{M}_A, \mathbf{M}_B] = \int_{dV} d^3r \left(-\mu_0 \mathbf{H}(\mathbf{M}_A + \mathbf{M}_B) - K_z M_{Az}^2 - K_z M_{Bz}^2 + J \mathbf{M}_A \cdot \mathbf{M}_B \right), \quad (3.28)$$

giving the effective fields:

$$\mathbf{B}_A = \mu_0 \mathbf{H} + 2K_z M_{Az} \hat{\mathbf{z}} - J \mathbf{M}_B \quad (3.29)$$

$$\mathbf{B}_B = \mu_0 \mathbf{H} + 2K_z M_{Bz} \hat{\mathbf{z}} - J \mathbf{M}_A. \quad (3.30)$$

Since the sublattice magnetization vectors are non-collinear with the applied field, it is convenient to work in different coordinates systems when investigating the dynamics. Defining two new coordinate systems, as shown in Fig. 3.12, the sublattice magnetization vectors can be represented as:

$$\mathbf{M}_A = m_{A_x} \hat{\mathbf{x}} + m_{A_y} \hat{\mathbf{y}}' + M_{A_z} \hat{\mathbf{z}}' \quad (3.31)$$

$$\mathbf{M}_B = m_{B_x} \hat{\mathbf{x}} + m_{B_y} \hat{\mathbf{y}}'' + M_{B_z} \hat{\mathbf{z}}'', \quad (3.32)$$

where $|m_{A_x}|, |m_{A_y}| \ll M_0$ and $|m_{B_x}|, |m_{B_y}| \ll M_0$. Note, that the choice of the double primed coordinate system is made to be consistent with the calculations in the collinear case. The x-axis coincides for all three coordinate systems. The effective fields to be employed in the LLG-equations now need to be expressed in these new coordinates. Utilizing the coordinate transformations in Sec. 4.3 we have:

$$\begin{aligned} \mu_0 \mathbf{H} &= \mu_0 [h_x \hat{\mathbf{x}} + (h_y \cos \theta - H_0 \sin \theta) \hat{\mathbf{y}}' + (h_y \sin \theta + H_0 \cos \theta) \hat{\mathbf{z}}'] \\ 2K_z M_{Az} \hat{\mathbf{z}} &= 2K_A (M_0 \cos \theta - m_{A_y} \sin \theta) (\hat{\mathbf{z}}' \cos \theta - \hat{\mathbf{y}}' \sin \theta) \\ &= K_z [(2m_{A_y} \sin^2 \theta - M_0 \sin 2\theta) \hat{\mathbf{y}}' + \\ &\quad (2M_0 \cos^2 \theta - m_{A_y} \sin 2\theta) \hat{\mathbf{z}}'] \\ -J \mathbf{M}_B &= -J (m_{B_x} \hat{\mathbf{x}} + m_{B_y} \hat{\mathbf{y}}'' + M_{B_z} \hat{\mathbf{z}}'') \\ &= -J (m_{B_x} \hat{\mathbf{x}} - (m_{B_y} \cos 2\theta + M_0 \sin 2\theta) \hat{\mathbf{y}}' + \\ &\quad (M_0 \cos 2\theta - m_{B_y} \sin 2\theta) \hat{\mathbf{z}}'), \end{aligned}$$

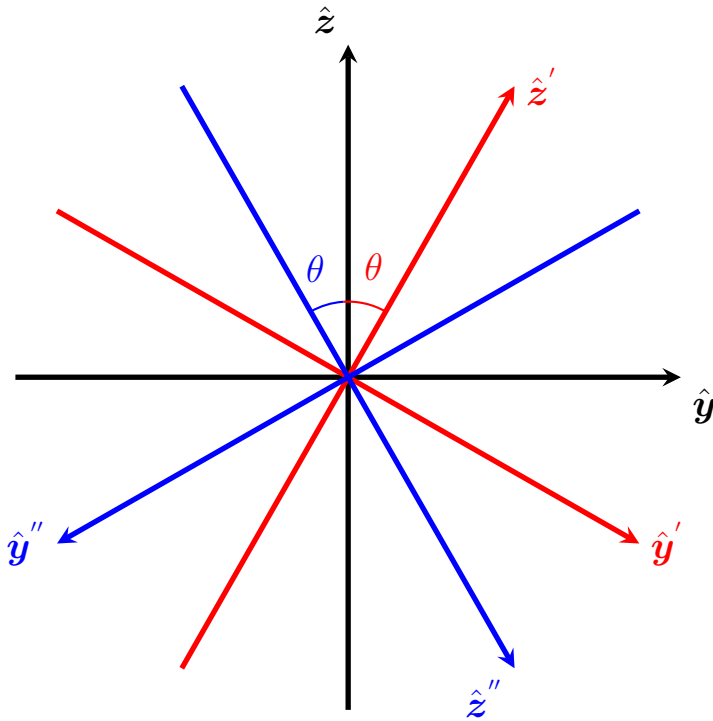


Figure 3.12: Schematic depiction of the three coordinate systems employed in describing the dynamics of the system. In the ground state $\vec{M}_A = M_{A0}\hat{z}'$ and $\vec{M}_B = -M_{B0}\hat{z}''$. The x-coordinate for the three coordinate systems coincide

for the terms in B_A . Doing the same for B_B , we obtain the effective fields in the desired representation:

$$B_A = (-Jm_{B_x} + \mu_0 h_x)\hat{x} + [\mu_0 h_y \cos \theta + 2K_z m_{A_y'} \sin^2 \theta - K_z M_0 \sin 2\theta - \quad (3.33)$$

$$\mu_0 H_0 \sin \theta + JM_0 \sin 2\theta + Jm_{B_y''} \cos \theta]\hat{y}' + [\mu_0 h_y \sin \theta + \mu_0 H_0 \cos \theta +$$

$$2K_z M_0 \cos^2 \theta - K_z m_{B_y''} \sin 2\theta - JM_0 \cos 2\theta]\hat{z}'$$

and

$$\begin{aligned}
 \mathbf{B}_B = & (-Jm_{A_x} + \mu_0 h_x) \hat{\mathbf{x}} + [-\mu_0 h_y \cos \theta + 2K_z m_{B_{y''}} \sin^2 \theta - K_z M_0 \sin 2\theta - \\
 & \mu_0 H_0 \sin \theta + JM_0 \sin 2\theta + Jm_{A_{y'}} \cos 2\theta] \hat{\mathbf{y}}'' + [\mu_0 h_y \sin \theta - \mu_0 H_0 \cos \theta - \\
 & 2K_z M_0 \cos^2 \theta + K_z m_{B_{y''}} \sin 2\theta - Jm_{A_{y'}} \sin 2\theta + JM_0 \cos 2\theta] \hat{\mathbf{z}}''
 \end{aligned} \tag{3.34}$$

In contrast to the collinear cases, all components of the effective fields contain time-dependent terms due to the non-collinearity of the sublattice magnetizations. Again, assuming harmonic oscillation of the fields, employing the expressions for the above effective fields in the LLG-equations, and follow a similar procedure as a before, the equations can be written:

$$\pm \omega \hat{m}_{A_{\pm}} = (C + i\alpha_{AA}\omega) \hat{m}_{A_{\pm}} + \frac{\gamma JM_0 + i\alpha_{AB}\omega}{2} \left[\hat{m}_{B_+} (1 \mp \cos \theta) + \hat{m}_{B_-} (1 \pm \cos \theta) \right] \tag{3.35}$$

$$- \frac{w}{2} \sin^2 \theta (\hat{m}_{A_+} + \hat{m}_{A_-}) - \frac{\gamma \mu_0}{2} \left[\hat{h}_+ (1 \pm \cos \theta) + \hat{h}_- (1 \mp \cos \theta) \right]$$

$$\mp \omega \hat{m}_{B_{\pm}} = (\mathcal{D} + i\alpha_{BB}\omega) \hat{m}_{B_{\pm}} + \frac{\gamma JM_0 + i\alpha_{BA}\omega}{2} \left[\hat{m}_{A_+} (1 \mp \cos \theta) + \hat{m}_{A_-} (1 \pm \cos \theta) \right] \tag{3.36}$$

$$- \frac{w}{2} \sin^2 \theta (\hat{m}_{B_+} + \hat{m}_{B_-}) - \frac{\gamma \mu_0}{2} \left[\hat{h}_+ (1 \mp \cos \theta) + \hat{h}_- (1 \pm \cos \theta) \right],$$

where we have used $\hat{m}_{A,B} = \hat{m} e^{i\omega t}$, $\hat{m}_{A_{\pm}, B_{\pm}} = \hat{m}_{A_x, B_x} \pm i \hat{m}_{A_{y'}, B_{y''}}$ etc., $w = 2K_z M_0$ and $C = \mathcal{D} = \gamma(\mu_0 H_0 \cos \theta + 2K_z M_0 \cos 2\theta - JM_0 \cos 2\theta)$. For an asymmetric antiferromagnet, C and \mathcal{D} would not be equal since $\gamma_A = \gamma_B = \gamma$ and $M_{A0} = M_{B0} = M_0$ do not hold. Note that the definitions $\hat{m}_{A_x, B_x} = m_{A_x, B_x} / M_0$ etc. have been employed. We see from the two equations that the torques acting on the sublattice magnetizations are dependent on the angle θ (except for the intra-sublattice damping terms). Noting that $1 + \cos 2\theta = 2 \cos^2 \theta$ and $1 - \cos 2\theta = 2 \sin^2 \theta$, these equations can be represented in matrix form as:

$$\tilde{m} = (P_0 + P_E + R)^{-1} \tilde{h}, \quad (3.37)$$

where in this case we have:

$$\tilde{m} = \begin{bmatrix} \hat{m}_{A+} \\ \hat{m}_{B+} \\ \hat{m}_{A-} \\ \hat{m}_{B-} \end{bmatrix}, \quad \tilde{h} = \begin{bmatrix} 1 + \cos \theta & 1 - \cos \theta \\ 1 - \cos \theta & 1 + \cos \theta \\ 1 - \cos \theta & 1 + \cos \theta \\ 1 + \cos \theta & 1 - \cos \theta \end{bmatrix} \begin{bmatrix} \gamma \mu_0 \hbar_+ / 2 \\ \gamma \mu_0 \hbar_- / 2 \end{bmatrix}$$

$$P_0 = \begin{bmatrix} -(\omega - \mathcal{C}) & (\gamma J M_0 \sin^2 \theta) / 2 & 0 & (\gamma J M_0 \cos^2 \theta) / 2 \\ (\gamma J M_0 \sin^2 \theta) / 2 & (\omega + \mathcal{D}) & \gamma J M_0 \cos^2 \theta & 0 \\ 0 & (\gamma J M_0 \cos^2 \theta) / 2 & -(-\omega - \mathcal{C}) & (\gamma J M_0 \sin^2 \theta) / 2 \\ (\gamma J M_0 \cos^2 \theta) / 2 & 0 & (\gamma J M_0 \sin^2 \theta) / 2 & (-\omega + \mathcal{D}) \end{bmatrix},$$

$$P_E = -\frac{1}{2} \begin{bmatrix} w \sin^2 \theta & 0 & w \sin^2 \theta & 0 \\ 0 & w \sin^2 \theta & 0 & w \sin^2 \theta \\ w \sin^2 \theta & 0 & w \sin^2 \theta & 0 \\ 0 & w \sin^2 \theta & 0 & w \sin^2 \theta \end{bmatrix},$$

$$R = \begin{bmatrix} i\alpha_{AA\omega} & (i\alpha_{AB\omega} \sin^2 \theta) / 2 & 0 & (i\alpha_{AB\omega} \cos^2 \theta) / 2 \\ i\alpha_{BA\omega} \sin^2 \theta / 2 & i\alpha_{BB\omega} & (i\alpha_{BA\omega} \cos^2 \theta) / 2 & 0 \\ 0 & (i\alpha_{AB\omega} \cos^2 \theta) / 2 & i\alpha_{AA\omega} & (i\alpha_{AB\omega} \sin^2 \theta) / 2 \\ (i\alpha_{BA\omega} \cos^2 \theta) / 2 & 0 & (i\alpha_{BA\omega} \sin^2 \theta) / 2 & i\alpha_{BB\omega} \end{bmatrix}.$$

Here, P_E is the contribution from the easy axis anisotropy and R the Gilbert damping contributions. Similar to the biaxial case the two modes are coupled, however the coupling is stronger in this case due to the effect of the non-collinearity on the exchange coupling between the sublattice magnetizations, the cross-sublattice damping and easy axis anisotropy energy. As a consequence, P_0 is no longer an uncoupled matrix, in contrast to the collinear case. By substituting $\theta = \pi/2$ in Eq. (3.37), we can check if the obtained matrix equation is on reasonable form. This corresponds to a collinear orientation of the sublattice magnetizations (in the y-direction). The y-direction then corresponds to the easy axis and the z-axis to one of the hard axes. Since the anisotropy term in the free energy is in the z-

direction, the matrix equation should be similar to the one for the biaxial antiferromagnet above. Making the substitution decouples the matrix P_0 . P_E and P_H differ by a minus sign, and R takes the same form as in the biaxial case. This indicates that the equation Eq. (3.37) is correct.

When calculating the resonance frequencies of eigenoscillations, i.e un-damped motion ($R=0$), one finds that there is only one non-zero frequency corresponding to the plus mode (Gurevich and Melkov, 1996). Taking the determinant, D , of $P_0 + P_E$ and solving the equation $D = 0$ for ω , one can obtain the following resonance frequencies:

$$\omega_+ = \gamma \sqrt{\frac{2J(2J + K_z)}{(2J - K_z)^2} (\mu_0 H_0)^2 - 2JK_z M_0^2} \quad (3.38)$$

$$\omega_- = 0. \quad (3.39)$$

Thus, the A and B sublattice magnetizations only have right circular precession about the \hat{z}' - and \hat{z}'' -axis, respectively. The zero-frequency corresponds to an infinitely slow precession. The minus mode is therefore called a soft mode. The appearance of such a mode is due to the breaking of cylindrical symmetry in the energy by the ground state. Observing the expression for \tilde{h} it is clear that the plus mode can be excited by both a left and right circularly polarized oscillation of the applied field. The precession amplitude will be different however since the torque on the magnetizations is different, as seen from Eqs. (3.35) and (3.36) (remember that the LLG-equation is a torque equation).

3.3.2 Dc spin pumping current and ISHE-voltage

Analytic results

Note that the analytic spin current expressions calculated, does not assume any free energy of the magnet, and is thus general for this type of configuration. The non-collinearity of the magnetizations introduces complexity to the cross-sublattice spin pumping terms in Eq. (3.12). The intra-sublattice terms however, can be evaluated in the same manner as in the collinear case since both magnetizations have a static component in the \hat{z}' - (A sublattice) and \hat{z}'' - direction (B sublattice). We therefore have

$$j_{s,intra}^{0,dc} \langle \hat{s} \rangle = \frac{\hbar\omega}{16\pi} \left[g_{AA} (|\hat{m}_{A+}|^2 - |\hat{m}_{A-}|^2) \hat{z}' + g_{BB} (|\hat{m}_{B+}|^2 - |\hat{m}_{B-}|^2) \hat{z}'' \right]. \quad (3.40)$$

In the bilayer model considered in Sec. 2.4, the interface is parallel to the z-direction. Thus, the magnetization components must be transformed from the primed and double primed coordinates to yz-coordinates. Using the transformation rules Eqs. (4.18) and (4.22), the intra-sublattice spin current is written:

$$\begin{aligned}
 j_{s,intra}^{0,dc} \langle \hat{\mathbf{s}} \rangle &= \frac{\hbar\omega}{16\pi} \left[\sin \theta \left(g_{AA} (|\hat{m}_{A+}|^2 - |\hat{m}_{A-}|^2) + g_{BB} (|\hat{m}_{A+}|^2 - |\hat{m}_{A-}|^2) \right) \hat{\mathbf{y}} \right. \\
 &\quad \left. + \cos \theta \left(g_{AA} (|\hat{m}_{A+}|^2 - |\hat{m}_{A-}|^2) - g_{BB} (|\hat{m}_{A+}|^2 - |\hat{m}_{A-}|^2) \right) \hat{\mathbf{z}} \right]
 \end{aligned} \tag{3.41}$$

Due to the non-collinearity, the spin current now has a polarization component in the y-direction in addition to the z-direction.

A bit more care is needed for the cross-sublattice contributions. Due to the non-collinearity, it is simplest to do the transformations to yz-coordinates first and then calculate the cross-products. Applying Eqs. (4.18) and (4.22) on the unit vector magnetizations:

$$\hat{\mathbf{m}}_A = \hat{m}_{A_x} \hat{\mathbf{x}} + \hat{m}_{A_{y'}} \hat{\mathbf{y}}' + \hat{\mathbf{z}}' \tag{3.42}$$

$$\hat{\mathbf{m}}_B = \hat{m}_{B_x} \hat{\mathbf{x}} + \hat{m}_{B_{y''}} \hat{\mathbf{y}}'' - \hat{\mathbf{z}}'', \tag{3.43}$$

we have:

$$\hat{\mathbf{m}}_A = \hat{m}_{A_x} \hat{\mathbf{x}} + (\hat{m}_{A_{y'}} \cos \theta + \sin \theta) \hat{\mathbf{y}} + (\cos \theta - \hat{m}_{A_{y'}} \sin \theta) \hat{\mathbf{z}} \tag{3.44}$$

$$\hat{\mathbf{m}}_B = \hat{m}_{B_x} \hat{\mathbf{x}} - (\hat{m}_{B_{y''}} \cos \theta + \sin \theta) \hat{\mathbf{y}} + (\cos \theta - \hat{m}_{B_{y''}} \sin \theta) \hat{\mathbf{z}}. \tag{3.45}$$

Before preceding, the calculations can be simplified by noting that all terms to first order in the magnetization components vanish upon time averaging. Thus, the terms to zeroth order in the magnetization components in Eqs. (3.44) and (3.45) can be disregarded. Taking the cross-products, we obtain:

$$\begin{aligned} \hat{\mathbf{m}}_A \times \dot{\hat{\mathbf{m}}}_B &= (-m_{A_y} \dot{m}_{B_{y''}} \sin 2\theta, (\hat{m}_{A_x} \dot{m}_{B_{y''}} - \hat{m}_{A_{y'}} \dot{m}_{B_x}) \sin \theta, \\ &\quad - (\hat{m}_{A_x} \dot{m}_{B_{y''}} + \hat{m}_{A_{y'}} \dot{m}_{B_x}) \cos \theta) \end{aligned} \quad (3.46)$$

$$\begin{aligned} \hat{\mathbf{m}}_B \times \dot{\hat{\mathbf{m}}}_A &= (m_{A_y} \dot{m}_{B_{y''}} \sin 2\theta, (\hat{m}_{B_x} \dot{m}_{A_{y'}} - \hat{m}_{B_{y''}} \dot{m}_{A_x}) \sin \theta, \\ &\quad (\hat{m}_{B_x} \dot{m}_{A_{y'}} + \hat{m}_{B_{y''}} \dot{m}_{A_x}) \cos \theta). \end{aligned} \quad (3.47)$$

All components contain terms to second order in the magnetization components which is non-zero upon time averaging. The spin current therefore has a component polarized in all three directions. Compared to the intra-sublattice contributions, we see that the existence of a polarization in the x-direction is purely due to cross-sublattice spin pumping. However, since the spin current travels in the x-direction in the normal metal, this component cannot be measured experimentally as $\hat{\mathbf{x}} \times \langle \hat{\mathbf{s}} \rangle_x = 0$ in Eq. (2.59), in the chosen set up.

Evaluating the x-component first, using that $g_{AB} = g_{BA}$ we have:

$$j_{s,cross}^{0,dc} \langle \hat{\mathbf{s}} \rangle_x = \frac{\hbar g_{AB} \sin 2\theta}{4\pi} \left[\langle \dot{m}_{A_{y'}} \hat{m}_{B_{y''}} - \hat{m}_{A_{y'}} \dot{m}_{B_{y''}} \rangle \right] \hat{\mathbf{x}}. \quad (3.48)$$

This needs to be expressed in complex variables in order for the results for the magnetization dynamics to be employed. The magnetization components can be expressed in their complex amplitudes as follows:

$$\hat{m}_{A_x, B_x} = \frac{1}{2} (\hat{m}_{A_x, B_x} e^{i\omega t} + \hat{m}_{A_x, B_x}^* e^{-i\omega t}) \quad (3.49)$$

$$\hat{m}_{A_{y'}, B_{y''}} = \frac{1}{2} (\hat{m}_{A_{y'}, B_{y''}} e^{i\omega t} + \hat{m}_{A_{y'}, B_{y''}}^* e^{-i\omega t}), \quad (3.50)$$

Substituting this is the expression above and taking the time average, the x-component becomes:

$$j_{s,cross}^{0,dc} \langle \hat{\mathbf{s}} \rangle_x = -\frac{\hbar g_{AB} \omega \sin 2\theta}{4\pi} \text{Im}(\hat{m}_{B_{y''}}^* \hat{m}_{A_{y'}}) \hat{\mathbf{x}} \quad (3.51)$$

Lastly, we must switch to a circular basis. Utilizing the same basis as for the magnetization dynamics, the contribution from the cross-sublattice terms polarized in the x-direction reads:

$$j_{s,cross}^{0,dc} \langle \hat{\mathbf{s}} \rangle_x = \frac{\hbar g_{AB} \omega \sin 2\theta}{16\pi} \text{Im} \left[\hat{m}_{B-}^* \hat{m}_{A+} + \hat{m}_{A-} \hat{m}_{B+}^* - \hat{m}_{B-}^* \hat{m}_{A-} - \hat{m}_{B+}^* \hat{m}_{A+} \right] \hat{\mathbf{x}}. \quad (3.52)$$

The analytic expression is seemingly non-zero, however its value is determined by the magnetization amplitudes. Nevertheless, this contribution cannot be detected experimentally for the bilayer model used in this thesis, as already discussed.

Continuing with the y- and z-components:

$$j_{s,cross}^{0,dc} \langle \hat{\mathbf{s}} \rangle_y = \frac{\hbar g_{AB} \sin \theta}{4\pi} \left[\langle \hat{m}_{A_x} \dot{\hat{m}}_{B_{y''}} - \hat{m}_{A_y} \dot{\hat{m}}_{B_x} + \hat{m}_{B_x} \dot{\hat{m}}_{A_{y'}} - \hat{m}_{B_{y''}} \dot{\hat{m}}_{A_x} \rangle \right] \hat{\mathbf{y}}. \quad (3.53)$$

and

$$j_{s,cross}^{0,dc} \langle \hat{\mathbf{s}} \rangle_z = \frac{\hbar g_{AB} \cos \theta}{4\pi} \left[\langle \hat{m}_{B_x} \dot{\hat{m}}_{A_{y'}} + \hat{m}_{B_{y''}} \dot{\hat{m}}_{A_x} - (\hat{m}_{A_x} \dot{\hat{m}}_{B_{y''}} + \hat{m}_{A_{y'}} \dot{\hat{m}}_{B_x}) \rangle \right] \hat{\mathbf{z}}. \quad (3.54)$$

Following the same procedure as before, we obtain:

$$j_{s,cross}^{0,dc} \langle \hat{\mathbf{s}} \rangle_y = \frac{\hbar g_{AB} \omega \sin \theta}{8\pi} \text{Re}(\hat{m}_{A+}^* \hat{m}_{B+} - \hat{m}_{A-}^* \hat{m}_{B-}) \hat{\mathbf{y}}. \quad (3.55)$$

and

$$j_{s,cross}^{0,dc} \langle \hat{\mathbf{s}} \rangle_z = \frac{\hbar g_{AB} \omega \cos \theta}{8\pi} \text{Re}(\hat{m}_{A-}^* \hat{m}_{B+} - \hat{m}_{A+}^* \hat{m}_{B-}) \hat{\mathbf{z}}. \quad (3.56)$$

Similar to the collinear case, the cross-sublattice spin pumping contributions are non-zero. We also see that the angular dependence of the y- and z-polarized contributions is the same as for the intra-sublattice contributions. In addition to the angular dependence, the two expressions differ in the coupling of the modes. In Eq. (3.55), the two modes are decoupled, as in the collinear case, while in Eq. (3.56) the modes are coupled. Adding the intra- and cross-sublattice terms, the total dc spin pumping current reads:

$$j_s^{0,dc} \langle \hat{\mathbf{s}} \rangle = j_{s_x}^{0,dc} \langle \hat{\mathbf{s}} \rangle_x + j_{s_y}^{0,dc} \langle \hat{\mathbf{s}} \rangle_y + j_{s_z}^{0,dc} \langle \hat{\mathbf{s}} \rangle_z, \quad (3.57)$$

with

$$j_s^{0,dc} \langle \hat{\mathbf{s}} \rangle_x = \frac{\hbar g_{AB} \omega \sin 2\theta}{16\pi} \left[\hat{m}_{B-}^* \hat{m}_{A+} + \hat{m}_{A-} \hat{m}_{B+}^* - \hat{m}_{B-}^* \hat{m}_{A-} - \hat{m}_{B+}^* \hat{m}_{A+} \right] \hat{\mathbf{x}} \quad (3.58)$$

$$j_s^{0,dc} \langle \hat{\mathbf{s}} \rangle_y = \frac{\hbar\omega \sin \theta}{16\pi} \left[g_{AA}(|\hat{m}_{A+}|^2 - |\hat{m}_{A-}|^2) + g_{BB}(|\hat{m}_{A+}|^2 - |\hat{m}_{A-}|^2) + \right. \\ \left. 2\text{Re}(\hat{m}_{A+}^* \hat{m}_{B+} - \hat{m}_{A-}^* \hat{m}_{B-}) \right] \hat{\mathbf{y}} \quad (3.59)$$

$$j_s^{0,dc} \langle \hat{\mathbf{s}} \rangle_z = \frac{\hbar\omega \cos \theta}{16\pi} \left[g_{AA}(|\hat{m}_{A+}|^2 - |\hat{m}_{A-}|^2) - g_{BB}(|\hat{m}_{A+}|^2 - |\hat{m}_{A-}|^2) + \right. \\ \left. 2\text{Re}(\hat{m}_{A-}^* \hat{m}_{B+} - \hat{m}_{A+}^* \hat{m}_{B-}) \right] \hat{\mathbf{z}}. \quad (3.60)$$

In this case, the voltage can be measured across two of the edges in the normal metal. This provides a possibility to isolate the cross-sublattice terms by combining the spin current polarized in the y- and z-direction. By setting $\theta = \pi/2$, the spin current expression should be equal to that in the collinear case, however the polarization should be in the y-direction as this corresponds to a collinear orientation of the sublattice magnetizations. Doing this, only y-polarized current is non-zero. Disregarding the polarization direction, the expressions Eq. (3.55) and Eq. (3.16) concur as expected. Substituting the current expression in Eq. (2.59), yields the measurable voltages:

$$V_y = -\frac{\gamma_H e \lambda_{sd} L \omega \cos \theta}{8\pi(\sigma_N t_N + \sigma_F t_F)} \tanh \frac{t_N}{2\lambda_{sd}} \left[g_{AA}(|\hat{m}_{A+}|^2 - |\hat{m}_{A-}|^2) - g_{BB}(|\hat{m}_{A+}|^2 - |\hat{m}_{A-}|^2) \right. \\ \left. + 2g_{AB} \text{Re}(\hat{m}_{A-}^* \hat{m}_{B+} - \hat{m}_{A+}^* \hat{m}_{B-}) \right], \quad (3.61)$$

and

$$V_z = \frac{\gamma_H e \lambda_{sd} L \omega \sin \theta}{8\pi(\sigma_N t_N + \sigma_M t_F)} \tanh \frac{t_N}{2\lambda_{sd}} \left[g_{AA}(|\hat{m}_{A+}|^2 - |\hat{m}_{A-}|^2) + g_{BB}(|\hat{m}_{A+}|^2 - |\hat{m}_{A-}|^2) \right. \\ \left. + 2g_{AB} \text{Re}(\hat{m}_{A+}^* \hat{m}_{B+} - \hat{m}_{A-}^* \hat{m}_{B-}) \right]. \quad (3.62)$$

Numerical results

The inverse susceptibility, $P_0 + P_E + R$, is even more complicated than in the biaxial case. Numerical calculations is therefore needed to obtain the expression for the magnetization components. Again, we skip presenting the numerical results for the magnetization components, since the spin current is of interest in this thesis. Considering the non-collinear

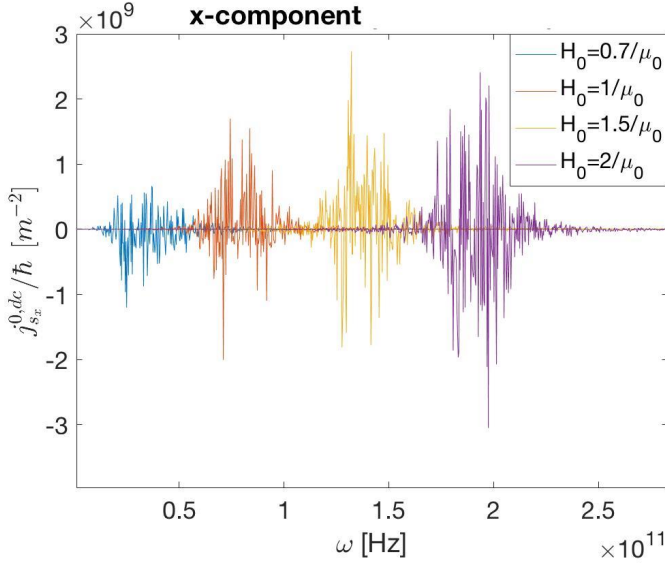


Figure 3.13: The dc spin pumping current polarized in the x-direction, as a function of frequency, ω , for four different values of H_0 . A linearly polarized field is applied.

ground state, the magnitude of the static applied field has to be above the spin flop field. Thus, the values for H_0 employed must be different for the collinear and non-collinear systems. For the parameters employed in this thesis the $H_{C1} \approx 0.64/\mu_0$. The other parameters are the same as in the two previous cases.

The x-component is solely due to cross-sublattice contributions. Thus, it does not make sense to plot this component for $g_{AB} = 0$. The cross-sublattice spin mixing conductance, $g_{AB} = 2 \cdot 10^{18}$, and damping parameter, $\alpha_{AB} = \alpha_{BA} = 0.001$, are therefore included in the calculations. Fig. 3.13 shows the spin current polarized in the x-direction as a function of frequency, for different values of H_0 . The figure displays noise due to the numerical calculations and is therefore zero. This suggests a canceling of the contribution from the two sublattices in the x-direction. Thus, this component cannot be used to measure the effect of the cross-sublattice terms. The same results are obtained for all polarizations of the applied field.

The spin current polarized in the y-direction is plotted in Fig. 3.14 for different values of H_0 and polarization of the oscillating field. We observe noise due to numerical errors in all cases. The spin current is therefore zero. The physical origin of the results has not been found in this work, although one possibility might be that the y-polarized spin current from the sublattice magnetizations cancels, since the sublattice magnetizations are π out of phase in the precessional motion. The plus mode for the B sublattice magnetiza-

tion is right circular precession about the \hat{z}'' -axis, however this corresponds to left circular polarization about the $-\hat{z}''$ -axis, which is the axis parallel to \hat{m}_B . Thus, the two sublattice magnetizations rotate in the opposite direction such that spin current polarized in the x- and y-directions cancel, while adding constructively in the z-direction. Nevertheless, a zero spin current polarized in the y-direction means that the cross-sublattice terms cannot be isolated and therefore not detected experimentally for this system.

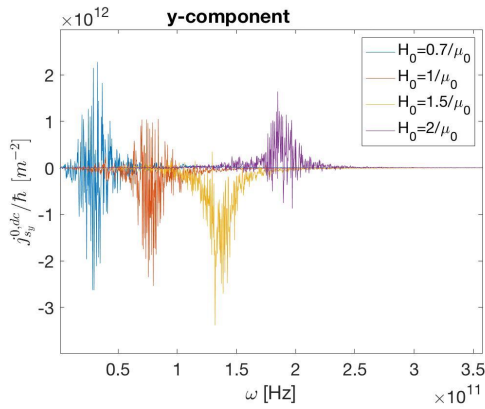
In Fig. 3.15 the component of the spin current polarized in the z-direction is shown for right circularly polarized applied field. We immediately observe that there is only one positive peak for each value of H_0 . This corresponds to the excited plus mode of the magnetizations, consistent with the analysis of the magnetization dynamics. The contributions from the two sublattices thus add constructively as in the collinear case, supporting the discussion above for the y-polarized component. Furthermore, the amplitude of the peak grows as a function of the field strength. From Eq. (3.27) we see that the angle decreases for larger H_0 , thus the sublattice magnetizations become more and more collinear, increasing the spin current pumped from each sublattice magnetization.

Fig. 3.16 displays the spin current polarized in the z-direction for left circularly polarized applied field. We see only positive peaks occurring at the same frequency values as in Fig. 3.15, consistent with the analysis of the magnetization dynamics. However, the amplitude of the peaks are 10^2 and 10^3 orders of magnitude lower than in Fig. 3.15. The spin current amplitude also decreases for increasing H_0 . This suggests that the more collinear the sublattice magnetizations become, the less motion is excited by the applied field.

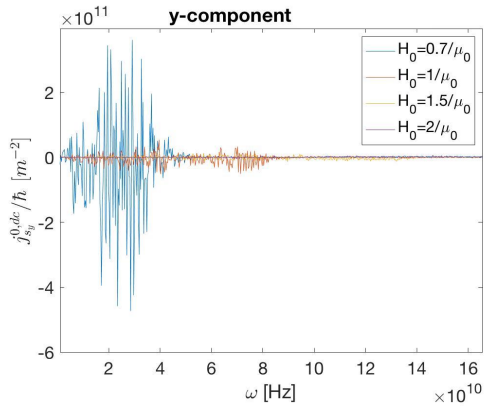
The spin current polarized in the z-direction for linearly polarized applied field is plotted in Fig. 3.17. From the figure it is clear that only the plus mode is excited, however the amplitude of the peaks have been lower. Comparing with the equivalent peaks in Fig. 3.15 we see that the amplitude is smaller for each H_0 and that the amount the amplitude has decreased is directly related to the equivalent peaks in Fig. 3.16 (this is best observed for $H_0 = 0.7/\mu_0$). A similar effect was observed for the minus mode in the bixial case. In light of this, an explanation might be that the precession of the magnetization is not circular, but rather elliptical. A more detailed analysis of the precessional mode of the magnetizations is required to explain the origin of this effect.

Fig. 3.18 shows the spin current polarized in the y-direction for different values of the cross-sublattice spin mixing conductance. $H_0 = 1/\mu_0$ has been employed and the polarization of the oscillating field is linear. Adding the cross-sublattice contributions has no effect on the dc spin current with this polarization, demonstrating that this component is truly zero.

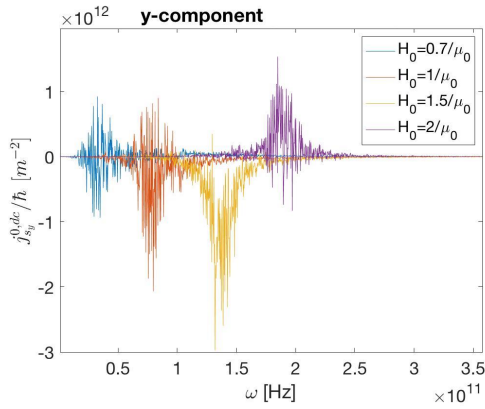
Similar to the collinear cases the spin current is reduced by the cross-sublattice spin pumping contributions, as seen in Fig. 3.19. Here the spin current with polarization in the z-direction is plotted for different g_{AB} for linearly polarized applied field. The parameters are the same as for the y-polarized spin current.



(a)



(b)



(c)

Figure 3.14: The dc spin current polarized in the y-direction, for the non-collinear AFM system, for different values of the static applied field, H_0 and different modes of the ac-field. In a) (plus mode) and b) (minus mode) only one mode is used. In c) a linearly polarized field is employed.

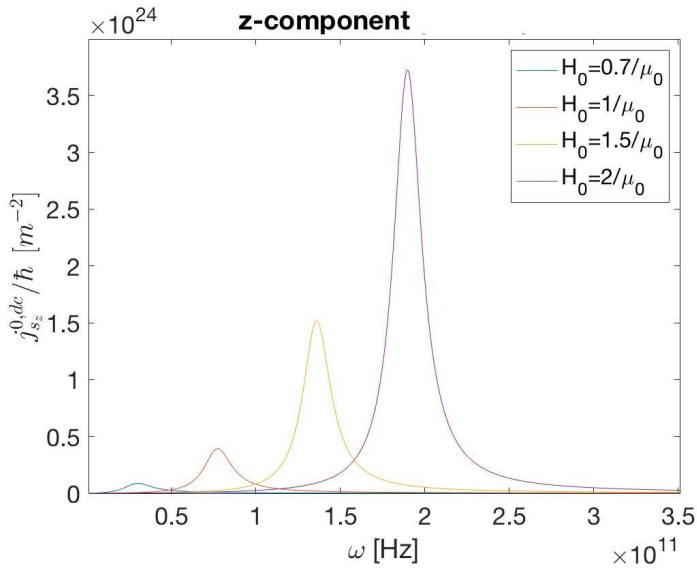


Figure 3.15: The dc spin current polarized in the z-direction, for the non-collinear AFM system, for different values of the static applied field, H_0 . A right circularly polarized applied field has been employed.

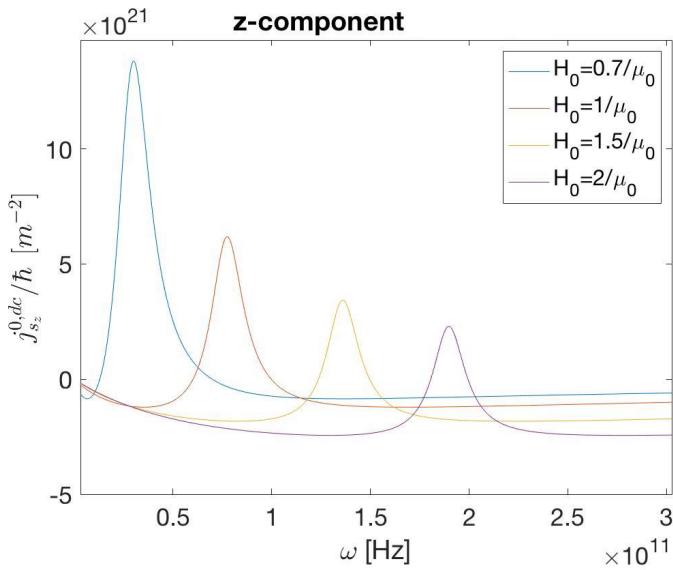


Figure 3.16: The dc spin current polarized in the z-direction, for the non-collinear AFM system, for different values of the static applied field, H_0 . A left circularly polarized applied field has been employed

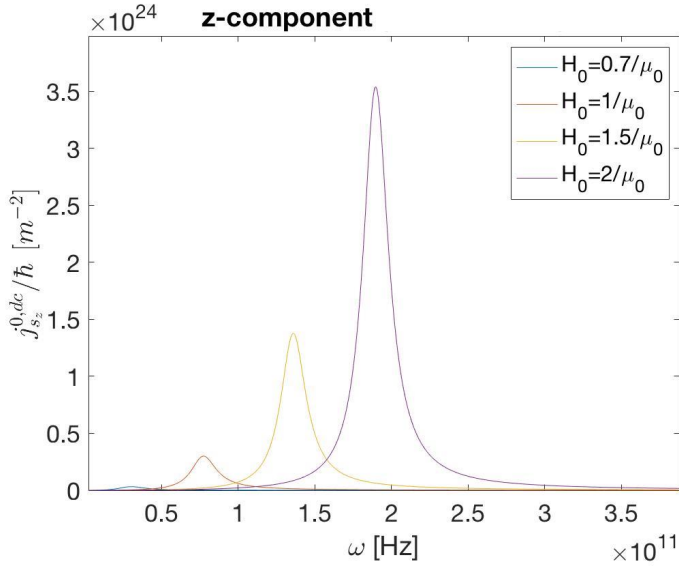


Figure 3.17: The dc spin current polarized in the z-direction, for the non-collinear AFM system, for different values of the static applied field, H_0 . A linearly polarized applied field has been employed

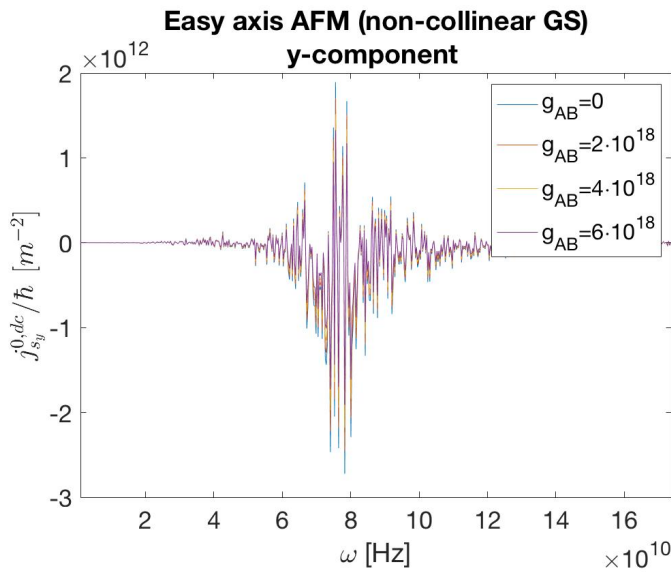


Figure 3.18: The dc spin current polarized in the y-direction, for the non-collinear AFM system, for different values of the cross-sublattice spin mixing conductance, g_{AB} . A linearly polarized applied field has been employed

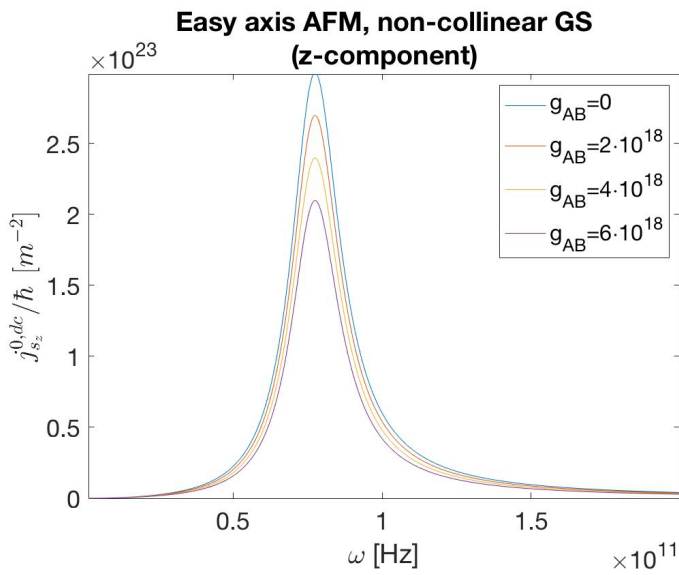


Figure 3.19: The dc spin current polarized in the z-direction, for the non-collinear AFM system, for different values of the cross-sublattice spin mixing conductance, g_{AB} . A linearly polarized applied field has been employed

Conclusion

4.1 Summery and concluding remarks

In this thesis the effect of cross-sublattice spin pumping on the dc spin pumping current, and whether it can be detected experimentally, for an antiferromagnetic/normal metal bilayer has been investigated and discussed. A total of three different AFM-systems were used for the antiferromagnetic layer, where two were in a collinear ground state and one was in a non-collinear ground state. The solution to the Landau-Lifshitz-Gilbert-equations of motion for the three systems, in addition to an analytic expression for the dc spin pumping current and induced ISHE-voltage for the two types of ground states, were presented. The solution to the equations of motion, together with the analytic expression for the dc spin current, was used to calculate dc spin current numerically for different values of the applied field strength and the cross-sublattice spin mixing conductance.

The solution to the LLG-equations presented for the easy axis antiferromagnet in collinear ground state is in excellent agreement with the literature. A splitting of the plus and minus modes was found, where the two modes correspond to right and left circular precession of the sublattice magnetizations, respectively. The analytic expression for the dc spin current displayed a polarization only in the z-direction, consistent with previous work on AFM spin pumping. We observed that the two modes were decoupled in the expression for both the intra-sublattice and cross-sublattice terms, and that the two modes give oppositely polarized spin currents. The voltage can thus only be measured along the edges in the y-direction of the normal metal. The results from the numerical calculations showed positive and negative peaks for right circularly polarized and left circularly polarized oscillations of the applied field, consistent with the analysis of the magnetization dynamics.

Increasing the field strength decreases the spin current pumped from the magnet in the plus mode, while it increases for the minus mode. The cross-sublattice contributions to the spin pumping current was found to decrease the injected current from the magnet.

The solution to the LLG-equation for the biaxial AFM displayed a coupling of the two modes, giving elliptical precession of the magnetizations. By comparison to the results from the easy axis AFM we can conclude that it is on reasonable form. The plots for the dc spin current displays two peaks, one negative and one positive, for both polarizations of the applied field, consistent with the results of the magnetization dynamics. We also observed a hybridized mode of the sublattice magnetizations for $H_0 = 0$. The effect of adding the cross-sublattice terms were found to be the same as in the easy axis case.

For the easy axis AFM in a non-collinear ground state, only the plus mode was excited by both a right and left circularly polarized applied field, consistent with the literature. The analytic expression for the dc spin pumping current displayed a component polarized in the x-, y- and z-direction, where the x-component originated from the cross-sublattice contributions only. From the numerical calculations we found that the spin current polarized in the x- and y-direction are zero for this configuration. The cross-sublattice contributions to the dc spin current can therefore not be isolated and measure experimentally. For the spin current polarized in the z-direction, the plots displayed only positive peaks, consistent with the magnetization dynamics. The effect of adding the cross-sublattice terms were observed to be the same as for the collinear systems.

4.1.1 Outlook

Due to time-pressure, there was no time to investigate the systems for different parameter-values or applied fields subtending non-zero angles with the easy axis. Thus, this should be on the agenda for future work on cross-sublattice spin pumping from non-collinear magnets. There is also reasons to believe that using a ferrimagnet in a non-collinear ground state can provide more promising results than presented in this thesis, as the sublattice magnetizations have different gyromagnetic ratios and saturation magnetizations. Although, the spin current expression, for a magnet in a non-collinear ground state, obtained in this thesis is not applicable for non-collinear ferrimagnets, the same method can be used to obtain an equivalent expression for these types of magnets.

Bibliography

Ando, K., Takahashi, S., Ieda, J., Kajiwara, Y., Nakayama, H., Yoshino, T., Harii, K., Fujikawa, Y., Maekawa, S., Saitoh, E., May 2011. Inverse spin-hall effect induced by spin pumping in metallic system. *Journal of Applied Physics* 109.

URL <https://doi.org/>

Baibich, M. N., Broto, J. M., Fert, A., Van Dau, F. N., Petroff, F., Etienne, P., Creuzet, G., Friederich, A., Chazelas, J., Nov 1988. Giant magnetoresistance of (001)fe/(001)cr magnetic superlattices. *Phys. Rev. Lett.* 61, 2472–2475.

URL <https://link.aps.org/doi/10.1103/PhysRevLett.61.2472>

Berry, M., Mar 1984. Quantal phase factors accompanying adiabatic changes. *Mathematical, Physical and Engineering Science* 5.

URL <https://doi.org/10.1098/rspa.1984.0023>

Binasch, G., Grünberg, P., Saurenbach, F., Zinn, W., Mar 1989. Enhanced magnetoresistance in layered magnetic structures with antiferromagnetic interlayer exchange. *Phys. Rev. B* 39, 4828–4830.

URL <https://link.aps.org/doi/10.1103/PhysRevB.39.4828>

Blundel, S., 2001. *Magnetism in condensed matter*. Oxford University press.

Brataas, A., Tserkovnyak, Y., Bauer, G. E. W., Halperin, B. I., Aug 2002. Spin battery operated by ferromagnetic resonance. *Phys. Rev. B* 66, 060404.

URL <https://link.aps.org/doi/10.1103/PhysRevB.66.060404>

Brown, W. J., 1960. Single-domain particles : New uses of old theorems. *American Journal of Physics* 28 (6), 542–551.

Bruus, H., Flensberg, K., 2002. Introduction to Many-body quantum theory in condensed matter physics. Oersted Laboratory, Niels Bohr Institute.

Cheng, R., Xiao, J., Niu, Q., Brataas, A., Jul 2014. Spin pumping and spin-transfer torques in antiferromagnets. Phys. Rev. Lett. 113, 057601.

URL <https://link.aps.org/doi/10.1103/PhysRevLett.113.057601>

Chikazumi, S., 1997. Physics of ferromagnetism. Oxford University Press Inc.

Coey, J., 2009. Magnetism and Magnetic materials. Cambridge Press.

Costache, M. V., Sladkov, M., Watts, S. M., van der Wal, C. H., van Wees, B. J., Nov 2006. Electrical detection of spin pumping due to the precessing magnetization of a single ferromagnet. Phys. Rev. Lett. 97, 216603.

URL <https://link.aps.org/doi/10.1103/PhysRevLett.97.216603>

Costache, M. V., Watts, S. M., van der Wal, C. H., van Wees, B. J., Aug 2008. Electrical detection of spin pumping: dc voltage generated by ferromagnetic resonance at ferromagnet/nonmagnet contact. Phys. Rev. B 78, 064423.

URL <https://link.aps.org/doi/10.1103/PhysRevB.78.064423>

Dieny, B., Goldfarb, R., Lee, K., Nov 2016. Introduction to magnetic random-access memory. Wiley.

Dirac, P., Howard, F., Oct 1926. On the theory of quantum mechanics. Proc. R. Soc. Lond. A 112, 661–677.

Dyakonov, M., Khaetskii, A., 2008. Spin Physics in Semiconductors, 1st Edition. Vol. 157. Springer-Verlag Berlin Heidelberg.

Gilbert, T., 2004. A phenomenological theory of damping in ferromagnetic materials. IEEE Transactions on Magnetics 40 (6), 3443–3449.

Gulbrandsen, S., Brataas, A., Oct 2017. Spin transfer and spin pumping in disordered normal metal-antiferromagneticinsulator systems.

URL <https://arxiv.org/pdf/1710.10250.pdf>

Gurevich, A. G., Melkov, G. A., 1996. Magnetization oscillations and waves. CRC Press, Inc.

-
- Haney, P. M., MacDonald, A. H., May 2008. Current-induced torques due to compensated antiferromagnets. *Phys. Rev. Lett.* 100, 196801.
URL <https://link.aps.org/doi/10.1103/PhysRevLett.100.196801>
- Heisenberg, W., Jun 1926. Mehrkörperproblem und resonanz in der quantenmechanik. *Zeitschrift für Physik* 38, 411–426.
- Hemmer, P., 2005. *Kvantemekanikk*. Tapir akademisk forlag.
- Jia, X., Liu, K., Xia, K., Bauer, G. E. W., Sep 2011. Spin transfer torque in magnetic insulators. *EPL* 96, 17005.
URL <https://doi.org/10.1209/0295-5075/96/17005>
- Johansen, O., Brataas, A., Jun 2017. Spin pumping and inverse spin hall voltages from dynamical antiferromagnets. *Phys. Rev. B* 95, 220408.
URL <https://link.aps.org/doi/10.1103/PhysRevB.95.220408>
- Johansen, O., Skarsvåg, H., Brataas, A., Feb 2018. Spin-transfer antiferromagnetic resonance. *Phys. Rev. B* 97, 054423.
URL <https://link.aps.org/doi/10.1103/PhysRevB.97.054423>
- Joshi, V., May 2016. Spintronics: A contemporary review of emerging electronics devices. *Engineering Science and Technology, an International Journal* 19, 1503–1513.
URL <https://doi.org/10.1016/j.jestch.2016.05.002>
- Kamra, A., Jan 2015. Coupled spin, elastic charge dynamics in magnetic nanostructures. Technische Universiteit Delft PhD.
- Kamra, A., Agrawal, U., Belzig, W., Jul 2017. Noninteger-spin magnonic excitations in untextured magnets. *Phys. Rev. B* 96, 020411.
URL <https://link.aps.org/doi/10.1103/PhysRevB.96.020411>
- Kamra, A., Belzig, W., Nov 2017. Spin pumping and shot noise in ferrimagnets: Bridging ferro- and antiferromagnets. *Phys. Rev. Lett.* 119, 197201.
URL <https://link.aps.org/doi/10.1103/PhysRevLett.119.197201>
- Kamra, A., Troncoso, R., Belzig, W., Brataas, A., Nov 2018. Gilbert damping phenomenology for two-sublattice magnets. *Phys. Rev. B* 98, 184402.
URL <https://link.aps.org/doi/10.1103/PhysRevB.98.184402>
-

-
- Keffer, F., Kittel, C., Jan 1952. Theory of antiferromagnetic resonance. *Phys. Rev.* 85, 329–337.
URL <https://link.aps.org/doi/10.1103/PhysRev.85.329>
- Kim, T., Park, K., Leiner, J., Park, J., Mar 2018. Hybridization and decay of magnetic excitations in two-dimensional triangular lattice antiferromagnets.
URL [arXiv:1810.00498](https://arxiv.org/abs/1810.00498) [cond-mat.str-el]
- Kimel, A., Kirilyuk, A., Usachev, A., P. V., Balbashov, A., Rasing, T., May 2005. Ultrafast non-thermal control of magnetization by instantaneous photomagnetic pulses. *Nature* 435, 655–657.
URL <https://doi.org/10.1038/nature03564>
- Liensberger, L., Kamra, A., Maier-Flaig, H., Geprags, S., Erb, A., Goennenwein, S.T.B., Belzig, W., Huebl, H., Weiler, M., Mar 2019. Exchange-enhanced ultrastrong magnon-magnon coupling in uncompensated ferrimagnet.
URL <https://arxiv.org/pdf/1903.04330.pdf>
- Liu, Q., Yuan, H. Y., Xia, K., Yuan, Z., Nov 2017. Mode-dependent damping in metallic antiferromagnets due to intersublattice spin pumping. *Phys. Rev. Materials* 1, 061401.
URL <https://link.aps.org/doi/10.1103/PhysRevMaterials.1.061401>
- Manenkov, A. A., Orbach, R., 1966. *Spin-Lattice Relaxation in Ionic Solids*. Harper Row.
- Martí, X., Park, B. G., Wunderlich, J., Reichlová, H., Kurosaki, Y., Yamada, M., Yamamoto, H., Nishide, A., Hayakawa, J., Takahashi, H., Jungwirth, T., Jan 2012. Electrical measurement of antiferromagnetic moments in exchange-coupled IrMn/NiFe stacks. *Phys. Rev. Lett.* 108, 017201.
URL <https://link.aps.org/doi/10.1103/PhysRevLett.108.017201>
- Mizukami, S., A. Y., Miyazaki, T., 2001. Ferromagnetic resonance linewidth for nm/80nm/nm films (nm=cu, ta, pd and pt). *Journal of Magnetism and Magnetic Materials* 226-230, 1640–1642.
- Mosendz, O., Vlamincik, V., Pearson, J. E., Fradin, F. Y., Bauer, G. E. W., Bader, S. D., Hoffmann, A., Dec 2010. Detection and quantification of inverse spin hall effect from spin pumping in permalloy/normal metal bilayers. *Phys. Rev. B* 82, 214403.
URL <https://link.aps.org/doi/10.1103/PhysRevB.82.214403>
-

Muller, M., Aug 2017. Finite size effects of the anisotropic magnetoresistance. Technische Universität München PhD.

Oogane, M., Wakitani, T., Yakata, S., Yilgin, R., Ando, Y., Sakuma, A., Miyazaki, T., May 2006. Magnetic damping in ferromagnetic thin films. Japanese Journal of Applied Physics 45, 3889–3891.

Saitoh, E., U. M., Miyajima, H., Mar 2006. Detection and quantification of inverse spin hall effect from spin pumping in permalloy/normal metal bilayers. Appl. Phys. Lett. 88, 182509.

URL <https://doi.org/10.1063/1.2199473>

Sankey, J., Cui, Y., Sun, J., Slonczewski, J., Buhrman, R., Ralph, D., Nov 2008. Measurement of the spin-transfer-torque vector in magnetic tunnel junctions. Nat.Phys, 67–71.

URL <https://doi.org/10.1038/nphys783>

Satoh, T., Cho, S.-J., Iida, R., Shimura, T., Kuroda, K., Ueda, H., Ueda, Y., Ivanov, B. A., Nori, F., Fiebig, M., Aug 2010. Spin oscillations in antiferromagnetic nio triggered by circularly polarized light. Phys. Rev. Lett. 105, 077402.

URL <https://link.aps.org/doi/10.1103/PhysRevLett.105.077402>

Shen, S., Oct 2008. Spintronics and spin current. AAPPS Bulletin 18, 29–37.

URL <http://web.hku.hk/~sshenn/index.files/publication/publication-pdf/pdf2008/Shen-AAPPS08.pdf>

Stancil, D., Prabhakar, A., 2009. Spin waves. Springer Science Business Media, LLC.

Swaving, A. C., Duine, R. A., Feb 2011. Current-induced torques in continuous antiferromagnetic textures. Phys. Rev. B 83, 054428.

URL <https://link.aps.org/doi/10.1103/PhysRevB.83.054428>

Tserkovnyak, Y., B. A. B. G., Halperin, B., Dec 2005. Nonlocal magnetization dynamics in ferromagnetic heterostructures. Rev. Mod. Phys. 77, 1375–1421.

URL <https://link.aps.org/doi/10.1103/RevModPhys.77.1375>

Tserkovnyak, Y., Brataas, A., Bauer, G., Halperin, B., Feb 2002a. Enhanced gilbert damping in thin ferromagnetic films. Phys. Rev. Lett. 88, 117601.

URL <https://link.aps.org/doi/10.1103/PhysRevLett.88.117601>

-
- Tserkovnyak, Y., Brataas, A., Bauer, G. E. W., Dec 2002b. Spin pumping and magnetization dynamics in metallic multilayers. *Phys. Rev. B* 66, 224403.
URL <https://link.aps.org/doi/10.1103/PhysRevB.66.224403>
- Tveten, E., Apr 2016. Manipulating spins in antiferromagnets with external forces. Norwegian University of Science and Technology PhD.
- Urban, R., Woltersdorf, G., Heinrich, B., Nov 2001. Gilbert damping in single and multi-layer ultrathin films: Role of interfaces in nonlocal spin dynamics. *Phys. Rev. Lett.* 87, 217204.
URL <https://link.aps.org/doi/10.1103/PhysRevLett.87.217204>
- Vacus, O., Vukadinovic, N., April 2005. Dynamic susceptibility computations for thin magnetic films. *Journal of Computational and Applied Mathematics* 175, 263–281.
- Wang, Y. Y., Song, C., Cui, B., Wang, G. Y., Zeng, F., Pan, F., Sep 2012. Room-temperature perpendicular exchange coupling and tunneling anisotropic magnetoresistance in an antiferromagnet-based tunnel junction. *Phys. Rev. Lett.* 109, 137201.
URL <https://link.aps.org/doi/10.1103/PhysRevLett.109.137201>
- Wegrow, J.-E., Cironei, M.-C., 2012. Magnetization dynamics, gyromagnetic relation, and inertial effects. *American Journal of Physics* 80 (7), 607–618.
- Wei, D., Obstaum, M., Ribow, M., B. C., Woltersdorf, G., Apr 2014. Spin hall voltages from a.c. and d.c. spin currents. *Nature Communications* 392.
URL <https://doi.org/10.1038/ncomms4768>
- Weiss, P., 1907. L'hypothèse du champ moléculaire et la propriété ferromagnétique. *J. Phys. Theor. Appl.* 6, 661–690.
- Wienholdt, S., Hinzke, D., Nowak, U., Jun 2012. Thz switching of antiferromagnets and ferrimagnets. *Phys. Rev. Lett.* 108, 247207.
URL <https://link.aps.org/doi/10.1103/PhysRevLett.108.247207>
- Xu, Y., Wang, S., Xia, K., Jun 2008. Spin-transfer torques in antiferromagnetic metals from first principles. *Phys. Rev. Lett.* 100, 226602.
URL <https://link.aps.org/doi/10.1103/PhysRevLett.100.226602>

Yan, P., Kamra, A., Cao, Y., Bauer, G., Oct 2013. Angular and linear momentum of excited ferromagnets. Phys. Rev. B 88, 144413.

URL <https://link.aps.org/doi/10.1103/PhysRevB.88.144413>

Appendix

4.2 Equation of motion of the magnetization from Lagrangian formalism

Considering the rotating magnetization as a symmetric spinning top with principle moment of inertia $I_1 = I_2 = 0$ and $I_3 > 0$, the Lagrangian density of the magnetization can be written (Brown, 1960):

$$\mathcal{L} = \frac{M_0}{\gamma} \dot{\phi} \cos \theta - w, \quad \dot{\phi} = \frac{d\phi}{dt} \quad (4.1)$$

in spherical coordinates, where w is the free energy density functional of the magnetization, $\theta, \dot{\theta}, \phi, \dot{\phi}$ the system generalized coordinates and velocities, M_0 is the saturation magnetization and γ is the gyromagnetic ratio. The first term is the kinetic energy of the system. This form is known as the spin Berry phase in quantum mechanics (Berry, 1984), which is also important in classical mechanics since it leads to the equation of motion characteristic to the angular momentum. The free energy density functional constitutes the potential energy of the system. The motion of the magnetization obeys the Euler-Lagrange equations:

$$\frac{d}{dt} \frac{\partial \mathcal{L}}{\partial \dot{\theta}} - \frac{\partial \mathcal{L}}{\partial \theta} = 0 \quad (4.2a)$$

$$\frac{d}{dt} \frac{\partial \mathcal{L}}{\partial \dot{\phi}} - \frac{\partial \mathcal{L}}{\partial \phi} = 0. \quad (4.2b)$$

Substituting (4.1) in these equations yields:

$$-\frac{M_0}{\gamma} \dot{\theta} \sin \theta = -\frac{\partial w}{\partial \phi} \quad (4.3a)$$

$$\frac{M_0}{\gamma} \dot{\phi} \sin \theta = -\frac{\partial w}{\partial \theta}, \quad (4.3b)$$

which are equivalent to the vector equation (2.23). The vector equation for the magnetization can be derived from (4.3a) and (4.3b) by using that the magnetization vector in spherical coordinates is written $\mathbf{M} = M_S(\sin \theta \cos \phi, \sin \theta \sin \phi, \cos \theta)$ and that for any vector of constant modulus (constant length) carried with the rotating body:

$$\frac{d\mathbf{M}}{dt} = \boldsymbol{\Omega} \times \mathbf{M}, \quad (4.4)$$

where $\boldsymbol{\Omega}$ is the angular velocity of the spinning top in the fixed body frame (Wegrow and Cironei, 2012). Inserting (4.4) in the equations above leads to:

$$\dot{\mathbf{M}} = -\gamma \mathbf{M} \times \mu_0 \mathbf{H}_{eff}, \quad (4.5)$$

for the magnetization $\mathbf{M} = \mathbf{M}(\mathbf{r})$. The effective field \mathbf{H}_{eff} , is related to the free energy density by the functional derivative:

$$\mu_0 \mathbf{H}_{eff} = -\frac{\delta w}{\delta \mathbf{M}}. \quad (4.6)$$

Damping can be introduced through the Rayleigh dissipation functional:

$$\mathcal{R} = \frac{\alpha}{2\gamma M_0} \int_V \frac{d\mathbf{M}}{dt} \cdot \frac{d\mathbf{M}}{dt} d^3r \quad (4.7)$$

$$= \frac{\alpha M_0}{2\gamma} \left(\dot{\theta}^2 + \dot{\phi}^2 \sin^2 \theta \right), \quad (4.8)$$

Adjusting the Euler-Lagrange's equations for the functional we have:

$$\frac{d}{dt} \frac{\partial \mathcal{L}}{\partial \dot{\theta}} - \frac{\partial \mathcal{L}}{\partial \theta} + \frac{\partial \mathcal{R}}{\partial \dot{\theta}} = 0 \quad (4.9a)$$

$$\frac{d}{dt} \frac{\partial \mathcal{L}}{\partial \dot{\phi}} - \frac{\partial \mathcal{L}}{\partial \phi} + \frac{\partial \mathcal{R}}{\partial \dot{\phi}} = 0. \quad (4.9b)$$

By using (4.4) in the above equations and (4.7), we obtain the damping expression introduced by Gilbert. The equations of motion including damping is then written:

$$\dot{\mathbf{M}} = -\gamma \mathbf{M} \times \mu_0 \mathbf{H}_{eff} + \frac{\alpha}{M_0} \mathbf{M} \times \dot{\mathbf{M}}. \quad (4.10)$$

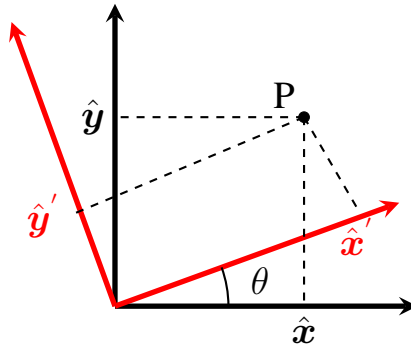


Figure 4.1: An xy -Cartesian coordinate system rotated through an angle θ to an $x'y'$ -Cartesian coordinate system

4.3 Coordinate transformations

The coordinate transformations between different coordinates is done by mapping from one coordinate system to another. Consider two coordinate systems xy and $x'y'$ as shown in Fig. 4.1. With the origin kept fixed, the mapping from xy to $x'y'$ is done by rotation of the axes through the angle θ . Consider a point P given by (x, y) in the xy -coordinates and (x', y') in the $x'y'$ -coordinates. In polar coordinates, the coordinates of P in the xy -frame is:

$$x = r \cos \alpha \tag{4.11}$$

$$y = r \sin \alpha. \tag{4.12}$$

Since the $x'y'$ coordinate system is rotated counterclockwise by the angle θ with respect to the other, the coordinates in this frame are:

$$x' = r \cos \alpha - \theta = r \cos \alpha \cos \theta + r \sin \alpha \sin \theta \tag{4.13}$$

$$y' = r \sin \alpha - \theta = r \sin \alpha \cos \theta - r \cos \alpha \sin \theta. \tag{4.14}$$

Substituting Eqs. (4.11) and (4.12) into these equations we obtain:

$$x' = r \cos(\alpha - \theta) = x \cos \theta + y \sin \theta \quad (4.15)$$

$$y' = r \sin(\alpha - \theta) = y \cos \theta - x \sin \theta. \quad (4.16)$$

Employing this to the coordinate systems in Fig. 3.12 yields:

$$(\hat{y}, \hat{z}) \rightarrow (\hat{y}', \hat{z}'): \hat{z} = \hat{z}' \cos \theta - \hat{y}' \sin \theta, \quad \hat{y} = \hat{y}' \cos \theta + \hat{z}' \sin \theta, \quad (4.17)$$

$$(\hat{y}', \hat{z}') \rightarrow (\hat{y}, \hat{z}): \hat{z}' = \hat{z} \cos \theta + \hat{y} \sin \theta, \quad \hat{y}' = \hat{y} \cos \theta - \hat{z} \sin \theta, \quad (4.18)$$

$$(\hat{y}'', \hat{z}'') \rightarrow (\hat{y}', \hat{z}'): \hat{z}'' = -\hat{z}' \cos 2\theta + \hat{y}' \sin 2\theta, \quad \hat{y}'' = -\hat{y}' \cos 2\theta - \hat{z}' \sin 2\theta, \quad (4.19)$$

$$(\hat{y}', \hat{z}') \rightarrow (\hat{y}'', \hat{z}''): \hat{z}' = -\hat{z}'' \cos 2\theta - \hat{y}'' \sin 2\theta, \quad \hat{y}' = -\hat{y}'' \cos 2\theta + \hat{z}'' \sin 2\theta, \quad (4.20)$$

$$(\hat{y}, \hat{z}) \rightarrow (\hat{y}'', \hat{z}''): \hat{z} = -\hat{z}'' \cos \theta - \hat{y}'' \sin \theta, \quad \hat{y} = -\hat{y}'' \cos \theta + \hat{z}'' \sin \theta \quad (4.21)$$

$$(\hat{y}'', \hat{z}'') \rightarrow (\hat{y}, \hat{z}): \hat{z}'' = -\hat{z} \cos \theta + \hat{y} \sin \theta, \quad \hat{y}'' = -\hat{y} \cos \theta - \hat{z} \sin \theta. \quad (4.22)$$

4.4 Numerics

Here, the numerics behind the results are elucidated. The actual codes are also presented below.

The codes work as follows:

1. First, the value of the coefficients describing the system are defined:

- Saturation magnetization M_0
- Gilbert damping parameters α_{ij}
- Anisotropy parameters K_x, K_z
- Exchange integral J
- Spin mixing conductances g_{ij}
- Values of the applied field components H_0, h_{\pm}
- Gyromagnetic ratio γ

2. Then, a set of vectors are defined:

-
- A row vector, named omega, with frequency values from 0 to a maximum frequency is created. This vector contains the frequency values, ω , of the applied field. The maximum frequency is chosen such that the resonance frequency of the magnet is included in the range, preferably in the middle of the set of frequency values.
 - A set of row vector of the same length as omega, representing the magnetization amplitudes $\hat{m}_{A\pm}$ and $\hat{m}_{B\pm}$ are defined.
 - A row vector of the same length as omega, representing the spin current, $j_{s_i}^{0,dc}$, is defined. Here, the subscript i denotes the polarization component of the spin current that is to be calculated.
3. To calculate the magnetization amplitudes and the spin current, a for-loop with iterator, m , running from 1 to l (where l is the length of the frequency vector) is made. Inside the for-loop we have:
- The inverse susceptibility tensor, $\hat{\chi}^{-1}(\omega)$, is defined, where the value of ω is $\omega(m)$ for each iteration.
 - The susceptibility, $\hat{\chi}(\omega)$, is calculated by taking the inverse of $\hat{\chi}^{-1}(\omega)$ using the built in function `inv()`.
 - The m th element of the magnetization components are calculated, using Eq. (3.37)/(3.23), and stored in the vectors.
 - These values are then used to calculate the m th element of the spin current vector, using Eq. (3.16)/(3.58)/(3.60)/(3.61), which is then stored in the vector.
4. The spin pumping current is then plot against the frequency values using the built in function `plot()`.

4.4.1 Codes

The codes used to numerically calculate and plot dc spin pumping current are shown below. Note, that the code for the easy axis AFM in the collinear ground state is different from that described above. This is because the analytic solution to the LLG-equations are easily obtainable, and could therefore be implemented directly into the code to calculate the desired spin current.

Easy axis AFM in collinear GS

```
%Constants
```

```

alphaAA=0.010; %Intra-sublattice damping parameter on...
sublattice A
alphaBB=0.010; %Intra-sublattice damping parameter on...
sublattice B
alphaAB=0.001; %Cross-sublattice damping parameter on...
sublattice A
alphaBA=alphaAB; %Cross-sublattice damping parameter on...
sublattice B

mu0=12.57*10^(-7); %Magnetic permeability
H0=0.3/mu0; %Field strength of the static part of the applied
magnetic field
h_plus=0.005/mu0; %Field strength of the oscillating part of
the applied field (right hand circularly polarized rotation)
h_minus=0.005/mu0; %Field strength of the oscillating part of
the applied field (left hand circularly polarized rotation

gamma=10^11; %gyromagnetic ratio
gAA=2*10^(19); %Intra-sublattice spin mixing conductance...
(sublattice A)
gBB=2*10^(19); %Intra-sublattice spin mixing conductance...
(sublattice B)
gAB=6*10^(18); %Cross-sublattice spin mixing conductance...
(sublattice A
and sublattice B)

M0=10^5; %Saturation magnetization
J=10^-4; %Exchange integral
Kz=10^(-7); %Easy axis anisotropy constant

omegaA=gamma*(mu0*H0+2*Kz*M0+J*M0);
omegaB=gamma*(2*Kz*M0+J*M0-mu0*H0);

%Vectors
omega=linspace(1e9,3e11,3001); %Frequency-values of the...
oscillating field

```

```

I=zeros(1,3001); %dc spin pumping current
D_plus=zeros(1,3001); %Determinant of the inverse...
susceptibility for upper sign
D_minus=zeros(1,3001); %Determinant of the inverse...
susceptibility for lower sign
mA_plus=zeros(1,3001); %Unit vector magnetzation on...
sublattice A
(plus mode)
mB_plus=zeros(1,3001); %Unit vector magnetzation on...
sublattice B
(plus mode)
mA_minus=zeros(1,3001); %Unit vector magnetzation on...
sublattice A
(minus mode)
mB_minus=zeros(1,3001); %Unit vector magnetzation on...
sublattice B
(minus mode)

%Calculating the magnetization amplitudes and the
dc spin current

for m=1:3001
    D_plus(m)=- (omega(m)-omegaA-1j*alphaAA*omega(m))*...
    (omega(m)+omegaB+1j*alphaBB*omega(m)) - (gamma*J*M0+...
    1j*alphaAB*omega(m))* (gamma*J*M0+1j*alphaBA*omega(m));
    D_minus(m)=- (-omega(m)-omegaA-1j*alphaAA*omega(m))*...
    (-omega(m)+omegaB+1j*alphaBB*omega(m)) - (gamma*J*M0+...
    1j*alphaAB*omega(m))* (gamma*J*M0+1j*alphaBA*omega(m));
    mA_plus(m)=(gamma*mu0*h_plus)*(omega(m)+omegaB+...
    1j*alphaBB*omega(m) - (gamma*J*M0+1j*alphaAB*omega(m)))...
    /D_plus(m);
    mB_plus(m)=(gamma*mu0*h_plus)*(-omega(m)-omegaA-...
    1j*alphaAA*omega(m)) - (gamma*J*M0+1j*alphaBA*omega(m)))...
    /D_plus(m);
    mA_minus(m)=(gamma*mu0*h_minus)*(-omega(m)+omegaB+...
    1j*alphaBB*omega(m) - (gamma*J*M0+1j*alphaAB*omega(m)))...

```

```

/D_minus(m);
mB_minus(m)=(gamma*mu0*h_minus)*(-(-omega(m)-omegaA-...
1j*alphaAA*omega(m))-(gamma*J*M0+1j*alphaBA*omega(m)))...
/D_minus(m);
I(m)=(omega(m)/(16*pi))*(gAA*(abs(mA_plus(m)))^2-...
(abs(mA_minus(m)))^2)+gBB*(abs(mB_plus(m)))^2-...
(abs(mB_minus(m)))^2)+2*gAB*real(conj(mA_plus(m))*...
mB_plus(m)-conj(mA_minus(m))*mB_minus(m)));
end

```

```

%Plotting the dc spin current against the frequency
plot(omega,I,'LineWidth',1);
xlabel('\omega [Hz]');
ylabel('$j^{0,dc}_{s}/\hbar \: \: [m^{-2}]$', 'interpreter',...
'latex');
set(findall(gcf,'-property','FontSize'),'FontSize',25)
set(gcf,'color','w');
set(gca,'FontSize',18);
hold on;

```

Biaxial AFM in collinear GS

```

%Constants
alphaAA=0.010; %Intra-sublattice damping parameter on
sublattice A
alphaBB=0.010; %Intra-sublattice damping parameter on
sublattice B
alphaAB=0.001; %Cross-sublattice damping parameter on
sublattice A
alphaBA=alphaAB; %Cross-sublattice damping parameter on
sublattice B

mu0=12.57*10^(-7); %Magnetic permeability
H0=0.3/mu0; %Field strength of the static part of...
the applied magnetic field
h_plus=0.005/mu0; %Field strength of the oscillating part...
of the applied field(right hand circularly polarized rotation)

```

`h_minus=0.005/mu0; %Field strength of the oscillating part...
of the applied field(left hand circularly polarized rotation)`

`gamma=10^11; %gyromagnetic ratio
gAA=2*10^(19);%Intra-sublattice spin mixing conductance
(sublattice A)
gBB=2*10^(19);%Intra-sublattice spin mixing conductance
(sublattice B)
gAB=6*10^(18);%Cross-sublattice spin mixing conductance...
(sublattice A and sublattice B)`

`M0=10^5; %Saturation magnetization
J=10^-4; %Exchange integral
Kz=10^(-7); %Easy axis anisotropy constant
Kx=10^(-7); %Hard axis anisotropy constant`

`omegaA=gamma*(mu0*H0+2*Kj*M0+J*M0);
omegaB=gamma*(2*Kj*M0+J*M0-mu0*H0);`

`%Defining vectors`

`omega=linspace(1e9,4e11,2001); % Frequency of the applied...
field`

`I=zeros(1,2001); %dc spin pumping current`

`mA_plus=zeros(1,2001); %Unit vector magnetization on...
sublattice A (plus mode)`

`mB_plus=zeros(1,2001); %Unit vector magnetization on...
sublattice B (plus mode)`

`mA_minus=zeros(1,2001); %Unit vector magnetization on...
sublattice A (minus mode)`

`mB_minus=zeros(1,2001); %Unit vector magnetization on...
sublattice B (minus mode)`

`%Calculating the magnetization amplitudes and the...`

dc spin current

```
for m=1:2001
    H=[-(omega(m)-omegaA-1j*alphaAA*omega(m)-2*gamma*Kx*M0)...
        gamma*J*M0+1j*alphaAB*omega(m) 2*gamma*Kx*M0 0;...
        gamma*J*M0+1j*alphaBA*omega(m) (omega(m)+omegaB+...
        1j*alphaBB*omega(m)+2*gamma*Kx*M0) 0 2*gamma*Kx*M0;...
        2*gamma*Kx*M0 0 -(-omega(m)-omegaA-1j*alphaAA*omega(m)-...
        2*gamma*Kx*M0) gamma*J*M0+1j*alphaAB*omega(m);...
        0 2*gamma*Kx*M0 gamma*J*M0+1j*alphaBA*omega(m) -omega(m)...
        +omegaB+1j*alphaBB*omega(m)+2*gamma*Kx*M0];
    M=inv(H);
    mA_plus(m)=gamma*mu0*(h_plus*M(1,1)+h_plus*M(1,2)+...
        h_minus*M(1,3)+h_minus*M(1,4));
    mB_plus(m)=gamma*mu0*(h_plus*M(2,1)+h_plus*M(2,2)+...
        h_minus*M(2,3)+h_minus*M(2,4));
    mA_minus(m)=gamma*mu0*(h_plus*M(3,1)+h_plus*M(3,2)+...
        h_minus*M(3,3)+h_minus*M(3,4));
    mB_minus(m)=gamma*mu0*(h_plus*M(4,1)+h_plus*M(4,2)+...
        h_minus*M(4,3)+h_minus*M(4,4));
    I(m)=(omega(m)/(16*pi))*(gAA*(abs(mA_plus(m)))^2-...
        (abs(mA_minus(m)))^2)+gBB*(abs(mB_plus(m)))^2-...
        (abs(mB_minus(m)))^2)+2*gAB*(real(conj(mA_plus(m))*...
        mB_plus(m))-real(conj(mA_minus(m))*mB_minus(m))));
end

%Plotting the dc spin current against the frequency
plot(omega,I);
xlabel('\omega [Hz]');
ylabel('$j^{0,dc}_{\{s\}}/\hbar \backslash:\backslash:[m^{-2}]$', 'interpreter',...
'latex');
set(findall(gcf,'-property','FontSize'),'FontSize',25)
set(gcf,'color','w');
set(gca,'FontSize',18);
hold on;
```

Easy axis AFM in non-collinear GS

x-component

```
%Defining constants
alphaAA=0.01;%Intra-sublattice damping parameter on...
sublattice A
alphaBB=0.01;%Intra-sublattice damping parameter on...
sublattice B
alphaAB=0.001;%Cross-sublattice damping parameter on...
sublattice A
alphaBA=alphaAB;%Cross-sublattice damping parameter on...
sublattice B

gAA=2*10^(19);%Intra-sublattice spin mixing conductance...
(sublattice A)
gBB=2*10^(19);%Intra-sublattice spin mixing conductance...
(sublattice B)
gAB=2*10^(18);%Cross-sublattice spin mixing conductance...
(sublattice A and sublattice B)

mu0=12.57*10^(-7);%Magnetic permeability
H0=0.7/mu0;%Field strength of the static part...
of the applied magnetic field
h_plus=0.005/mu0;%Field strength of the oscillating part...
of the applied field (right hand circularly polarized rotation)
h_minus=0.005/mu0;%Field strength of the oscillating part...
of the applied field (left hand circularly polarized rotation)

Kz=10^(-7);%Easy axis anisotropy constant
M0=10^5; %Saturation magnetization
gamma=10^11; %gyromagnetic ratio
wh=2*gamma*Kz*M0;
J=10^-4;%Exchange integral

theta=acos(mu0*H0/(2*J*M0)); %Angle subtended by the...
```

```

sublattice magnetization with respect to the easy axis
Theta=[1+cos(theta) 1-cos(theta);1-cos(theta)...
1+cos(theta); 1-cos(theta) 1+cos(theta);1+cos(theta) 1-cos(theta)];
h_circ=[gamma*mu0*h_plus/2; gamma*mu0*h_minus/2];

C=gamma*(2*Kz*M0*cos(2*theta)+mu0*H0*cos(theta)-...
J*M0*cos(2*theta));
D=gamma*(2*Kz*M0*cos(2*theta)-J*M0*cos(2*theta)+...
mu0*H0*cos(theta));

%Defining matrices and vectors
omega=linspace(1e9,6e11,2001); %Frequency of the...
oscillating applied field
mA_plus=zeros(1,2001);%Unit vector magnetzation on...
sublattice A (plus mode)
mB_plus=zeros(1,2001);%Unit vector magnetzation on...
sublattice B (plus mode)
mA_minus=zeros(1,2001);%Unit vector magnetzation on...
sublattice A (minus mode)
mB_minus=zeros(1,2001);%Unit vector magnetzation on...
sublattice B (minus mode)
Ix=zeros(1,2001);%dc spin pumping current...
polarized in the x-direction
prod=Theta*h_circ;

%Calculating the magnetization amplitudes and the...
dc spin current

for m=1:2001
    H=[-omega(m)+C+1j*alphaAA*omega(m)-(1/2)*wh*...
(sin(theta))^2 (gamma*J*M0/2+1j*alphaAB*omega(m)/2)*...
(1-cos(2*theta)) -(1/2)*wh*(sin(theta))^2 (gamma*J*M0/2+...
1j*alphaAB*omega(m)/2)*(1+cos(2*theta));(gamma*J*M0/2+...
1j*alphaBA*omega(m)/2)*(1-cos(2*theta)) omega(m)+D+...
1j*alphaBB*omega(m)-(1/2)*wh*(sin(theta))^2 ...

```

```

(gamma*J*M0/2+1j*alphaBA*omega(m)/2)*(1+cos(2*theta))...
-(1/2)*wh*(sin(theta))^2;-(1/2)*wh*(sin(theta))^2 ...
(gamma*J*M0/2+1j*alphaAB*omega(m)/2)*...
(1+cos(2*theta)) omega(m)+C+1j*alphaAA*omega(m)-...
(1/2)*wh*(sin(theta))^2 (gamma*J*M0/2+1j*alphaAB*omega(m)/2)*...
(1-cos(2*theta));(gamma*J*M0/2+1j*alphaAB*...
omega(m)/2)*(1+cos(2*theta)) -(1/2)*wh*(sin(theta))^2 ...
(gamma*J*M0/2+1j*alphaAB*omega(m)/2)*(1-cos(2*theta)) ...
-omega(m)+D+1j*alphaBB*omega(m)-(1/2)*wh*(sin(theta))^2];
M=inv(H);
mA_plus(m)=prod(1)*M(1,1)+prod(2)*M(1,2)+prod(3)*M(1,3)+...
prod(4)*M(1,4);
mB_plus(m)=prod(1)*M(2,1)+prod(2)*M(2,2)+prod(3)*M(2,3)+...
prod(4)*M(2,4);
mA_minus(m)=prod(1)*M(3,1)+prod(2)*M(3,2)+prod(3)*M(3,3)+...
prod(4)*M(3,4);
mB_minus(m)=prod(1)*M(4,1)+prod(2)*M(4,2)+prod(3)*M(4,3)+..
prod(4)*M(4,4);
Ix(m)=(omega(m)*gAB*sin(2*theta)/(8*pi))*...
imag(conj(mB_plus(m))*mA_plus(m)+conj(mB_minus(m))*...
mA_minus(m)-conj(mB_minus(m))*mA_plus(m)-conj(mB_plus(m))*mA_minus(m)
end

```

```

%Plotting the dc spin current against the frequency
plot(omega, Ix);
xlabel('\omega [Hz]');
ylabel('$j^{0,dc}_{s_x}/\hbar \: \: [m^{-2}]$', 'interpreter', ...
'latex');
set(findall(gcf, '-property', 'FontSize'), 'FontSize', 25)
set(gcf, 'color', 'w');
set(gca, 'FontSize', 18);
hold on;

```

y-component

```

%Defining constants

```

```

alphaAA=0.01;%Intra-sublattice damping parameter on...
sublattice A
alphaBB=0.01;%Intra-sublattice damping parameter on...
sublattice B
alphaAB=0.001;%Cross-sublattice damping parameter on...
sublattice A
alphaBA=alphaAB;%Cross-sublattice damping parameter on...
sublattice B

gAA=2*10^(19);%Intra-sublattice spin mixing conductance...
(sublattice A)
gBB=2*10^(19);%Intra-sublattice spin mixing conductance...
(sublattice B)
gAB=2*10^(18);%Cross-sublattice spin mixing conductance...
(sublattice A and sublattice B)

mu0=12.57*10^(-7);%Magnetic permeability
H0=0.7/mu0;%Field strength of the static part of...
the applied magnetic field
h_plus=0.005/mu0;%Field strength of the oscillating part of...
the applied field (right hand circularly polarized rotation)
h_minus=0.005/mu0;%Field strength of the oscillating part of...
the applied field (left hand circularly polarized rotation)

Kz=10^(-7);%Easy axis anisotropy constant
M0=10^5; %Saturation magnetization
gamma=10^11; %gyromagnetic ratio
wh=2*gamma*Kz*M0;
J=10^-4;%Exchange integral

theta=acos(mu0*H0/(2*J*M0)); %Angle subtended by the...
sublattice magnetization with respect to the easy axis
Theta=[1+cos(theta) 1-cos(theta);1-cos(theta) 1+cos(theta);...
1-cos(theta) 1+cos(theta);1+cos(theta) 1-cos(theta)];

```

```

h_circ=[gamma*mu0*h_plus/2; gamma*mu0*h_minus/2];

C=gamma*(2*Kz*M0*cos(2*theta)+mu0*H0*cos(theta)-J*M0*...
cos(2*theta));
D=gamma*(2*Kz*M0*cos(2*theta)-J*M0*cos(2*theta)+...
mu0*H0*cos(theta));

%Defining matrices and vectors
omega=linspace(1e9,6e11,2001); %Frequency of the...
oscillating applied field
mA_plus=zeros(1,2001);%Unit vector magnetization on...
sublattice A (plus mode)
mB_plus=zeros(1,2001);%Unit vector magnetization on...
sublattice B (plus mode)
mA_minus=zeros(1,2001);%Unit vector magnetization on...
sublattice A (minus mode)
mB_minus=zeros(1,2001);%Unit vector magnetization on...
sublattice B (minus mode)
Iy=zeros(1,2001);%dc spin pumping current...
polarized in the y-direction
prod=Theta*h_circ;

%Calculating the magnetization amplitudes and the ...
dc spin current

for m=1:2001
    H=[-omega(m)+C+1j*alphaAA*omega(m)-(1/2)*wh*...
(sin(theta))^2 (gamma*J*M0/2+1j*alphaAB*omega(m)/2)*...
(1-cos(2*theta)) -(1/2)*wh*(sin(theta))^2 (gamma*J*M0/2+...
1j*alphaAB*omega(m)/2)*(1+cos(2*theta));(gamma*J*M0/2+...
1j*alphaBA*omega(m)/2)*(1-cos(2*theta)) omega(m)+D+...
1j*alphaBB*omega(m)-(1/2)*wh*(sin(theta))^2 ...
(gamma*J*M0/2+1j*alphaBA*omega(m)/2)*(1+cos(2*theta))...
-(1/2)*wh*(sin(theta))^2;-(1/2)*wh*(sin(theta))^2 ...
(gamma*J*M0/2+1j*alphaAB*omega(m)/2)*...

```

```

(1+cos(2*theta)) * omega(m) + C + 1j * alphaAA * omega(m) - ...
(1/2) * wh * (sin(theta))^2 * (gamma * J * M0 / 2 + 1j * alphaAB * omega(m) / 2) * ...
(1 - cos(2*theta)); (gamma * J * M0 / 2 + 1j * alphaAB * ...
omega(m) / 2) * (1 + cos(2*theta)) - (1/2) * wh * (sin(theta))^2 ...
(gamma * J * M0 / 2 + 1j * alphaAB * omega(m) / 2) * (1 - cos(2*theta)) ...
- omega(m) + D + 1j * alphaBB * omega(m) - (1/2) * wh * (sin(theta))^2];
M = inv(H);
mA_plus(m) = prod(1) * M(1,1) + prod(2) * M(1,2) + prod(3) * M(1,3) + ...
prod(4) * M(1,4);
mB_plus(m) = prod(1) * M(2,1) + prod(2) * M(2,2) + prod(3) * M(2,3) + ...
prod(4) * M(2,4);
mA_minus(m) = prod(1) * M(3,1) + prod(2) * M(3,2) + prod(3) * M(3,3) + ...
prod(4) * M(3,4);
mB_minus(m) = prod(1) * M(4,1) + prod(2) * M(4,2) + prod(3) * M(4,3) + ..
prod(4) * M(4,4);
Iy(m) = (omega(m) * sin(theta) / (16 * pi)) * (gAA * ((abs(mA_plus(m)))^2 ...
- (abs(mA_minus(m)))^2) + gBB * ((abs(mB_plus(m)))^2 ...
- (abs(mB_minus(m)))^2) + 2 * gAB * real(conj(mA_plus(m)) * ...
mB_plus(m) - conj(mA_minus(m)) * mB_minus(m)));
end

```

```

%Plotting the dc spin current against the frequency
plot(omega, Iy);
xlabel('\omega [Hz]');
ylabel('$j^{\{0,dc\}}_{\{s_{y}\}} / \hbar \ : \ : [m^{\{-2\}}]$', 'interpreter', ...
'latex');
set(gcf, '-property', 'FontSize', 'FontSize', 25)
set(gcf, 'color', 'w');
set(gca, 'FontSize', 18);
hold on;

```

z-component

```

%Defining constants
alphaAA = 0.01; %Intra-sublattice damping parameter on...
sublattice A

```

```

alphaBB=0.01;%Intra-sublattice damping parameter on...
sublattice B
alphaAB=0.001;%Cross-sublattice damping parameter on...
sublattice A
alphaBA=alphaAB;%Cross-sublattice damping parameter on...
sublattice B

gAA=2*10^(19);%Intra-sublattice spin mixing conductance...
(sublattice A)
gBB=2*10^(19);%Intra-sublattice spin mixing conductance...
(sublattice B)
gAB=2*10^(18);%Cross-sublattice spin mixing conductance...
(sublattice A and sublattice B)

mu0=12.57*10^(-7);%Magnetic permeability
H0=0.7/mu0;%Field strength of the static part of...
the applied magnetic field
h_plus=0.005/mu0;%Field strength of the oscillating part of...
the applied field (right hand circularly polarized rotation)
h_minus=0.005/mu0;%Field strength of the oscillating part of...
the applied field (left hand circularly polarized rotation)

Kz=10^(-7);%Easy axis anisotropy constant
M0=10^5; %Saturation magnetization
gamma=10^11; %gyromagnetic ratio
wh=2*gamma*Kz*M0;
J=10^-4;%Exchange integral

theta=acos(mu0*H0/(2*J*M0)); %Angle subtended by the...
sublattice magnetization with respect to the easy axis
Theta=[1+cos(theta) 1-cos(theta);1-cos(theta) 1+cos(theta);...
1-cos(theta) 1+cos(theta);1+cos(theta) 1-cos(theta)];
h_circ=[gamma*mu0*h_plus/2; gamma*mu0*h_minus/2];

```

```

C=gamma*(2*Kz*M0*cos(2*theta)+mu0*H0*cos(theta)-J*M0*...
cos(2*theta));
D=gamma*(2*Kz*M0*cos(2*theta)-J*M0*cos(2*theta)+...
mu0*H0*cos(theta));

```

```

%Defining matrices and vectors

```

```

omega=linspace(1e9,6e11,2001); %Frequency of the...
oscillating applied field
mA_plus=zeros(1,2001);%Unit vector magnetzation on...
sublattice A (plus mode)
mB_plus=zeros(1,2001);%Unit vector magnetzation on...
sublattice B (plus mode)
mA_minus=zeros(1,2001);%Unit vector magnetzation on...
sublattice A (minus mode)
mB_minus=zeros(1,2001);%Unit vector magnetzation on...
sublattice B (minus mode)
Iy=zeros(1,2001);%dc spin pumping current...
polarized in the y-direction
prod=Theta*h_circ;

```

```

%Calculating the magnetization amplitudes and the ...
dc spin current

```

```

for m=1:2001

```

```

    H=[-omega(m)+C+1j*alphaAA*omega(m)-(1/2)*wh*...
        (sin(theta))^2 (gamma*J*M0/2+1j*alphaAB*omega(m)/2)*...
        (1-cos(2*theta)) -(1/2)*wh*(sin(theta))^2 (gamma*J*M0/2+...
        1j*alphaAB*omega(m)/2)*(1+cos(2*theta)); (gamma*J*M0/2+...
        1j*alphaBA*omega(m)/2)*(1-cos(2*theta)) omega(m)+D+...
        1j*alphaBB*omega(m)-(1/2)*wh*(sin(theta))^2 ...
        (gamma*J*M0/2+1j*alphaBA*omega(m)/2)*(1+cos(2*theta))...
        -(1/2)*wh*(sin(theta))^2;-(1/2)*wh*(sin(theta))^2 ...
        (gamma*J*M0/2+1j*alphaAB*omega(m)/2)*...
        (1+cos(2*theta)) omega(m)+C+1j*alphaAA*omega(m)-...
        (1/2)*wh*(sin(theta))^2 (gamma*J*M0/2+1j*alphaAB*omega(m)/2)*...

```

```

(1-cos(2*theta)); (gamma*J*M0/2+1j*alphaAB*...
omega(m)/2)*(1+cos(2*theta)) -(1/2)*wh*(sin(theta))^2 ...
(gamma*J*M0/2+1j*alphaAB*omega(m)/2)*(1-cos(2*theta)) ...
-omega(m)+D+1j*alphaBB*omega(m)-(1/2)*wh*(sin(theta))^2];
M=inv(H);
mA_plus(m)=prod(1)*M(1,1)+prod(2)*M(1,2)+prod(3)*M(1,3)+...
prod(4)*M(1,4);
mB_plus(m)=prod(1)*M(2,1)+prod(2)*M(2,2)+prod(3)*M(2,3)+...
prod(4)*M(2,4);
mA_minus(m)=prod(1)*M(3,1)+prod(2)*M(3,2)+prod(3)*M(3,3)+...
prod(4)*M(3,4);
mB_minus(m)=prod(1)*M(4,1)+prod(2)*M(4,2)+prod(3)*M(4,3)+...
prod(4)*M(4,4);
Iz(m)=(omega(m)*cos(theta)/(16*pi))*...
(gAA*(abs(mA_plus(m))^2-(abs(mA_minus(m))^2)-gBB*...
((abs(mB_plus(m))^2-(abs(mB_minus(m))^2)+2*gAB*...
real(conj(mA_minus(m))*mB_plus(m))...
-conj(mA_plus(m))*mB_minus(m)));
end

%Plotting the dc spin current against the frequency
plot(omega,Iz);
xlabel('\omega [Hz]');
ylabel('$j^{0,dc}_{s_z}/\hbar \::\:: [m^{-2}]$', 'interpreter', ...
'latex');
set(findall(gcf,'-property','FontSize'),'FontSize',25)
set(gcf,'color','w');
set(gca,'FontSize',18);
hold on;

```